

Numerical simulation and control of a continuous flow glass melting process using microwave radiation

Gonçalo Resende Moreira Feio

Thesis to obtain the Master of Science Degree in

Mechanical Engineering

Supervisor: Dr. Duarte Manuel Salvador Freire Silva de Albuquerque

Examination Committee

Chairperson: Prof. Carlos Frederico Neves Bettencourt da Silva

Supervisor: Dr. Duarte Manuel Salvador Freire Silva de Albuquerque

Member of the Committee: Prof. Luís Rego da Cunha de Eça

November 2020

To my mother in law, Hortensia, who prayed so much
for me and from Heaven made this work possible.

Acknowledgments

Firstly, I want to thank God – blessed be His Name – for loving me unconditionally and for giving me the necessary strength to finish this Thesis. Secondly, I want to thank my beloved wife, Esperanza, for her support, patience, sacrifice and for accepting staying alone countless nights while I was working in this Thesis. I want to thank my children, Madalena, Manuel, Esperanza and Marta for being so good, letting me work and even sleep during the few hours that I had left every day. I want to thank my mother, Ana, my father, Filipe, my sister, Mafalda, and my brother, Francisco, for all their help and encouragement. I want to thank my grandmothers, Maria Amélia and Maria Luísa, for their kindness. I want to thank my grandfathers, Manuel and Luís Filipe, who did not make it to see this work finished, for their bravery and advice. I want to thank all my uncles, aunts and cousins for their precious help. I also want to thank my Father in law, Miguel Angel, all my brothers and sisters in law and all my thirty-three nephews for their precious prayers.

I want to thank my Neocatechumenal community for their support and prayers and for continuously helping me knowing myself. I want to thank all my friends who never gave up on me.

I also want to thank Centimfe, specially the engineering department supervisor Nuno Fidelis, for all the support and encouragement and my colleagues João Caseiro and João Magrinho for reading and commenting this Thesis and for their useful suggestions to improve this work.

Finally, I want to thank my supervisor, Duarte Albuquerque, for the opportunity to develop this amazing work, for his constant support, guidance, patience and sacrifice shown in the hundreds of e-mails exchanged.

Resumo

A indústria da produção de vidro desempenha um papel importante no consumo global de energia com significativas emissões de CO_2 para a atmosfera devido aos combustíveis fósseis convencionais usados, como fonte de energia, no processo de fusão. Nas duas últimas décadas, tem sido desenvolvida investigação com o intuito de se estudar fontes alternativas de aquecimento para se reduzir as emissões de gases de efeito estufa. Entre essas alternativas, o aquecimento por micro-ondas aparece como uma promissora fonte de aquecimento no processo de produção de vidro, com vantagens substanciais relativamente às fontes de aquecimento convencionais.

Esta Tese tem como objetivo fornecer informações sobre os mecanismos de aquecimento por absorção de micro-ondas num processo contínuo de fusão de vidro. O software comercial *COMSOL Multiphysics* foi utilizado para os cálculos numéricos transientes que acoplam as físicas eletromagnética e térmica. Foi desenvolvido um algoritmo em linguagem *MATLAB* para controlar autonomamente o processo, por ajuste da potência fornecida, necessária para se obter as condições de saída desejadas, e da geometria da cavidade, com o objectivo de maximizar a eficiência eletromagnética. Foram realizados diversos estudos com o objetivo de analisar e quantificar a influência de vários parâmetros neste processo de produção.

O controlador desenvolvido provou ser um sucesso, fornecendo resultados em regime estacionário para diferentes condições operacionais, respeitando sempre as condições de saída desejadas e utilizando a menor quantidade de energia possível. Um estudo paramétrico inovador foi realizado, permitindo encontrar as condições operacionais que maximizam a eficiência global do processo. Para essas condições, verificaram-se gastos de energia 54% abaixo do consumo energético do processo convencional.

Palavras-chave: Modelação numérica de micro-ondas, Aquecimento por micro-ondas a temperaturas elevadas, Processo contínuo de fusão de vidro por micro-ondas, Otimização autónoma da eficiência eletromagnética e térmica, Design de equipamentos de micro-ondas.

Abstract

The industry of glass production plays an important role in the global energy consumption with significant CO_2 direct emissions to the atmosphere due to the conventional fossil fuels that are used as energy sources. In the past couple of decades considerable research has been made to switch the current energy sources in order to achieve reductions in the emissions of greenhouse gases. Among the alternatives, microwave radiation appears to be a promising one, with substantial advantages over the conventional heating sources.

This Thesis aims to give insight on the microwave absorption heating mechanisms that take place in the continuous flow glass melting process. The commercial software *COMSOL Multiphysics* was used to solve the three-dimensional transient simulations with the coupling of the electromagnetic and thermal physics. A *MATLAB* algorithm was developed to autonomously control the process by adjusting the power input, required to achieve a specific output condition, and the microwave cavity geometry, to maximize the microwave efficiency. Several studies were performed with the objective of showing how different parameters influence the continuous glass melting process heated by microwave energy.

The developed *MATLAB* controller has proven to be a success, providing steady-state solutions for different operational conditions while respecting the requested output ones and using the minimum possible power. An innovative parametric study was conducted, and it allowed to find the operational conditions that maximize the global efficiency of the process. For these conditions, energy savings of almost 54% relatively to the conventional process were achieved.

Keywords: Microwave numerical modeling, High temperature microwave heating, Continuous flow microwave process, Autonomous microwave and thermal efficiency optimization, Microwave cavity design.

Contents

Acknowledgments.....	v
Resumo	vii
Abstract.....	ix
List of Tables	xiii
List of Figures	xv
Nomenclature	xix
1 Introduction.....	1
1.1 Motivation	1
1.2 Objectives.....	2
1.3 Literature Review.....	3
1.3.1 Microwave heating applications in the glass industry	3
1.3.2 Factors that influence microwave heating.....	4
1.3.3 Continuous flow microwave heating.....	6
1.4 Thesis outline	9
2 Background.....	11
2.1 Maxwell's equations	11
2.2 Complex permittivity	12
2.3 Poynting Theorem and microwave dissipated power	14
2.4 Momentum and continuity equations.....	16
2.5 Heat equation	16
2.6 Microwave basics	17
2.6.1 Penetration depth.....	17
2.6.2 Microwave cavities.....	18
2.6.3 Rectangular waveguide	19
2.7 Numerical simulations with <i>COMSOL Multiphysics</i>	19
3 Numerical model.....	21
3.1 Geometry and simulation domains	21
3.2 Material properties.....	23
3.3 Boundary and initial conditions.....	27

3.3.1	Electromagnetic interface	28
3.3.2	Thermal interface	28
3.3.3	Flow interface.....	33
3.4	Phase change numerical modelling.....	33
3.5	Mass and energy balances.....	35
3.6	<i>Matlab</i> microwave heating controller code	36
4	Results and discussion.....	41
4.1	Mesh convergence analysis	41
4.2	Scalability study	44
4.3	Influence of the tube's rotation on the glass heating process.....	46
4.4	Thermal history and converged solution.....	50
4.5	Influence of plunger position updates, microwave leakage and <i>slip</i> boundary condition	57
4.5.1	Plunger position updates	58
4.5.2	Microwave leakage	60
4.5.3	<i>Slip</i> boundary condition.....	62
4.6	Tube inner diameter and mean flow velocity parametric studies.....	64
4.6.1	Influence of the diameter for a fixed mean flow velocity	64
4.6.2	Influence of the mean flow velocity for a fixed diameter	69
4.6.3	Combined parametric study	73
5	Conclusions	78
5.1	Achievements	79
5.2	Future Work.....	79
6	Bibliography	80

List of Tables

3.1	Aluminum alloy AW 7022 physical properties.....	23
3.2	Boron nitride physical properties	24
3.3	Alkaline earth silicate wool thermal properties.....	25
3.4	Chemical composition of the soda-lime silica glass studied in this work	25
3.5	Glass emissivity, melting temperature, latent heat of fusion and dynamic viscosity	27
4.1	Number of elements, NoE, and normalized grid spacing, NGS, of the created grids for the mesh convergence analysis	42
4.2	Results of the mesh convergence analysis by using the converged control variables for five different meshes.	43
4.3	Simulation times and average outlet temperature relative errors obtained with mesh 3 and 4 for one transient iteration with a physical time of $\Delta t_s = 44$ s in a machine with an AMD Ryzen 7200X CPU 8 cores and a clock speed of 3.7 GHz. All 8 cores were used in parallel computing	44
4.4	Scalability study results obtained with an AMD Ryzen 7200X CPU with 8 cores and a clock speed of 3.7 GHz.....	45
4.5	Operational conditions used for showing the control of the glass heating process done by the <i>MATLAB</i> algorithm.....	50
4.6	Steady-state results for the glass melting process with $d_i = 30$ mm and $\dot{m} =$ 3.6 kg/h.....	57
4.7	Operation conditions of the numerical simulations	58
4.8	Comparison of the steady-state results with and without microwave radiation leakage.....	61
4.9	Comparison of the steady-state results obtained using <i>no-slip</i> and <i>slip</i> boundary conditions at the tube inner walls.....	62
4.10	Operational conditions for the simulations done in the diameter parametric study.....	64
4.11	Operational conditions for the simulations done in the mean flow velocity parametric study	69
4.12	Steady-state results for the glass melting process with $d_i = 15$ mm and $\dot{m} =$ 11.92 kg/h.....	76

List of Figures

1.1	Dependence of the microwave efficiency on the inlet velocity for different applicator tube diameters. At the critical diameter of 45.6 mm, a critical value for the inlet velocity is found	9
2.1	Frequency response of dielectric constant and loss factor for a hypothetical dielectric material showing various known phenomena.....	13
3.1	Microwave cavity geometry designed for the numerical study of the glass melting process	22
3.2	Presentation of the (a) electromagnetic domain, (b) thermal domain and (c) flow domain. The computational mesh with 74837 tetrahedral elements is shown in illustration (d)	22
3.3	Boron nitride thermal conductivity temperature dependence, $k(T)$ [W/(m · K)].	24
3.4	Boron nitride dielectric properties temperature dependence, $\epsilon'_r(T)$ and $\epsilon''_r(T)$	24
3.5	Soda-lime silica glass density temperature dependence, $\rho(T)$ [kg/m ³]	26
3.6	Soda-lime silica glass dielectric constant, $\epsilon'_r(T)$, and loss factor, $\epsilon''_r(T)$, temperature dependence.....	26
3.7	Soda-lime silica glass thermal conductivity temperature dependence, $k(T)$ [W/(m · K)].....	27
3.8	Soda-lime silica glass specific heat capacity temperature dependence, $C_p(T)$ [J/(kg · K)].	27
3.9	Electromagnetic interface domain. Location of the <i>port</i> and <i>scattering</i> boundaries	28
3.10	Air flows induced by (a) hot vertical plate, (b) hot horizontal plate located below the air and (c) hot horizontal plate located above the air	30
3.11	Applicator tube inlet boundary condition in the models with (a) fixed temperature and (b) heat flux. Converged thermal solution for the (c) fixed temperature, and (d) heat flux models	32
3.12	Phase transition converged solution with (a) $\Delta T = 50$ K and (b) $\Delta T = 20$ K.....	34
3.13	Plunger parametric study for the initial thermal conditions in a model with $d_i = 30$ mm. The curve shows the value of $1 - S_{11} ^2$ for different plunger positions.....	38
3.14	Flowchart describing the <i>MATLAB</i> controller code.....	40

4.1	Convergence of the control variables for the five meshes along with the respective fit and result for the exact solution estimation, in red.....	44
4.2	Steady-state thermal field [K], for different rotation velocities, ω_r [rad/s]: (a) no rotation, (b) $\omega_r = 2\omega_{ref}$, (c) $\omega_r = 4\omega_{ref}$, (d) $\omega_r = 8\omega_{ref}$, (e) $\omega_r = 16\omega_{ref}$, (f) $\omega_r = 32\omega_{ref}$ and (g) $\omega_r = 64\omega_{ref}$	47
4.3	Glass and tube maximum temperatures at steady-state for different rotation velocities.....	47
4.4	Fraction of non-reflected microwave power, $1 - S_{11} ^2$, and microwave efficiency, η_{MW} , dependence on the rotation velocity	47
4.5	Penetration depth, δ [m], at the surface where the microwaves penetrate the glass for the cases (a) without rotation and b) with rotation velocity of $\omega_r = 32\omega_{ref}$ rad/s	48
4.6	Electric field norm [V/m] inside the glass for the cases (a) without rotation and (b) with rotation velocity of $\omega_r = 32\omega_{ref}$ rad/s, at a cross-section taken at the middle position inside the microwave cavity.....	49
4.7	Heat source [W/m ³] inside the glass for the cases (a) without rotation and (b) with rotation velocity of $\omega_r = 32\omega_{ref}$ rad/s, at a cross-section taken at the middle position inside the microwave cavity.....	49
4.8	Fraction of non-reflected microwave power, microwave efficiency and plunger position evolution during the physical time	51
4.9	Electric field norm [V/m] in the microwave cavity at the steady-state.....	51
4.10	Heat source [W/m ³] distribution, (a), in the glass thin layer facing the incoming microwave radiation. Distributions of the (b) electric field norm [V/m], (c) loss factor and (d) heat source [W/m ³] in the glass region at the steady-state	52
4.11	Average outlet glass temperature, maximum glass temperature, maximum tube temperature and outlet fraction of melted material evolutions during the physical time.....	53
4.12	Power input, microwave efficiency, transient term of the heat equation and plunger position evolutions during the physical time	54
4.13	Power input, power absorbed, power leakage, power reflected and microwave efficiency evolutions during the physical time	55
4.14	Power absorbed, transient term of the heat equation, sensible and latent heat at the outlet and thermal losses evolution during the physical time.....	55
4.15	Complete energy balance of the microwave cavity for the case with $d_i = 30$ mm and $\dot{m} = 3.6$ kg/h	56
4.16	Fraction of non-reflected microwave power evolution during the physical time, for $d_i = 30$ mm, with and without plunger position adjustments.....	58
4.17	Fraction of non-reflected microwave power evolution during the physical time, for $d_i = 15$ mm, with and without plunger position adjustments.....	59
4.18	Electric field norm [V/m] in the microwave cavity at steady-state, for the case with (a) $d_i = 30$ mm and (b) $d_i = 15$ mm.....	60

4.19	Electric field norm [V/m] in the microwave cavity at steady-state for the case (a) with and (b) without microwave radiation leakage	61
4.20	Distributions of the electric field norm [V/m], temperature [K], heat source [W/m ³] and fraction of melted phase in the glass region at steady-state, for the case with (a) <i>no-slip</i> and (b) <i>slip</i> boundary conditions at the tube inner walls	63
4.21	Fraction of non-reflected microwave power, $1 - S_{11} ^2$, microwave efficiency, η_{MW} , thermal efficiency, η_T , outlet fraction of melted material, θ , and global efficiency, η_G , versus tube inner diameter, d_i , for a constant mean flow velocity of $U_{ave} = 0.64$ mm/s.....	65
4.22	Penetration depth values for the converged solutions with (a) $d_i = 12$ mm, (b) $d_i = 15$ mm, (c) $d_i = 20$ mm, (d) $d_i = 30$ mm and (e) $d_i = 40$ mm. For all cases, the penetration depth is always below 1 mm in the glass outer surface inside the microwave cavity.	66
4.23	Heat source distribution [W/m ³] in the external surface of the absorbing layer for (a) $d_i = 12$ mm, (b) $d_i = 15$ mm, (c) $d_i = 20$ mm, (d) $d_i = 30$ mm and (e) $d_i = 40$ mm	66
4.24	Heat source distribution [W/m ³] in the absorbing layer for (a) $d_i = 12$ mm, (b) $d_i = 15$ mm, (c) $d_i = 20$ mm, (d) $d_i = 30$ mm and (e) $d_i = 40$ mm	67
4.25	Global efficiency, η_G , versus tube inner diameter, d_i , for a constant mean flow velocity of $U_{ave} = 0.64$ mm/s, with and without tube rotation.....	68
4.26	Specific energy consumption, SEC [kJ/kg], versus tube inner diameter, d_i , for a constant mean flow velocity of $U_{ave} = 0.64$ mm/s	69
4.27	Fraction of non-reflected microwave power, $1 - S_{11} ^2$, microwave efficiency, η_{MW} , thermal efficiency, η_T , outlet fraction of melted material, θ , and global efficiency, η_G , versus mean flow velocity, U_{ave} , for a tube inner diameter of $d_i = 30$ mm	70
4.28	Thermal field [K] and heat source distribution [W/m ³] in the glass domain for (a) $U_{ave} = 0.64$ mm/s, (b) $U_{ave} = 1.93$ mm/s and (c) $U_{ave} = 6.10$ mm/s, for a tube inner diameter of $d_i = 30$ mm	71
4.29	Penetration depth values for (a) $U_{ave} = 0.64$ mm/s, (b) $U_{ave} = 1.93$ mm/s and (c) $U_{ave} = 6.10$ mm/s, for a tube inner diameter of $d_i = 30$ mm.....	71
4.30	Global efficiency, η_G , versus mean flow velocity, U_{ave} , for a tube inner diameter of $d_i = 30$ mm, for the cases with and without tube rotation.....	72
4.31	Domain for the combined parametric study. Each point represents a performed simulation	73
4.32	Combined influence of the tube inner diameter, d_i [mm], and mean flow velocity, U_{ave} [mm/s], on the (a) microwave efficiency, η_{MW} , (b) outlet fraction of melted material, θ , (c) global efficiency, η_G , and (d) thermal efficiency, η_T	74
4.33	Thermal field [K] and heat source distribution [W/m ³] in the glass domain for (a) $U_{ave} = 0.64$ mm/s, (b) $U_{ave} = 4.30$ mm/s, (c) $U_{ave} = 8.50$ mm/s, which is the critical mean flow velocity and (d) $U_{ave} = 11.50$ mm/s, for a tube inner diameter of $d_i = 15$ mm.....	75

4.34	Complete energy balance of the microwave cavity for the case with $d_i = 15$ mm and $\dot{m} = 11.92$ kg/h.....	77
------	---	----

Nomenclature

Acronyms

ARC	Asymptotic range checking
CMC	Carboxymethyl cellulose
FDTD	Finite difference time domain
GCI	Grid convergence index
KPI	Key performance indicator
LH	Latent heat
NGS	Normalized grid spacing
NoE	Number of elements
SEC	Specific energy consumption
SH	Sensible heat
TE	Transverse electric
TM	Transverse magnetic

Constants

c	Speed of light in vacuum, 3×10^8 m/s
g	Gravitational acceleration, 9.81 m/s ²
ϵ_0	Permittivity in vacuum, 8.85×10^{-12} F/m
μ_0	Permeability in vacuum, $4\pi \times 10^{-7}$ H/m
σ_b	Stefan-Boltzmann constant 5.67×10^{-8} W/(m ² · K ⁴)

Math operators

$\frac{\partial}{\partial t}$	Derivative with respect to time
$\frac{\partial}{\partial x}$	Derivative with respect to an arbitrarily variable x
Δ	Difference operator
$\nabla \cdot$	Divergence operator

$\nabla \times$	Rotational operator
∇	Gradient operator
∇^2	Laplace operator
\times	Cross product operator
\cdot	Dot product operator
j	Imaginary number
$Re[]$	Real part of a complex variable
$\langle \rangle_t$	Time average of a variable

Greek symbols

α	Thermal diffusivity [m^2/s]
β	Volumetric thermal expansion coefficient [K^{-1}]
δ	Penetration depth [m]
δ_{BL}	Boundary layer thickness [m]
ε	Surface emissivity
ε_i	Emissivity of surface i
ϵ	Permittivity [F/m]
ϵ_r	Relative permittivity
ϵ'_r	Relative dielectric constant
ϵ''_r	Relative loss factor
η_{MW}	Microwave efficiency
η_T	Thermal efficiency
η_G	Global efficiency
θ	Fraction of liquid phase
k	Thermal conductivity [$\text{W}/(\text{m} \cdot \text{K})$]
k_0	Wave number in vacuum [m^{-1}]
λ	Wavelength [m]
λ_c	Cut-off wavelength [m]
μ	Permeability [H/m]
μ_r	Relative permeability
μ_v	Dynamic viscosity [$\text{Pa} \cdot \text{s}$]
ν	Kinematic viscosity [m^2/s]
π	Pi
ρ	Density [kg/m^3]
ρ_q	Charge density [C/m^3]
ρ_s	Surface charge density [C/m^2]
σ	Electrical conductivity [S/m]
ω	Angular frequency [rad/s]

ω_r	Applicator tube rotation velocity [rad/s]
ω_{ref}	Tube reference rotation velocity [rad/s]

Roman symbols

A	Area [m ²]
A_i	Area of surface i [m ²]
A_s	Surface area [m ²]
\vec{B}	Magnetic flux density [Wb/m ²]
C_p	Specific heat capacity [J/(kg · K)]
$C_{p_{app}}$	Apparent specific heat capacity [J/(kg · K)]
\vec{D}	Electric displacement or electric flux density [C/m ²]
d_{ext}	External diameter of the insulation around the tube [m]
d_i	Applicator tube inner diameter [m]
d_{out}	Applicator tube outlet inner diameter [m]
\vec{E}	Electric field [V/m]
$E(n_p)$	Parallel computing efficiency
e	Nepper number
F_{ij}	View factor
F_s	Safety factor
f	Frequency [Hz]
\bar{f}	Richardson extrapolation
f_c	Cut-off frequency [Hz]
Gr_L	Grashof number
\vec{H}	Magnetic field [A/m]
H_i	Irradiation of surface i
h	Convection coefficient [W/(m ² · K)]
\vec{j}	Electric current density [A/m ²]
J_i	Radiosity of surface i
J_s	Surface current density [A/m ²]
L	Characteristic length [m]
L_f	Latent heat of fusion [J/kg]
\dot{m}	Mass flow rate [kg/s]
$\overline{Nu_L}$	Average Nusselt number
\vec{n}	Normal vector
n_p	Number of processors
P	Pressure [Pa]

\vec{P}	Polarization [C/m ²]
P_{abs}	Power absorbed [W]
P_h	Heating useful power [W]
P_{in}	Power input [W]
P_L	Leakage power [W]
P_{loss}	Thermal losses [W]
Pr	Prandtl number
P_{ref}	Power reflected [W]
P_s	Surface perimeter [m]
p	Order of accuracy
Q	Heat generation by microwave absorption [W/m ³]
Q_i	Radiation power leaving surface i
Ra_L	Rayleigh number
r	Refinement ratio
r_i	Applicator tube inner radius [m]
r_{out}	Applicator tube outlet inner radius [m]
S	Arbitrarily Surface
$S(n_p)$	Parallel computing speed up
\vec{S}	Poynting vector [W/m ²]
S_{11}	Reflection coefficient
T	Temperature [K]
T_{amb}	Ambient temperature [K]
T_i	Temperature of surface i [K]
T_m	Melting temperature [K]
T_{max}	Maximum temperature [K]
T_{out}	Average outlet temperature [K]
T_s	Surface temperature [K]
t	Time [s]
$t(n)$	Computational time using n processors
\vec{U}	Velocity field [m/s]
U_{ave}	Mean flow velocity [m/s]
V	Volume [m ³]
\vec{X}	Arbitrarily complex vector field
\vec{X}^*	Conjugate of an arbitrarily complex vector field
\vec{X}_s	Phasor of an arbitrarily complex vector field

Chapter 1

Introduction

This chapter aims to introduce the present work. The motivation for this Thesis is presented in Section 1.1, followed by the main objectives that it pursues in Section 1.2. The literature review that was done during this work is exposed in Section 1.3 and, finally, in Section 1.4 the Thesis outline is drawn.

1.1 Motivation

The glass production industry plays an important role in the Europe's energy consumption, as well as in its CO_2 emissions, due to the high temperatures needed in the process of glass melting [1]. In order to reduce costs and emissions of greenhouse gases, major efforts have been made to improve the efficiency of the process of glass melting. Several studies report improvements in furnace designs as can be seen, for example, in [2]. On the other hand, Yao *et al.* [3] report the usage of different energy sources, namely a radio-frequency plasma, a 12-phase alternating current arc and an oxygen burner in order to achieve better energy efficiencies than those of the conventional air-fuel firing method. Although the research mentioned above is far from being complete, new energy sources are being extensively studied in order to reduce emissions and costs. In the last couple of decades, microwave energy started being used in glass processing with promising results namely in the quality of the final product and in time and energy savings [4-5].

Microwave heating is a very complex phenomenon which involves the two-way coupling of the Maxwell's and heat transfer equations due to the materials dielectric properties dependence on temperature [6]. A detailed description of microwave heating can be found in [7] and [8]. Microwave heating is an energy conversion phenomenon rather than an energy transfer one. Essentially, when a time-varying electric field reaches a dielectric medium, it suffers some attenuation and lagging mainly due to the polarization of dipolar molecules. This alternating reorientation of the molecules generates heat, result of friction mechanisms. There may be other heating mechanisms such as ionic conduction and the Maxwell-Wagner effect, but the dipole polarization is the most influent on microwave frequencies [9-10]. The material response to the external electric field is measured by its complex permittivity, ϵ . There are several factors that influence microwave heating such as the physical properties of the mate-

rial being heated, its geometry and location within the electric field, the frequency and operating mode of the external electric field, the geometry of the microwave cavity, etc. [9].

One of the most relevant parameters of microwave heating is the penetration depth, δ [m], which is the depth within the material where the external electric field amplitude falls to $1/e$ of its value at the material surface. The penetration depth decreases with the increase of the frequency of the electric field and with the increase of the loss factor, which is the imaginary part of the relative complex permittivity [11]. The microwave dissipation power density, which is the power per unit volume that is absorbed by the material, is proportional to the loss factor, to the working frequency and to the square of the electric field intensity. Almost all the power absorption occurs within a layer of thickness equal to δ , starting from the material external surface. Since microwave heating is a volumetric phenomenon, values of the penetration depth that are considerably smaller than the thickness of the material being heated will mean a less efficient heating process.

The main advantages of high temperature microwave heating, over the conventional one, are reported in several studies. Since the heat generation due to microwave absorption is a volumetric phenomenon, microwave heating allows a significant decrease in the process cycle time with less energy consumption [4-5]. Concerning the environmental impact, microwave heating is preferable to the conventional heating method since it has no direct CO_2 emissions [12]. On the other hand, there are several physical mechanisms in microwave heating that can turn out to be disadvantageous. Firstly, since the electromagnetic field is strongly coupled with the thermal field it is necessary to establish a method to control the process in order to have efficiencies as high as possible, by keeping the electric field peaks over the material to be heated. This can be done by changing the cavity geometry or the material position within the cavity, otherwise the microwave power density can decrease considerably leading to low heating rates and heating efficiencies. Secondly, some materials like glass and other ceramics, have a loss factor that increases sharply with the temperature. Since the power absorbed by the material is proportional to the loss factor, a feedback mechanism usually called *thermal runaway* can occur leading to hotspots whose temperature grows uncontrollably [13-15]. These hotspots can damage the heating system and can create undesirably temperature gradients in the material leading to thermal stresses that can compromise the final product. In order to prevent this phenomenon, the power input of the system must be controlled.

1.2 Objectives

The main objective of this Thesis is to develop a numerical model to study the continuous flow glass melting process, while using microwave radiation as the heating source, in a single-mode cavity. *COMSOL Multiphysics* is the selected commercial software since it has been widely used in several studies involving the coupling of electromagnetic and heat transfer physics [15-19]. Besides there are also reports concerning verification and validation of numerical models created in *COMSOL Multiphysics* [16-17, 20]. In order to obtain steady state solutions with maximum efficiency, minimized power input

and with all the material being processed at the outlet, a *MATLAB* algorithm will be developed following the previous works of Mimoso *et al.* [19] and Mendes [21].

It is the purpose of this work to analyze the evolution of the heating and melting process of the glass as it flows through an applicator tube, which is partially inside a microwave cavity. Different parametric studies will be carried out to study the influence of the applicator tube inner diameter and mean flow velocity in the global efficiency of the process. The influence of the tube rotation in the efficiency and thermal field will also be analyzed. This work will look for insight on the control of the continuous flow melting process of glass, on the principal difficulties inherent to the process, on the optimal operational conditions and on improvements relatively to previous works on the literature.

1.3 Literature Review

This section aims to give an insight into the research that has already been done on microwave heating applications. In the first subsection, attention will be given to microwave heating applications in the glass industry. The second subsection will focus in the factors that influence microwave heating. Finally, the third subsection will deal with continuous flow microwave heating applications presenting some important parametric studies.

1.3.1 Microwave heating applications in the glass industry

Besides food industry where microwave heating has proven to be extremely effective, there are several other applications, namely in the glass and ceramic industry, where this heating source is emerging with promising results. Mandal and Sen [10] reported the usage of microwave radiation for drying, joining, sintering and coating of ceramic materials. This study also mentions small scale batch glass melting and a comparison between the microwave heating process and an equivalent conventional process in terms of final product properties and energy efficiency. It states that it was verified an enhancement in the optical absorption for iron-doped phosphate glasses when processed by microwave radiation. Energy savings of 65% and considerable reductions in melting time were reported in small batch glass melting comparing to the conventional heating process. In another study, Mandal *et al.* [5] reported a comparative analysis between conventional and microwave assisted small batch glass melting. Examination by X-ray diffraction analysis of both final products showed that both materials have almost identical properties. Again, energy savings and time reductions of about 60% were reported, leading to a considerable decrease in the overall process cost.

Bykov *et al.* [8] presented a topical review on high-temperature microwave processing of materials and, particularly, a review on the advantages of microwave heating in ceramic sintering. Besides the clear energy consumption and cycle time reductions, it is reported that higher material densities have been reached with microwave heating comparatively to conventional sintering process. A reduction in the sintering temperature is also observed thus leading to cost savings. The volumetric phenomenon

in microwave heating allows higher heating rates and therefore a reduction in grain size which improves the overall performance. The work of Agrawal [4] also reports several advantages of microwave heating over conventional heating in the sintering process of ceramics and metals. Again, energy savings and cycle time reductions due to better material diffusion and phase transformations are reported. Finer grain sizes after microwave assisted sintering are achieved leading to better mechanical and physical properties of the sintered materials. A reference to microwave glass melting is made at the end of the work but, again, only in a small batch process.

Acevedo *et al.* [22] presented a numerical study of microwave heating of cullet glass by means of a combined electric and thermal model. Although it is a batch process, this work presents a very important issue in microwave heating of ceramic materials which is the initial part of the heating process. Since ceramic materials, such as glass, poorly absorb microwave radiation at temperatures below 300 °C due to the very low values of its loss factor at these temperatures, a preheating mechanism is necessary to activate the glass absorption of microwaves. This study reports the use of a silicon carbide, SiC, susceptor which is a high absorber of microwave radiation at low temperatures, to initiate the glass heating process. The numerical results showed that the susceptor can provide appropriate preheating for the glass at low temperatures and that the susceptor location significantly influences the heating process. The authors mention the importance of performing a previous analysis of the susceptor location to find the optimal one in order to get the most uniform temperature fields and the highest possible efficiencies.

1.3.2 Factors that influence microwave heating

As mentioned earlier, microwave heating is a very complex phenomenon and there are many factors that play an important role in the process. It is important to know these factors in order to have good efficiencies which may lead to the advantages stated above such as energy consumption and cycle time reductions in the heating process. Loharkar *et al.* [9] highlighted four significant parameters affecting microwave heating. The first one is the material dielectric properties, namely the complex permittivity and the ratio between its imaginary and its real terms, which indicates if the material is suitable to be heated by microwave radiation. The heating mechanism in electric field heating is another parameter that influences microwave heating. The authors refer three of them, namely polarization of dipolar molecules, ionic conduction and Maxwell-Wagner effect. The third parameter is related to the load itself, which is the material that is being heated. Here, the penetration depth is of extreme importance because it controls how uniformly distributed is the microwave dissipation power density, *i.e.*, how uniform will be the heating inside the material volume. In order to achieve good efficiencies, the size of the load should be close to the order of magnitude of the penetration depth. Because microwaves form a standing wave pattern inside the cavity due to interference phenomena, good heating efficiencies are achieved when the load is positioned in a spot with high electric field amplitude. Finally, the kind of applicator or microwave cavity is the last influencing parameter reported in this work. The heating pro-

cess is strongly influenced by the microwave cavity geometry and whether it is in a single-mode or multi-mode configuration.

Clemens and Saltiel [23] presented a detailed numerical model to solve the coupled electromagnetic-thermal problem using the finite difference time domain method (FDTD). The purpose of the study was to understand the influence of the working frequency, load size and dielectric properties of the heated material. The simulations were performed using a multi-mode cavity. It was reported that small variations in the working frequency have a tremendous impact in the heating process because of the resonance effect. This indicates that when using multi-mode cavities, its geometry must have a resonant frequency that needs to be the same as the working frequency. Regarding the dielectric properties, it was shown that they can influence the resonant behavior of the system and thus the efficiency of the process. Simulations with different load sizes indicated that there is a critical size which is related to the cut-off frequency phenomenon, *i.e.*, when the distance between the load and the cavity walls is less than half of a wavelength. The waves are strongly attenuated as they try to pass around the load and, consequently, the effective surface area for wave penetration is reduced leading to a power absorption decrease. Taking that phenomenon into account, the study reports that above the critical size, the microwave efficiency, *i.e.*, the ratio between the power absorbed and the power input, decreases. Below the critical size, the microwave efficiency rises until critical conditions are achieved. If resonance occurs, *i.e.*, phase matching of reflections off the load and walls which create a symmetric pattern, microwave efficiency can have a maximum value below the critical conditions.

In the study of Cha-um *et al.* [24], a numerical analysis of microwave heating of a water and oil layer inside a single-mode cavity was performed. Experimental data was then used to validate the numerical results. The authors report the effect of microwave power in the heating process, stating that higher power provides a greater heat generation inside the material. The influence of the load size was also studied. The results showed that, when the thickness of the material being heated is close to the value of the penetration depth, the heat rate is improved. The position of the load inside the cavity proved to be an influent parameter in the heating process.

Gao *et al.* [25] studied the influence of various design parameters on the performance of microwave heating of a water film, namely the efficiency of the process and the heating uniformity. In this work the effects of port location, load position and cavity shape, among others, are discussed. It is reported that cubic cavities have better performance than cylindrical or spherical ones. Since the load is heated inside a multi-mode cavity without any kind of impedance match control, very low microwave efficiencies are reported.

The work of Morschhäuser *et al.* [26] depicted the influence of the microwave cavity geometry on the heating process. The study describes a microwave system that combines the advantages of both single-mode and multi-mode cavities allowing a high efficiency heating process with high mass flow rates.

In short, there are several parameters that influence the microwave heating of a load. Those parameters, well documented in the literature, are essentially the dielectric properties of the material, the heating mechanisms, the penetration depth, the load geometry and position, the microwave cavity geometry, the working frequency and the power input.

1.3.3 Continuous flow microwave heating

In this subsection continuous flow microwave heating is addressed. The first group of studies are related to the use of *COMSOL Multiphysics* for the numerical modeling of continuous flow microwave heating processes. This software has been extensively used in such numerical problems, achieving relative errors in an average of 5% between simulated and measured data. The second group presents some parametric studies in continuous flow microwave heating where several useful conclusions are drawn.

The work of Salvi *et al.* [16] consists in the development of a numerical model in *COMSOL Multiphysics* to simulate temperature profiles in Newtonian (tap water) and non-Newtonian (carboxymethyl cellulose, CMC, solution) fluids during continuous flow microwave heating. Iterative coupling of electromagnetism, heat transfer and fluid flow equations was granted by the software. The model consisted in a rectangular waveguide connected to an elliptical focusing microwave cavity where the vertical applicator tube was placed. Heat transfer between the fluids and the applicator tube was not considered and the tube was taken as transparent to microwave radiation. A microwave frequency of 915 MHz was used in the study. The results showed clearly that the power generation is influenced by the dielectric properties of the material being heated. Experimental measurements were taken to validate the simulation results. Differences between experimental and numerical results were found to be of around 6% for the electromagnetic power absorbed and values of $R^2 \approx 0.9$ were found for the linear correlation between simulated and measured temperatures.

Tuta and Palazoğlu [17] presented a *COMSOL Multiphysics* finite element model of continuous flow microwave heating of fluids. Distilled water and CMC solution at several flow rates were used as heated materials. A cavity with similar configuration as the one in the work mentioned above was used. A working frequency of 915 MHz was also used. The main difference consisted in the geometry of the applicator tube which was helical and not a vertical straight tube as in the previous study [16]. Convection heat transfer was considered between the tube and the surroundings and *scattering* boundary conditions were used in the inlet and outlet of the tube to account for microwave radiation leakage. An experimental setup was also developed to validate the numerical model, showing differences of around 8%. The results showed that distilled water presented better thermal uniformity at the outlet than CMC solutions. However, when compared to other results presented in the literature, the helical tube allowed for better uniformity in the heating of CMC solutions than other tube geometries. This phenomenon was due to secondary flows caused by the tube's curvature.

Wu *et al.* [18] presented a numerical model of a reaction tube with cross structures located in a single-mode cavity with the aim of achieving uniform microwave heating in ethyl acetate production. The use of *COMSOL Multiphysics* enabled the coupling of the Maxwell's, the heat transfer, the reaction kinetics and the Navier-Stokes equations. Different initial velocities were compared in order to obtain the flow rate that provides the best thermal uniformity and heating efficiency. The influence of the distance and angle between each cross structure on the heating process have also been studied. In this model, heat exchanges between the mixture and the reaction tube were not considered. The results showed that the smallest flow rate and the smallest distance between cross structures are the best

combination to achieve heating uniformity and higher efficiencies. The angle between cross structures was considered to have little influence in the heating process. An experimental setup was manufactured to validate the numerical results. Measurements of the temperature in two different locations out of the waveguide were taken and compared to the numerical results giving relative errors below 2% for all flow rates thus revealing good agreement between the numerical and experimental results.

The studies presented so far in this subsection have proved that *COMSOL Multiphysics* is a powerful tool to model continuous flow microwave heating processes. The following ones will show important parametric studies that have already been done which may give some insight about the microwave heating phenomena.

Mimoso *et al.* [19] developed a numerical model in *COMSOL Multiphysics* in order to simulate the continuous microwave glass melting process in a single-mode cavity operating at 2.45 GHz in a TE₁₀ mode with an alumina vertical container tube passing through it. A moving plunger was considered to allow the impedance matching during the simulations. The walls of the microwave cavity, including inlet and outlet of the tube, were considered as perfect electrical conductors, a classic boundary condition of the Maxwell's equations. Convection and radiation heat transfer were assumed at the external boundaries of the domain and surface-to-surface radiation inside of the cavity was considered. The flow of the material was assumed to be laminar with *slip* boundary condition imposed on the inner surface of the tube. The velocity field was calculated separately and then imported to the microwave heating model, since this field was not considered coupled with the other ones. Phase change was modeled by an apparent heat capacity used in the heat equation. Both thermal and dielectric properties of the glass were assumed to be temperature dependent. In order to obtain steady-state solutions for different operation conditions with high microwave efficiency and sufficiently high outlet temperatures, a *MATLAB* code was developed to allow for both power input and plunger position control during successive transient electromagnetic-thermal simulations. Two parametric studies were conducted in order to analyze the effect of the mass flow rate and temperature input.

The results obtained showed that the plunger adjustment has a significant impact on the steady-state microwave efficiency. Without this continuous impedance matching the model converged to a solution with a low microwave efficiency. Regarding the influence of the mass flow rate, the authors state that there is no evident trend for the variation of the microwave efficiency. However, since the thermal efficiency increased with the mass flow rate due to the reduction of the residence time, the global efficiency rose until a certain value. Concerning the temperature input, it was concluded that once the microwave oven reaches steady state with melting of glass there is no need to preheat the material with a different heating equipment.

The work of Zhu *et al.* [27] presents a detailed numerical model to study the heat transfer in continuous flow. The main objective of this study was to understand the effects of the load dielectric properties, of the applicator tube diameter and its location and of the microwave cavity geometry on the heating process. The FDTD method was used to solve the Maxwell's equations using a leapfrog scheme. To solve the energy and momentum equations a cell centered finite volume approach was used. The simulation domain consisted of a rectangular waveguide connected to an elliptical cross sectioned microwave cavity. The fluid flowed inside a vertical cylindrical tube passing through the cavity.

Three different fluids were used in this study: apple sauce, skim milk and tomato sauce, whose dielectric properties were assumed to be temperature dependent. The microwave worked at a frequency of 915 MHz in a TE_{10} mode. The applicator tube was assumed to be electromagnetically transparent and the walls of the waveguide and cavity were assumed to be perfect conductors. *No-slip* boundary condition was used in the inner wall of the applicator tube and the flow was assumed to be hydrodynamically fully developed. The power-law assumption was used to describe the behavior of the non-Newtonian fluids. At the outer wall of the applicator tube convection and radiation losses were used as thermal boundary conditions.

Concerning the effect of the dielectric properties, the results obtained confirmed that materials with higher loss tangent, which is the ratio between the imaginary and real terms of the complex permittivity, absorb more microwave power. Regarding the tube diameter, the results clearly showed that there is a critical value for the diameter for which the power absorption achieves a maximum value. This critical value is different for each fluid, being smaller for materials with higher loss tangent. This phenomenon is related to the cut-off frequency effect referred to by Clemens and Saltiel [23]. With respect to the position of the applicator tube, the results showed that the best microwave efficiency is achieved when the tube passes through the center of the elliptical cross section of the microwave cavity. A shift from that location causes a decrease in the power absorption due to the cut-off frequency phenomenon, as the distance between the tube and the walls of the cavity decreases. Changing the cavity cross section caused a decrease in the microwave efficiency. As the major axis of the ellipse became smaller, *i.e.*, as cross section tended to a circular shape the resonance of the cavity decreased causing a reduction in the power absorbed.

Yousefi *et al.* [28] developed a numerical model on *ANSYS Multiphysics* software to investigate the effects of inlet velocity, cavity height and applicator tube diameter on the process of microwave heating of continuous flowing water. Just like the previous work, the simulation domain used was a rectangular waveguide connected to an elliptical cross sectioned microwave cavity with a vertical applicator tube passing through its center. The dielectric properties of water were assumed to be temperature dependent. The water flow was assumed to be laminar, stationary and fully developed. *No-slip* boundary condition was applied to the inner wall of the applicator tube, which was assumed to be perfectly insulated. No phase change was considered during the simulation and the water thermal properties were assumed to be temperature dependent.

Regarding the effect of the inlet velocity, the results showed that the power absorbed increased with the inlet velocity. Since the power input was kept constant, it implies that an increase in the inlet velocity will cause an increase in the microwave efficiency. This was justified by the increase of the water dielectric properties with decreasing temperature. For constant power input, as the inlet velocity increases, the temperature decreases in the water volume causing an increase in the loss tangent and thus in the absorption ability of the material. As for the influence of the applicator tube diameter, the results showed that there is a critical diameter that is dependent on the dielectric properties, which decreases with the increase of the loss tangent. This agrees with the conclusions drawn by Clemens and Saltiel [23] and by Zhu *et al.* [27]. At the critical diameter, maximum microwave efficiency was observed for almost all inlet velocities. The results also showed that, at the critical diameter, there is a

critical value for the inlet velocity corresponding to the best combination to achieve the maximum microwave efficiency. For diameters below the critical value, the microwave efficiency increases with increasing inlet velocity as discussed above. However, the results showed that for diameters above the critical value, the microwave efficiency decreases with increasing inlet velocity. These conclusions are illustrated in Figure 1.1.

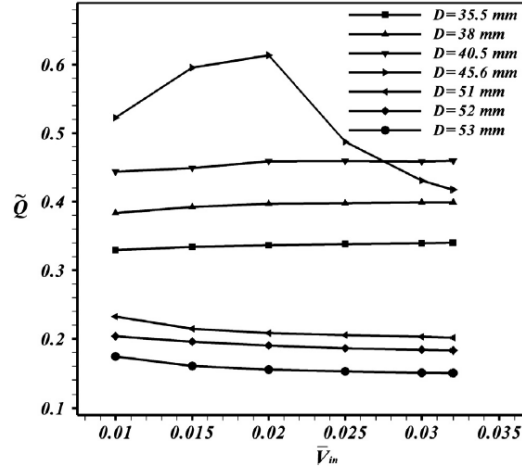


Figure 1.1: Dependence of the microwave efficiency on the inlet velocity for different applicator tube diameters. At the critical diameter of 45.6 mm, a critical value for the inlet velocity is found [28].

Concerning the height of the cavity, and thus the height of the applicator tube, the results demonstrated that its increase causes a negative effect in the microwave efficiency.

Patil *et al.* [29] presented an experimental work that aimed to study the effect of the load size on the efficiency of microwave heating of ethylene glycol in both stop flow and continuous flow conditions. The setup consisted in rectangular waveguide operating at 2.45 GHz with a vertical applicator tube passing through it. Concerning only the continuous flow results, it was shown that the microwave efficiency rose monotonously with the increase of the tube inner diameter, ranging from 4 – 11 mm. The authors mentioned that larger diameters were impossible to test due to microwave leakage.

1.4 Thesis outline

This Thesis is composed by five chapters. In Chapter 1, an introduction to the subject of this work and its main objectives are addressed. The state-of-the-art regarding microwave heating processes is also presented in this chapter through a literature review. Chapter 2 aims to give some insight on the physical background of the microwave heating process. The description of the developed numerical model that simulates the continuous flow glass melting process is presented in Chapter 3. In Chapter 4, the results obtained for several performed studies and respective discussions are shown. Finally, Chapter 5 presents the main conclusions of this Thesis as well as its main achievements. Guidelines for eventual future work in the microwave glass melting process are also presented in this final chapter.

Chapter 2

Background

This chapter aims to introduce the theoretical background for this work. In Section 2.1 the Maxwell's equations are presented. Section 2.2 aims to give an insight on the dielectric permittivity, explaining why it is a complex quantity for lossy materials. The energy balance of the electromagnetic radiation and the power dissipated in a lossy medium are addressed in Section 2.3. The continuity and momentum equations that governs the incompressible laminar flows are described in Section 2.4, while the heat equation is presented in 2.5. In Section 2.6 some microwave basic concepts are introduced. Finally, in Section 2.7 the coupling between the Maxwell's and heat equations done by the commercial software *COMSOL Multiphysics* is described.

2.1 Maxwell's equations

The Maxwell's equations are a set of four equations that constitute the basis for the electromagnetic theory, describing the interaction between the electric and magnetic fields. Faraday's law of induction, Maxwell-Ampere's law, electric and magnetic Gauss's laws are, respectively, found below:

$$\nabla \times \vec{E} = -\frac{\partial \vec{B}}{\partial t} \quad (2.1)$$

$$\nabla \times \vec{H} = \vec{J} + \frac{\partial \vec{D}}{\partial t} \quad (2.2)$$

$$\nabla \cdot \vec{D} = \rho_q \quad (2.3)$$

$$\nabla \cdot \vec{B} = 0 \quad (2.4)$$

where \vec{E} is the electric field [V/m], \vec{B} is the magnetic flux density [Wb/m²], \vec{H} is the magnetic field [A/m], \vec{J} is the electric current density [A/m²], \vec{D} is the electric displacement or electric flux density [C/m²], ρ_q is the charge density [C/m³] and t is time [s].

The following equations are the constitutive relations that describe the macroscopic properties of a linear isotropic medium, where the electric and magnetic fields exist, and show how those fields relate to each other:

$$\vec{D} = \epsilon \vec{E} \quad (2.5)$$

$$\vec{B} = \mu \vec{H} \quad (2.6)$$

$$\vec{J} = \sigma \vec{E} \quad (2.7)$$

where ϵ is the permittivity [F/m], μ is the permeability [H/m] and σ is the electrical conductivity [S/m] of the medium.

Assuming that the fields have an harmonic time dependence, phasor notation can be applied to represent any field as:

$$\vec{X} = \vec{X}_0 \cos(\omega t + \theta_X) = \text{Re}[\vec{X}_0 e^{j\theta_X} e^{j\omega t}] = \text{Re}[\vec{X}_s e^{j\omega t}] \quad (2.8)$$

where $\omega = 2\pi f$ is the angular frequency [rad/s], with f being the frequency [Hz] and $j = \sqrt{-1}$. Equations (2.1) and (2.2) can then be rewritten in phasor notation as:

$$\nabla \times \vec{E} = -j\omega \vec{B} \quad (2.9)$$

$$\nabla \times \vec{H} = \vec{J} + j\omega \vec{D} \quad (2.10)$$

At the interface between two media, the boundary conditions for the electric, \vec{E} , and magnetic, \vec{H} , fields, as well as for the electric, \vec{D} , and magnetic, \vec{B} , flux densities are described mathematically by:

$$\vec{n} \times (\vec{E}_1 - \vec{E}_2) = 0 \quad (2.11)$$

$$\vec{n} \times (\vec{H}_1 - \vec{H}_2) = \vec{J}_s \quad (2.12)$$

$$\vec{n} \cdot (\vec{B}_1 - \vec{B}_2) = 0 \quad (2.13)$$

$$\vec{n} \cdot (\vec{D}_1 - \vec{D}_2) = \rho_s \quad (2.14)$$

where \vec{J}_s is the surface current density [A/m²] and ρ_s is the surface charge density [C/m²]. These equations show that the tangential component of \vec{E} and the normal component of \vec{B} are always continuous across the interface. The discontinuities of the tangential term of \vec{H} and of the normal component of \vec{D} are equal to \vec{J}_s and ρ_s , respectively.

2.2 Complex permittivity

Assuming that all the fields are time-harmonic, the phasor notation can be used to express them, i.e., $\vec{X} = \vec{X}_0 \cos(\omega t + \theta_X) = \text{Re}[\vec{X}_0 e^{j(\omega t + \theta_X)}]$. Recalling Equation (2.5) and knowing that:

$$\vec{D} = \epsilon \vec{E} = \epsilon_0 \vec{E} + \vec{P} \quad (2.15)$$

where ϵ_0 is the permittivity in vacuum and \vec{P} is the polarization [C/m²], the vector \vec{D} is the result of the sum of two harmonic waves. Due to polarization of dipole molecules there is a lag in phase between \vec{P} and \vec{E} , i.e., $\theta_E - \theta_P \neq 0$. Knowing that the sum of harmonic waves with the same angular frequency, ω , but with different phase angles, is still an harmonic wave with the same angular frequency, ω , but with different phase angle, $\theta_D \neq \theta_E, \theta_P$, it can be concluded that \vec{D} will not be in phase with \vec{E} . This means that the permittivity, ϵ , must be a complex number:

$$\epsilon = |\epsilon| e^{-j\delta_t} = \epsilon' - j\epsilon'' = \epsilon_0(\epsilon'_r - j\epsilon''_r) \quad (2.16)$$

where ϵ'_r is the real part of the relative permittivity, usually known as dielectric constant and ϵ''_r is the imaginary part of the relative permittivity, known as loss factor. Applying the phasor notation and using Equation (2.16), Equation (2.15) can be rewritten as:

$$\vec{D} = |\epsilon| \vec{E}_0 e^{j(\omega t + \theta_E - \delta_t)} \quad (2.17)$$

where $\delta_t = \tan^{-1}(\epsilon''_r/\epsilon'_r)$ is the phase mismatch between \vec{D} and \vec{E} . In the literature $\tan \delta_t$ is known as the loss tangent and its value gives information about the material ability to absorb microwave radiation and converting it into heat [27]. As it will be seen later, the dielectric constant, ϵ'_r , describes the ability of the material to store electric energy.

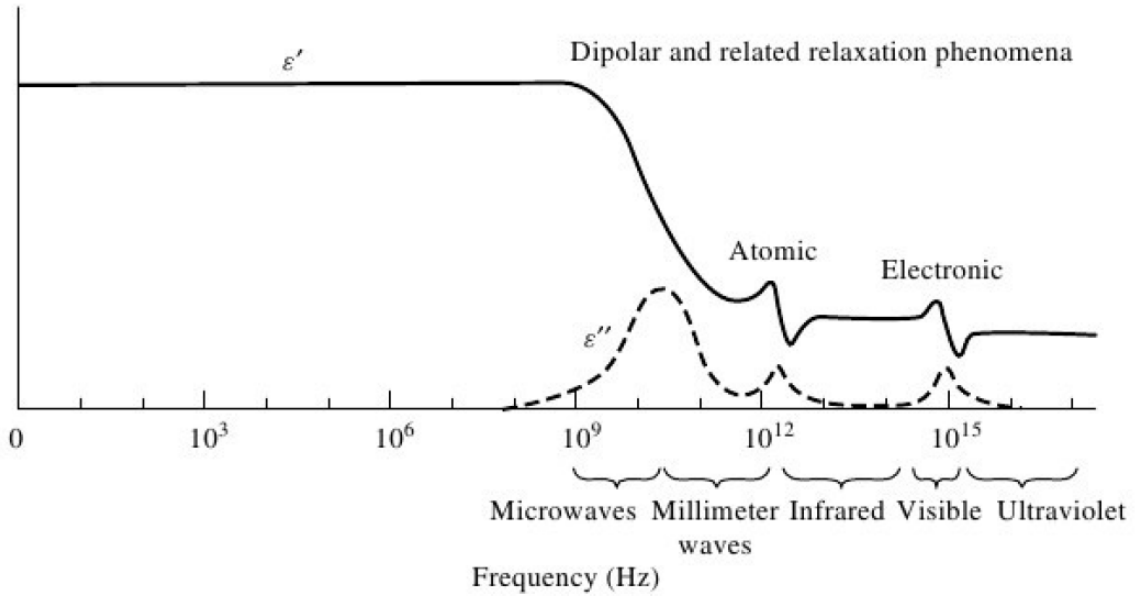


Figure 2.1: Frequency response of dielectric constant and loss factor for a hypothetical dielectric material showing various known phenomena [30].

Permittivity is strongly dependent on the frequency and temperature. Figure 2.1 shows a loss factor peak in the microwave frequency range corresponding to dipolar and related relaxation phenomena, which, as mentioned before, is the main heating mechanism in the microwave heating process. The dependence of the permittivity on temperature is not the same for all materials. In water, for example, it decreases with increasing temperature [28]. In the case of glass and other ceramic materials, after a critical temperature is reached both dielectric constant and loss factor present a very sharp increase with increasing temperature. This behavior is behind the *thermal runaway* phenomenon, already referred to in this text, which must be controlled or avoided.

2.3 Poynting Theorem and microwave dissipated power

The cross product between the electric and magnetic fields is called the Poynting vector, \vec{S} , and has units of W/m^2 , which means that it represents an energy flux density. For a closed surface S , the energy flux, P_f , that crosses it is given by:

$$P_f = \oint_S (\vec{E} \times \vec{H}) \cdot \vec{n} dS \quad (2.18)$$

Using the divergence theorem, it yields:

$$\oint_S (\vec{E} \times \vec{H}) \cdot \vec{n} dS = \iiint_{V_s} \nabla \cdot (\vec{E} \times \vec{H}) dV \quad (2.19)$$

where V_s is the volume enclosed by the surface S .

Recalling the identity vector $\nabla \cdot (\vec{A} \times \vec{B}) = \vec{B} \cdot (\nabla \times \vec{A}) - \vec{A} \cdot (\nabla \times \vec{B})$ and substituting into Equation (2.19), one obtains:

$$\oint_S (\vec{E} \times \vec{H}) \cdot \vec{n} dS = \iiint_{V_s} [\vec{H} \cdot (\nabla \times \vec{E}) - \vec{E} \cdot (\nabla \times \vec{H})] dV \quad (2.20)$$

Substituting Equations (2.1) and (2.2) into Equation (2.20), the following equation is obtained:

$$\oint_S (\vec{E} \times \vec{H}) \cdot \vec{n} dS = \iiint_{V_s} \left[-\vec{H} \cdot \frac{\partial \vec{B}}{\partial t} - \vec{E} \cdot \frac{\partial \vec{D}}{\partial t} - \vec{j} \cdot \vec{E} \right] dV \quad (2.21)$$

Equation (2.21), which consists in an electromagnetic energy balance, expresses the Poynting theorem. It states that the amount of power that leaves the enclosed surface, S , equals the rate of

decrease of stored electric and magnetic energies plus the losses that are dissipated within the volume, V_s . If it is assumed that all the fields are time-harmonic and recalling Equation (2.8) and the trigonometric identity $\cos(x) \cos(y) = 1/2 [\cos(x + y) + \cos(x - y)]$, the Poynting vector can be expressed as:

$$\vec{E} \times \vec{H} = \frac{1}{2} E_0 H_0 [\cos(2\omega t + \theta_E + \theta_H) + \cos(\theta_E - \theta_H)] (\hat{i}_E \times \hat{i}_H) \quad (2.22)$$

where E_0 and H_0 are the electric and magnetic field amplitudes, respectively, and \hat{i}_E and \hat{i}_H are the unit vectors that point in the direction of \vec{E} and \vec{H} , respectively.

The time-average of the instantaneous Poynting vector is given by:

$$\langle \vec{E} \times \vec{H} \rangle_t = \frac{1}{T} \int_T (\vec{E} \times \vec{H}) dt \quad (2.23)$$

Substituting Equation (2.22) into Equation (2.23) and after some algebra, the following equation is obtained:

$$\langle \vec{E} \times \vec{H} \rangle_t = \frac{E_0 H_0}{2} \cos(\theta_E - \theta_H) (\hat{i}_E \times \hat{i}_H) = \frac{1}{2} \text{Re} [\vec{E}_s \times \vec{H}_s^*] \quad (2.24)$$

where \vec{H}_s^* is the complex conjugate of the phasor $\vec{H}_s = \vec{H}_0 e^{j\theta_H}$. The time-averaged power that crosses the enclosed surface S is then given by:

$$\oint_S (\langle \vec{E} \times \vec{H} \rangle_t) \cdot \vec{n} dS = \frac{1}{2} \text{Re} \left[\oint_S (\vec{E}_s \times \vec{H}_s^*) \cdot \vec{n} dS \right] \quad (2.25)$$

By replacing \vec{E} and \vec{H} with \vec{E}_s and \vec{H}_s^* , respectively, in Equations (2.9) and (2.10) and taking into account the constitutive relations, as well as that the permittivity is a complex number, for a dielectric material with relative permeability $\mu_r = 1$, typical in glasses and ceramic materials, one obtains:

$$\nabla \times \vec{E}_s = -j\omega \vec{B}_s = -j\omega \mu_0 \vec{H}_s \quad (2.26)$$

$$\nabla \times \vec{H}_s^* = \vec{J}_s^* - j\omega \vec{D}_s^* = \sigma \vec{E}_s^* - j\omega \epsilon^* \vec{E}_s^* = -j\omega \epsilon_0 \epsilon_r' \vec{E}_s^* + (\sigma + \omega \epsilon_0 \epsilon_r'') \vec{E}_s^* \quad (2.27)$$

where μ_0 is the permeability in vacuum.

Replacing \vec{E} and \vec{H} with \vec{E}_s and \vec{H}_s^* , respectively, in Equation (2.20) and using Equations (2.26) and (2.27), after some manipulation the so-called complex phasor form of the Poynting theorem is obtained:

$$\oint_S (\vec{E}_s \times \vec{H}_s^*) \cdot \vec{n} dS = -j\omega \iiint_{V_s} (\mu_0 H_0^2 - \epsilon_0 \epsilon_r' H_0^2) dV - \iiint_{V_s} (\sigma + \omega \epsilon_0 \epsilon_r'') E_0^2 dV \quad (2.28)$$

Recalling Equation (2.25) and observing Equation (2.28) it can be concluded that its real part represents twice the time-averaged power that crosses the closed surface S . It is important to notice that only the real term of Equation (2.28) contributes to the time-averaged power. The imaginary term is related to the reactive power and describes the rearrangement of energy in the system. The expression:

$$Q = (\sigma + \omega \epsilon_0 \epsilon_r'') \frac{E_0^2}{2} \quad (2.29)$$

which units are W/m^3 , represents the power that is dissipated and converted into heat by Joule effect and mainly by friction mechanisms due to the dipolar relaxation phenomena.

2.4 Momentum and continuity equations

Laminar flow takes place when the Reynolds number is small. This can happen either because the flow velocity is very low, or the fluid viscosity is very high. A laminar, incompressible flow is characterized by the Navier-Stokes momentum equation [31]:

$$\frac{\partial \vec{U}}{\partial t} + \vec{U} \cdot \nabla \vec{U} = -\frac{\nabla P}{\rho} + \nu \nabla^2 \vec{U} \quad (2.30)$$

and by the continuity equation:

$$\nabla \cdot \vec{U} = 0 \quad (2.31)$$

where \vec{U} is the velocity [m/s], P is the pressure [Pa], ρ is the fluid density [kg/m^3] and ν is the kinematic viscosity [m^2/s]. Equation (2.30), which represents a momentum balance for an infinitesimal control volume, states that the acceleration experienced by a fluid particle is induced by a pressure gradient and by viscous stresses. Equation (2.31), which describes a mass balance, shows that for an incompressible fluid, *i.e.*, when ρ is constant, the divergence of the velocity is zero.

2.5 Heat equation

The non-stationary heat transfer process is described by the transient heat equation which gives the thermal field solution:

$$\frac{\partial}{\partial t}(\rho C_p T) + \vec{U} \cdot \nabla(\rho C_p T) = \nabla \cdot (k \nabla T) + Q \quad (2.32)$$

where C_p is the specific heat capacity [$J/(kg \cdot K)$], T is the temperature [K], k is the thermal conductivity [$W/(m \cdot K)$] and Q [W/m^3] is the heat source term. In Equation (2.32), the first term on the left-hand side is the transient one and represents the accumulated energy inside an infinitesimal control volume. When this term approaches zero, the steady-state is being reached. The second term on the left-hand side and the first term on the right-hand side represent the energy convective and diffusive terms, respectively. This second term on the right-hand side, Q , is the power source which enables the coupling of the Maxwell's equations with the heat transfer one, since Q is the time-averaged electromagnetic power dissipated in a dielectric lossy medium with $\mu_r = 1$, which is represented by Equation (2.29), explained in the previous section.

Regarding Equation (2.29), it is important to observe that in the power source term, Q , are present two heating mechanisms, which are the Joule and the dielectric loss effects, represented, respectively, by the following expressions:

$$Q_J = \sigma \frac{E_0^2}{2} \quad (2.33)$$

$$Q_D = \omega \epsilon_0 \epsilon_r'' \frac{E_0^2}{2} \quad (2.34)$$

It can be observed, in Equation (2.34), that the loss factor, ϵ_r'' , plays a decisive role in the conversion of electromagnetic power into heat, as discussed in previous sections. It is also important to notice that in Equation (2.32) the material properties, ρ , C_p and k are not considered as constant, but temperature dependent.

2.6 Microwave basics

This section aims to give the reader some insight on several microwave related concepts which are relevant to better understand all the microwave heating phenomena presented and discussed further in this Thesis.

2.6.1 Penetration depth

The penetration depth, δ [m], is an extremely important parameter in microwave heating. By definition δ is the depth within the material where the external electric field amplitude has dropped to $1/e$, approximately 37%, of its value at the material surface. The value of the penetration depth is given by [11]:

$$\delta = \frac{c}{2\pi f(2\epsilon_r')^{1/2}} \left\{ \left[1 + \left(\frac{\epsilon_r''}{\epsilon_r'} \right)^2 \right]^{1/2} - 1 \right\}^{-1/2} \quad (2.35)$$

where $c = 1/\sqrt{\mu_0\epsilon_0}$ is the speed of light in vacuum [m/s].

Regarding Equation (2.35) it can be concluded that the penetration depth is influenced by the working frequency, f , decreasing as the frequency increases. It is also dependent on the dielectric constant, ϵ_r' , and on the loss tangent, ϵ_r''/ϵ_r' , decreasing as both parameters increase. It can be shown that, when the electromagnetic radiation hits a load, almost 90% of the power absorption occurs within a thickness equal to δ . To take advantage of the volumetric heating effect, the thickness of the load that is heated should be equal to δ .

2.6.2 Microwave cavities

In microwave heating, the cavity geometry has an important impact on the efficiency of the process, mainly due to resonance phenomena. When microwave radiation enters the cavity, it will be reflected by its metallic walls. When the reflected waves interact with the incoming ones, standing waves are created either by constructive or destructive interference. When constructive interference happens, these interactions give rise to resonant modes that depend on the frequency and on the cavity geometry. For example, for an empty rectangular cavity with dimensions a , b , and d along x , y and z directions, respectively, the resonant modes will be described by:

$$\left(\frac{l\pi}{a} \right)^2 + \left(\frac{m\pi}{b} \right)^2 + \left(\frac{n\pi}{d} \right)^2 = \left(\frac{\omega_{lmn}}{c} \right)^2 \quad (2.36)$$

where l , m and n correspond to the number of wave half-wavelengths along x , y and z directions, respectively.

Microwave cavities with a geometry that allow the development of only one resonant mode are called single-mode cavities, which provide a better control over the microwave heating process due to the predictability of the field across the cavity. These cavities provide higher heating efficiencies because it is easy to control the location of the electric field peaks by moving a shorting plunger. However, single-mode cavities are not suitable for heating large size loads, which constitutes a limiting factor to scale-up these processes [9].

Multi-mode cavities are designed to accommodate multiple resonant modes. To accomplish that, these cavities are larger than single-mode ones, which leads to the distribution of electromagnetic energy over a larger space and consequently to a lower, more uniform electric field distribution. This means that to achieve the same electric field magnitude in a multi-mode as in a single-mode cavity, higher power is required. This better heating uniformity causes a decrease in the influence that the location of the load inside the cavity exerts on the microwave efficiency. Multi-mode cavities allow for larger loads to be heated, giving them better scale-up potential. However, besides the higher power

required, in multi-mode cavities, small changes in dielectric properties of the load can significantly influence the entire electric field distribution which leads to difficulties in the heating control [9, 23].

2.6.3 Rectangular waveguide

Waveguides consist of a structure that transmits electromagnetic waves. Rectangular cross sectioned waveguides can propagate transverse electric, TE, or transverse magnetic, TM, waves which are waves with no field component in the direction of propagation. The cut-off frequency of a waveguide, f_c [Hz], is a critical frequency under which no wave propagation occurs, as all field components will decay exponentially away from the radiation source. For a rectangular waveguide with cross section dimensions of a and b , along x and y directions, respectively, the cut-off frequency for a transverse wave propagating in the z direction is given by:

$$f_c = \frac{c}{2\pi} \sqrt{\left(\frac{m\pi}{a}\right)^2 + \left(\frac{n\pi}{b}\right)^2} \quad (2.37)$$

where m and n can take the values $m = 0, 1, 2, \dots$ and $n = 0, 1, 2, \dots$, but $(m, n) \neq (0, 0)$.

Assuming that $a > b$, the smallest cut-off frequency occurs when $m = 1$ and $n = 0$, which corresponds to the TE_{10} mode, which is the dominant one. For a given frequency, if the cavity dimensions are designed to only allow the propagation of the TE_{10} mode, then the waveguide behaves as a single-mode cavity. It is important to note that if assigning $m = 1$ and $n = 0$ into Equation (2.37), it follows that:

$$f_{c_{10}} = \frac{c}{2a} \quad (2.38)$$

and knowing the relation between the wavelength and the frequency, $\lambda = c/f$ [m], it can be concluded that if $a < \lambda_{c_{10}}/2$ there will be no wave propagation at all, and the electric field will decay exponentially as it moves away from the source.

The guide wavelength, λ_g [m], which is the distance between field peaks inside a waveguide is different from the one of a plane-wave propagating freely, λ_0 [m], and is given by [32]:

$$\lambda_g = \lambda_0 \left(\sqrt{1 - f_{c_{10}}^2 / f^2} \right)^{-1} \quad (2.39)$$

2.7 Numerical simulations with *COMSOL Multiphysics*

It was shown in this chapter that the process of microwave heating involves the coupling of the Maxwell's and heat equations. Since the thermal and dielectric properties of glass are highly dependent

on temperature, an iterative method is necessary to obtain a coupled solution. The objective of this section is to present to the reader the basis of such coupled algorithm.

COMSOL Multiphysics was the selected software to perform such calculations due to its ability to couple different physics in the same numerical simulation and mainly because it has been extensively used in microwave heating problems with validated results [16-18, 20].

If it is assumed that the electromagnetic fields are harmonic and the frequency is fixed, some simplifications can be made in the Maxwell's equations. Recalling Equations (2.9) and (2.10) and the constitutive relations:

$$\nabla \times \vec{E} = -j\omega\vec{B} = -j\omega\mu_0\mu_r\vec{H} \quad (2.40)$$

$$\nabla \times \vec{H} = \vec{J} - j\omega\vec{D} = j\omega\epsilon_0\epsilon_r'\vec{E} + (\sigma + \omega\epsilon_0\epsilon_r'')\vec{E} \quad (2.41)$$

By using the curl operation in Equation (2.40), it yields:

$$\nabla \times \frac{1}{\mu_r}(\nabla \times \vec{E}) = -j\omega\mu_0(\nabla \times \vec{H}) \quad (2.42)$$

and by replacing Equation (2.41) into Equation (2.42) and knowing that $k_0 = \omega\sqrt{\mu_0\epsilon_0}$ [m^{-1}] is the wave-number in vacuum, the Helmholtz equation in the frequency domain is obtained:

$$\nabla \times \frac{1}{\mu_r}(\nabla \times \vec{E}) - k_0^2\epsilon_r'\vec{E} + jk_0^2\left(\frac{\sigma}{\omega\epsilon_0} + \epsilon_r''\right)\vec{E} = 0 \quad (2.43)$$

Given an initial temperature distribution, the electric field is calculated using Equation (2.43). The microwave power dissipated is then calculated using Equation (2.29) and introduced in the heat equation. After that, the thermal field is computed using Equation (2.32) and the temperature dependent properties are updated, before the Helmholtz equation is solved again. This iterative scheme is repeated until a solution is achieved. It is important to note that the frequency domain equation can be used because the electromagnetic timescale is much smaller than the heat transfer one.

Since the density of glass is a function of temperature, the velocity field calculation should be included in the iterative method described above. To avoid this, it was assumed a constant density value for the microwave heating simulations. Since the maximum deviation from the mean density value used in the calculations was 100 kg/m^3 , corresponding to 4.5%, the velocity field was calculated separately and then imported to the microwave heating model. Keeping the velocity field independent of the temperature field facilitates the convergence and allows for significant savings in the computational resources.

Chapter 3

Numerical model

In this chapter the *COMSOL* numerical model will be described. In Section 3.1, the geometry of the microwave heating system is presented, followed by a description of the electromagnetic, thermal and flow domains. Section 3.2 aims to list the materials used in this Thesis and to present their physical properties. The boundary and initial conditions for the simulations are discussed in Section 3.3. A description of the numerical modelling for the glass phase change is addressed in Section 3.4. Section 3.5 deals with the mass and energy balance calculations for the microwave cavity control volume and finally in Section 3.6, the *MATLAB* microwave heating controller algorithm, which aims to get a steady-state solution with higher efficiency and lower power input as possible, is described.

3.1 Geometry and simulation domains

In order to numerically simulate the glass melting process, a geometry of the microwave cavity was defined, which consists of a rectangular waveguide behaving as a single-mode cavity vertically trespassed by an applicator tube, where the glass flows. The exterior walls of the cavity and tube are covered by an insulation material intended to minimize the thermal losses. For a better visualization, the geometry described above is depicted in Figure 3.1.

The standard WR-340 waveguide has an inner cross section with dimensions of 86.36×43.18 mm and a total length of 325 mm. Recalling Equation (2.37), it can be concluded that for a frequency of 2.45 GHz, this waveguide behaves as a single-mode cavity with a TE_{10} mode of propagation. From Equation (2.39), with a frequency of 2.45 GHz and knowing that in air, $\lambda_0 = 122$ mm, the guide wavelength is found to be $\lambda_g = 174$ mm. The cavity length was chosen in order to allow the moving plunger to travel a distance greater than λ_g so that maximum microwave absorption efficiency can be achieved as it will be seen later.

The glass flows vertically, and the material enters the tube in powder form at room temperature and should leave the outlet section in molten state at an average temperature defined by the user. The applicator tube has a thickness of 6.5 mm that was kept constant along this work. Near the outlet, an obstruction to the flow was introduced to prevent the powder from falling directly from the inlet. Rotation

of the applicator tube was considered and its influence in the heating process was studied as it will be seen later.

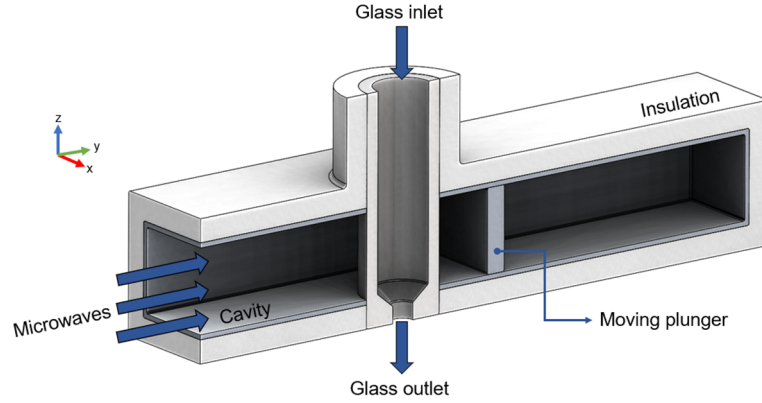


Figure 3.1: Microwave cavity geometry designed for the numerical study of the glass melting process.

The microwave cavity is filled with air and its length is controlled by the plunger position. Since the electromagnetic field is strongly dependent on the thermal one and as it will be discussed later and also referred in the work of Mimoso *et al.* [19], if the plunger is kept in a fixed position, the microwave efficiency will converge to a low value. In order to keep the electric field peak near the material location, maximizing the microwave efficiency, the plunger position varies during the heating process. The microwave radiation enters the cavity in the direction represented by the identified arrows of Figure 3.1.

As it was explained in Section 2.7, the numerical simulations performed in this Thesis involve an iterative method to couple two different physics: electromagnetism and heat transfer. As explained before, the laminar flow calculations were not coupled with the other physics since a constant density was considered for the glass. To prevent unnecessary calculations, it is important to identify the domains where each set of equations must be solved. Figure 3.2a shows the regions where the Helmholtz equation in the frequency domain is solved. These regions consist of the interior of the cavity before the moving plunger, the applicator tube and the glass.

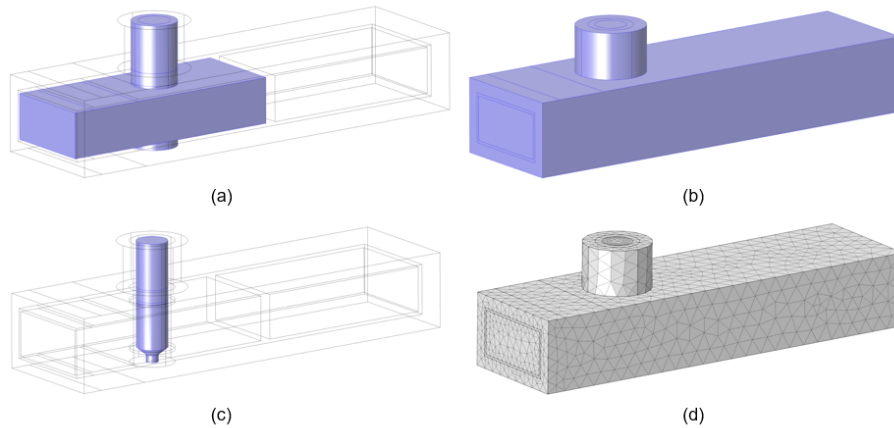


Figure 3.2: Presentation of the (a) electromagnetic domain, (b) thermal domain and (c) flow domain. The computational mesh with 74837 tetrahedral elements is shown in illustration (d).

The heat equation, whose source term depends on the Helmholtz equation, must be solved in all regions, as depicted in Figure 3.2b. The Navier-stokes and continuity equations are solved only in the glass region, since the other regions represent static materials with a null velocity. Figure 3.2c presents the glass region where the laminar flow interface is assigned. In Figure 3.2d, the computational mesh used in this work is represented. It is composed by 74837 tetrahedral elements and it can be observed that the mesh is more refined in the glass domain.

3.2 Material properties

In this section, the materials used in each domain are presented as well as their physical properties. As it was referred before, the microwave cavity is filled with air, whose properties were taken from the *COMSOL* materials database.

For the cavity walls and moving plunger, an aluminum alloy, AW 7022, was chosen as suggested in [33]. For this material, the density, ρ , the thermal conductivity, k , and the specific heat capacity, C_p , were assumed constant and can be found in the work of Berger *et al.* [34]. The surface emissivity, ε , was taken from the study of Bartl and Baranek [35]. These values are listed in Table 3.1.

Table 3.1: Aluminum alloy AW 7022 physical properties.

Property	Value
ρ [kg/m ³]	2800
k [W/(m · K)]	135
C_p [J/(kg · K)]	860
ε	0.06

Concerning the applicator tube, the material selected was boron nitride due to its high operating temperature and its microwave transparency behavior. In the work of Behrend *et al.* [36] values for the density, ρ , for the dielectric constant, $\epsilon'_r(T)$, and for the loss factor, $\epsilon''_r(T)$, can be found. The density was assumed constant, but the dielectric properties were considered as temperature dependent. The studies of Simpson and Stuckes [37] and of Solozhenko [38] present information about the boron nitride thermal conductivity and specific heat capacity variation with the temperature, $k(T)$ and $C_p(T)$, respectively. Sridharan *et al.* [39] provides data for the surface emissivity, ε .

The values of the properties assumed as constant are presented in Table 3.2. The temperature dependence of the specific heat capacity, $C_p(T)$, is given by Equation (3.1), valid for temperatures between 0 and 1200 K, in units of J/(kg · K). Figures 3.3 and 3.4 show the temperature dependent curves of the boron nitride thermal conductivity, $k(T)$, and dielectric properties, $\epsilon'_r(T)$ and $\epsilon''_r(T)$, for the temperature ranges given by the respective references.

Table 3.2: Boron nitride physical properties.

Property	Value
ρ [kg/m ³]	2100
ε	0.8

$$C_p(T) = 1865.25 \left(\frac{T^2}{T^2 - 18.727 + 67447.464} \right)^2 \quad (3.1)$$

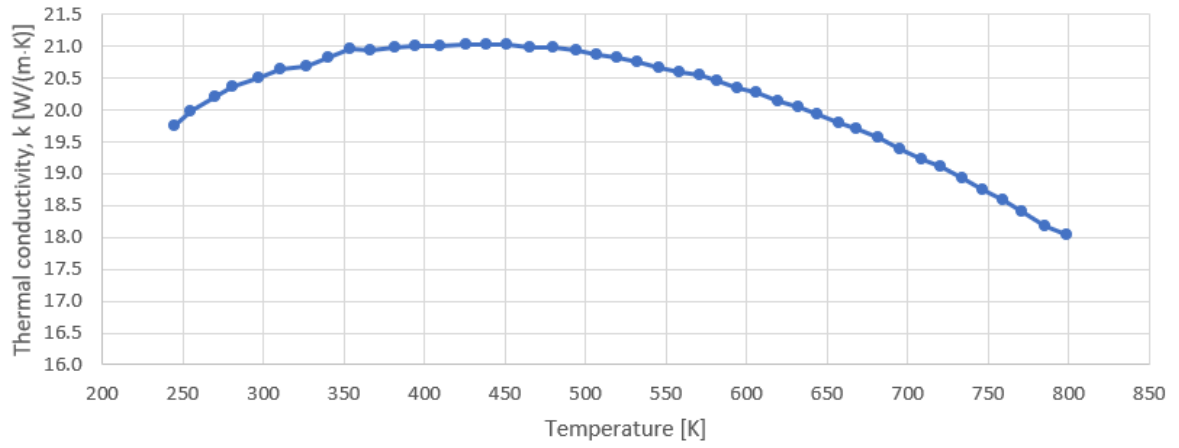


Figure 3.3: Boron nitride thermal conductivity temperature dependence, $k(T)$ [W/(m · K)].

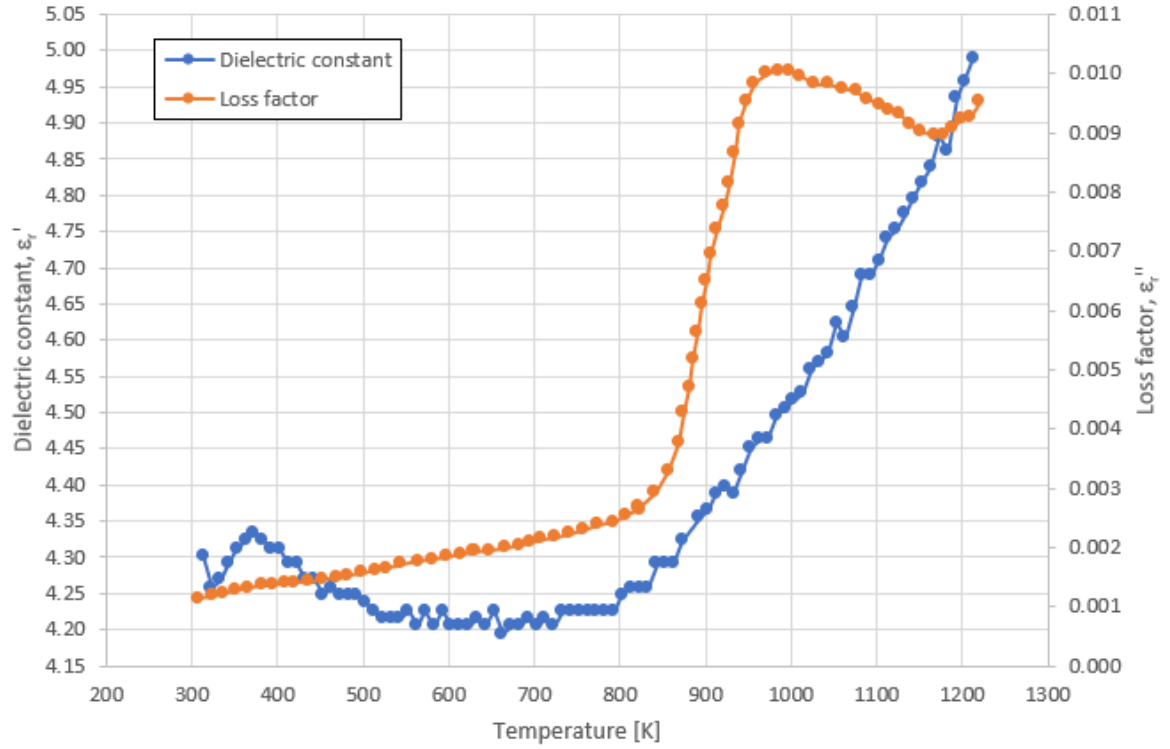


Figure 3.4: Boron nitride dielectric properties temperature dependence, $\varepsilon'_r(T)$ and $\varepsilon''_r(T)$.

As mentioned above, the data for the temperature dependent properties are given for a specific range of temperatures. For the numerical simulations, some extrapolations were made in order to obtain the properties values for temperatures out of the range provided. Linear extrapolations were made for all properties except for the loss factor which was considered to stabilize for the constant value of 0.0095 for temperatures higher than 1200 K.

For the thermal insulation, an alkaline earth silicate wool was considered. Concerning its physical properties, data for the density, ρ , and thermal conductivity, k , can be found in the work of Modarresifar *et al.* [40]. For the specific heat capacity, C_p , glass mineral wool data obtained in the study of Rossi and Rocco [41] was used. These properties are showed in Table 3.3.

Table 3.3: Alkaline earth silicate wool thermal properties.

Property	Value
ρ [kg/m ³]	160
k [W/(m · K)]	0.25
C_p [J/(kg · K)]	1030

It was considered that the exterior surface of the insulation wool was covered by a thin aluminum sheet in order to reduce the radiation thermal losses, since the aluminum emissivity is much smaller than the alkaline earth silicate one [42]. This thin sheet was not considered in the simulations because it was assumed that its temperature would be the same as the temperature of the exterior surface of the insulation, due to the aluminum high thermal conductivity and its very small thickness. For that reason, a surface emissivity value of $\varepsilon = 0.06$ was attributed directly to the insulation material.

Soda-lime silica glass was the material chosen to be processed and studied in this Thesis. Data for the density, $\rho(T)$, dielectric constant, $\epsilon'_r(T)$, and loss factor, $\epsilon''_r(T)$, were provided by *Microwave Properties North* [43], which is a company that measures the dielectric properties of materials up to very high temperatures, and are shown in Figure 3.5 and 3.6, respectively. These properties were measured for a glass whose composition is presented in Table 3.4.

Table 3.4: Chemical composition of the soda-lime silica glass studied in this work.

SiO ₂	Na ₂ O	CaO	MgO	SO ₃	Al ₂ O ₃	Fe ₂ O ₃
73.050%	13.750%	8.830%	3.840%	0.262%	0.120%	0.106%

In order to obtain the temperature dependent curves of the thermal conductivity, $k(T)$, and specific heat capacity, $C_p(T)$, for this specific glass composition, a mass weighted method was applied considering the data found in the literature for each component. Information about the thermal conductivity can be found in the studies of Carniglia and Barna [44], Tatli *et al.* [45] and Aurkari [46]. As for the specific heat capacity, information can be obtained in the work of Green *et al.* [47]. A comparison made with property values given in other references, namely [48] and [49], shows good agreement with the

ones obtained with the mass weighted method, except for the values of the specific heat capacity at low temperatures which led to a correction in this temperature range. These curves are shown in Figures 3.7 and 3.8, respectively.

A reference value for the emissivity of glass powder, ε , and for the glass melting temperature, T_m , can be found in the work of Albouchi *et al.* [50] and Pilon *et al.* [51], respectively. Concerning the value of the latent heat of fusion, L_f [J/kg], a mass weighted value was obtained with the information found in [47]. This value was validated by comparison with the one given by Hossain *et al.* [52]. Data for the dynamic viscosity, μ_v [Pa · s], can be found in the work of Napolitano and Hawkins [53]. These values are presented in Table 3.5. During the numerical simulations, for all the curves presented below, a linear extrapolation was used for temperatures outside of the ranges, which were defined by the data available in the literature.

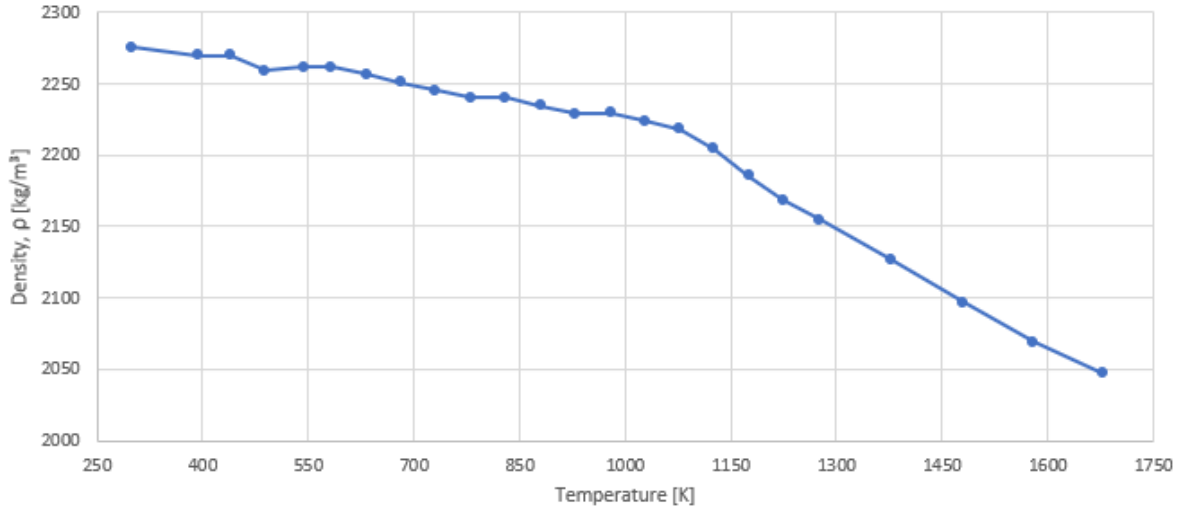


Figure 3.5: Soda-lime silica glass density temperature dependence, $\rho(T)$ [kg/m³].

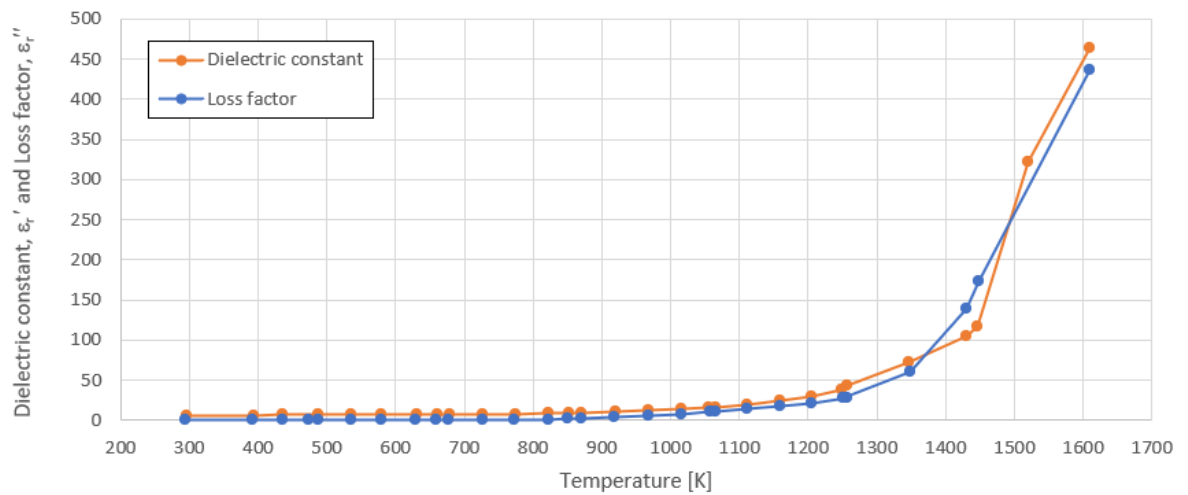


Figure 3.6: Soda-lime silica glass dielectric constant, $\epsilon'_e(T)$, and loss factor, $\epsilon''_e(T)$, temperature dependence.

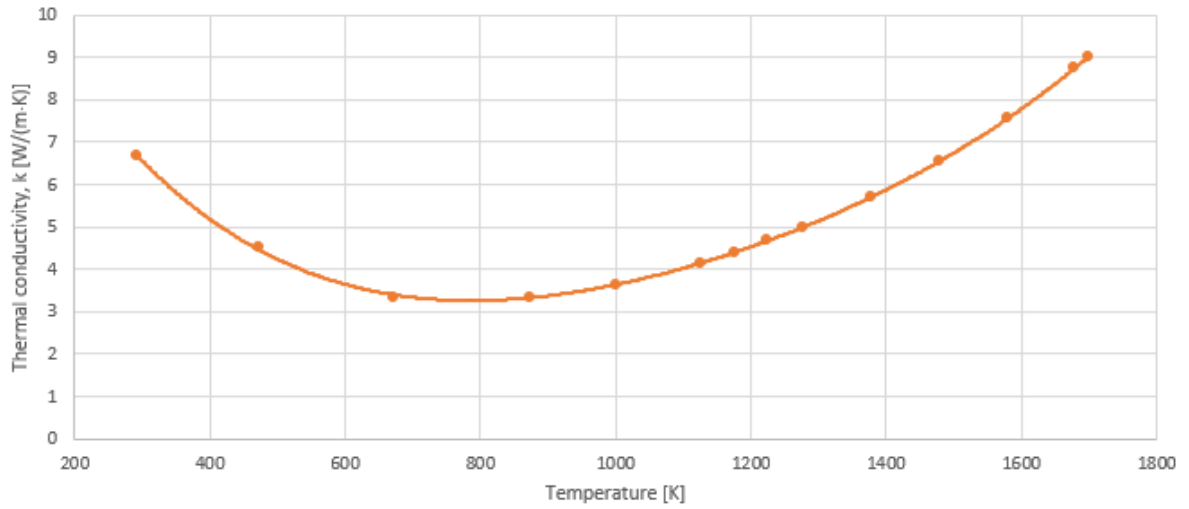


Figure 3.7: Soda-lime silica glass thermal conductivity temperature dependence, $k(T)$ [W/(m · K)].

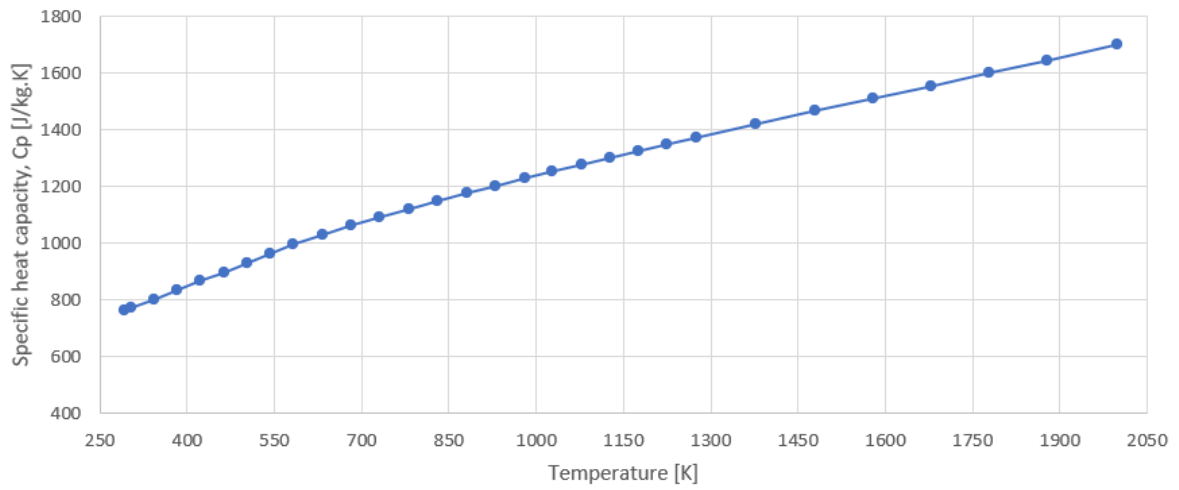


Figure 3.8: Soda-lime silica glass specific heat capacity temperature dependence, $C_p(T)$ [J/(kg · K)].

Table 3.5: Glass emissivity, melting temperature, latent heat of fusion and dynamic viscosity.

Property	Value
ε	0.96
T_m [K]	1450
L_f [kJ/kg]	388
μ_v [Pa · s]	100

3.3 Boundary and initial conditions

In this section, the boundary and initial conditions for the numerical model are described. Firstly, the boundary and initial conditions for the electromagnetic field are addressed, followed by the descrip-

tion of the ones for the thermal field. Finally, the laminar flow boundary and initial conditions are presented.

3.3.1 Electromagnetic interface

A frequency domain electromagnetic interface was assigned to solve the Helmholtz equation, since all the simulations performed in this work used a single value for the frequency of the microwaves, $f = 2.45$ GHz. The domains assigned to this interface have already been described and are shown in Figure 3.2.

All the boundaries of the wave equation domain were considered as *perfect electric conductor*, except for the cavity inlet and tube inlet and outlet boundaries, where *port* and *scattering* boundary conditions were used, respectively, as shown in Figure 3.9. In this study, the *port* boundary simulates the inlet of a TE_{10} wave with a specified power, P_{in} [W], at a 2.45 GHz fixed frequency. The *scattering* boundary condition enables the flux of electromagnetic radiation out of the computational domain, simulating, therefore, microwave leakage in those boundaries.

As for the initial conditions, the electric field is set to zero everywhere in the electromagnetic domain. Pressure is assumed to be 1×10^5 Pa, *i.e.*, 1 atm, everywhere. The electromagnetic interface is coupled with the thermal interface through the temperature field.

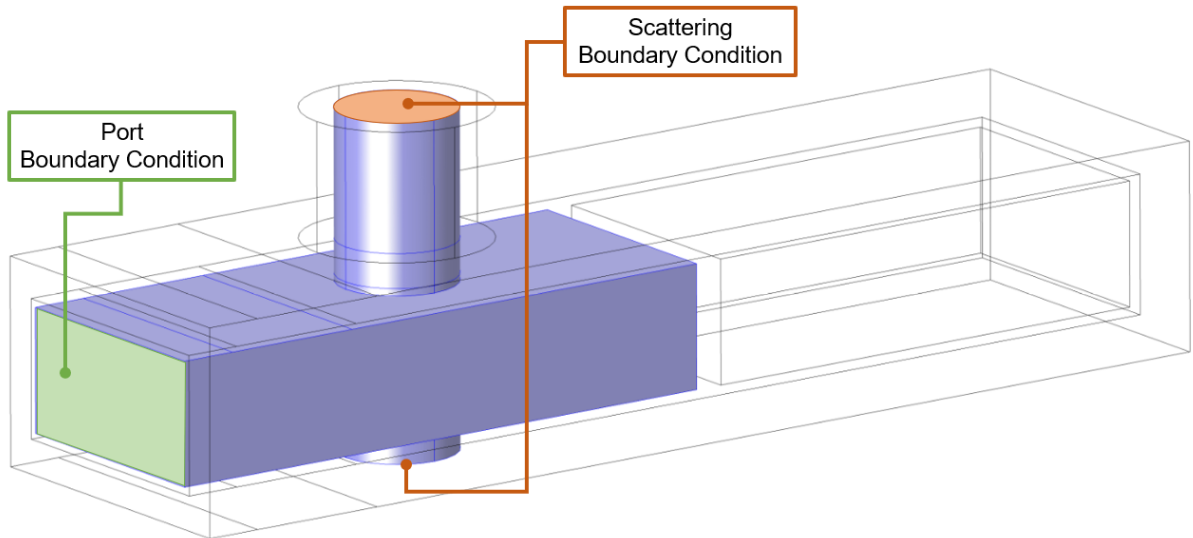


Figure 3.9: Electromagnetic interface domain. Location of the *port* and *scattering* boundaries.

3.3.2 Thermal interface

To solve the heat equation, the *heat transfer in solids* interface was designated. As mentioned before and illustrated in Figure 3.2, all the regions were selected in this interface. Concerning the

boundary conditions used in this interface, an *outflow*, *i.e.*, adiabatic boundary condition was given to the applicator tube outlet surface, which means that there is no heat flux across it. This assumption is valid considering that the molten glass keeps its temperature and velocity profiles constant after exiting the tube.

Radiation and natural convection heat fluxes were imposed to the exterior surfaces of the microwave cavity and the ambient temperature, T_{amb} , was set to 293 K. These imposed heat fluxes [W/m²] are driven by the temperature difference between the surface and the ambient temperatures, and they account for the thermal losses of the microwave cavity. These fluxes are computed by the following equations:

$$q_R = \varepsilon \sigma_b (T_s^4 - T_{amb}^4) \quad (3.2)$$

$$q_C = h(T_s - T_{amb}) \quad (3.3)$$

where ε is the emissivity of the surface, σ_b is the Stefan-Boltzmann constant [W/(m² · K⁴)], T_s is the surface temperature [K] and h is the convection coefficient [W/(m² · K)].

The convection coefficients, h , were calculated for all the exterior surfaces depending on their orientation relatively to the gravitational vector, \vec{g} , using empirical correlations found in the literature, which are relationships established between measured data. The orientation of the surfaces is important in the calculation of the convection coefficients, h , because these depend on the air flow driven by buoyancy forces. The lateral and rear external surfaces of the microwave cavity were assumed to be isothermal vertical plates. The top and bottom surfaces of the cavity and tube were assumed to be the top and bottom surfaces of an isothermal horizontal plate, respectively. The insulation external cylindrical surfaces around the tube were also assumed to be as isothermal vertical plates since the thickness of the boundary layer, δ_{BL} , is much smaller than the external diameter of the insulation around the tube, d_{ext} . This assumption can be established if [48]:

$$\frac{d_{ext}}{L} \leq \frac{35}{Gr_L^{1/4}} \quad (3.4)$$

where L is the cylinder height [m] and $Gr_L = g\beta(T_s - T_\infty)L^3/\nu^2$ is a non-dimensional parameter called Grashof number that represents the ratio between buoyancy and viscous forces, where g is the gravitational acceleration [m/s²], $\beta = -1/\rho (\partial\rho/\partial T)_p$ is a thermodynamic property of the fluid designated by volumetric thermal expansion coefficient [K⁻¹], T_s is the surface temperature [K], T_∞ is the temperature of the fluid away from the surface [K] and ν is the kinematic viscosity of the fluid [m²/s].

Here it is important to introduce the reader to some other important non-dimensional parameters that appear in the convection coefficient correlations presented below. Firstly, the average Nusselt number, \overline{Nu}_L , defined as:

$$\overline{Nu}_L = \bar{h}L/k \quad (3.5)$$

where \bar{h} is the surface average convection coefficient [$\text{W}/(\text{m}^2 \cdot \text{K})$], L is the characteristic length of the surface [m] and k is the fluid thermal conductivity [$\text{W}/(\text{m} \cdot \text{K})$]. For a vertical plate, L is its height. However, for a horizontal plate L is given by the ratio between the surface area, A_s , and its perimeter, P_s , i.e., $L = A_s/P_s$. Secondly, the Prandtl number, Pr , which is defined as:

$$Pr = \nu/\alpha \quad (3.6)$$

where α is the thermal diffusivity of the fluid [m^2/s]. It represents the ratio between the momentum and thermal diffusivity. Finally, the Rayleigh number, Ra_L , is defined as:

$$Ra_L = Gr_L Pr = \frac{g\beta(T_s - T_\infty)L^3}{\nu\alpha} \quad (3.7)$$

As mentioned before, in this study, the fluid considered was air and all its thermal properties were calculated for the so-called film temperature, $T_f = (T_s + T_\infty)/2$, using the data tables found in [48]. Air flows near vertical and horizontal plates are illustrated in Figure 3.10.

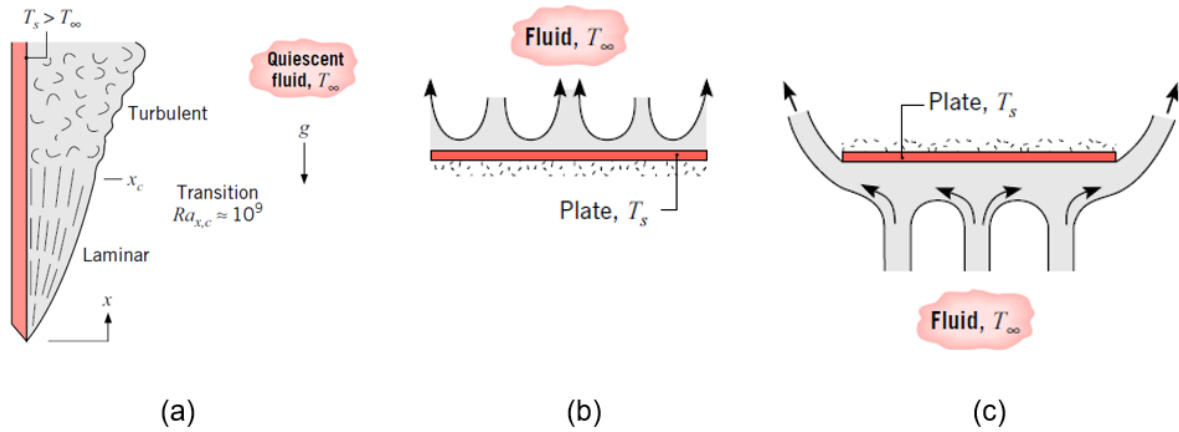


Figure 3.10: Air flows induced by (a) hot vertical plate, (b) hot horizontal plate located below the air and (c) hot horizontal plate located above the air [48].

For an isothermal vertical plate, the average Nusselt number, is computed with the Churchill & Chu correlation, valid for all values of Ra_L and given by [48]:

$$\overline{Nu}_L = \left\{ 0.825 + \frac{0.387 Ra_L^{1/6}}{[1 + (0.492/Pr)^{9/16}]^{8/27}} \right\}^2 \quad (3.8)$$

For the top hot horizontal plate located below the air, the following correlations, valid for $1 \leq Ra_L \leq 10^{10}$, were used for the calculation of the average Nusselt number [54]:

$$\bar{C}_l = \frac{0.671}{[1 + (0.492/Pr)^{9/16}]^{4/9}} \quad (3.9)$$

$$\overline{Nu^T} = 0.835 \bar{C}_l Ra_L^{1/4} \quad (3.10)$$

$$\overline{Nu}_l = \frac{1.4}{\ln(1 + 1.4/\overline{Nu^T})} \quad (3.11)$$

$$\overline{Nu}_t = 0.14 \left(\frac{1 + 0.0107Pr}{1 + 0.01Pr} \right) Ra_L^{1/3} \quad (3.12)$$

$$\overline{Nu}_L = [(\overline{Nu}_l)^{10} + (\overline{Nu}_t)^{10}]^{1/10} \quad (3.13)$$

For the hot horizontal plate located above the air, the following correlations, valid for $10^3 \leq Ra_L \leq 10^{10}$, were used to get the average Nusselt number [54]:

$$\overline{Nu^T} = \frac{0.527}{[1 + (1.9/Pr)^{9/10}]^{2/9}} Ra_L^{1/5} \quad (3.14)$$

$$\overline{Nu}_L = \frac{2.5}{\ln(1 + 2.5/\overline{Nu^T})} \quad (3.15)$$

Once the average Nusselt number is calculated for the desired range of temperatures, the average convection coefficient, \bar{h} , is obtained for every surface using Equation (3.5).

To consider the energy exchange by radiation between the interior walls of the microwave cavity, the *diffuse surface* boundary condition was applied in those regions simulating surface-to-surface radiative heat fluxes, using the hemicube method that accounts for the view factors between surfaces. The view factor, F_{ij} , is the fraction of radiation leaving surface i that is intercepted by surface j . For an enclosure with N surfaces filled with a transparent medium, the power, Q_i , that leaves surface i is given by:

$$Q_i = \frac{\sigma_b T_i^4 - J_i}{\frac{1 - \varepsilon_i}{\varepsilon_i A_i}} = \sum_{j=1}^N A_i F_{ij} (J_i - J_j) \quad (3.16)$$

where T_i , A_i and ε_i are the temperature, area and emissivity of surface i , respectively. The radiosity, J_i , is related to the emissive power and to the irradiation, H_i as:

$$J_i = \varepsilon_i \sigma_b T_i^4 + (1 - \varepsilon_i) H_i = \varepsilon_i \sigma_b T_i^4 + (1 - \varepsilon_i) \sum_{j=1}^N F_{ij} J_j \quad (3.17)$$

Finally, at the applicator tube inlet, a *heat flux* boundary condition was applied. This heat flux, integrated over the inlet area, S_{in} , is given by:

$$Q_{in} = \iint_{S_{in}} \left[\rho(\vec{U} \cdot \vec{n}) \int_{T_0}^T c_p(T) dT \right] dA \quad (3.18)$$

where \vec{U} is the local velocity [m/s], \vec{n} is the surface unit normal vector, T_0 is the temperature at which the glass is introduced in the system [K], defined as $T_0 = 293 \text{ K}$, and T is the local temperature [K]. From Equation (3.18) it can be seen that Q_{in} represents the power required to rise the glass temperature from T_0 to T , assuming that the velocity, \vec{U} , and that the specific heat capacity, $c_p(T)$, are not constant along the surface. The use of this *heat flux* boundary condition avoids the need to simulate a longer tube with a *fixed temperature* boundary condition at the inlet which would require more finite elements and, consequently, more computational resources. Both models, long tube with *fixed temperature* boundary condition and smaller tube with *heat flux* boundary condition are illustrated in Figure 3.11.

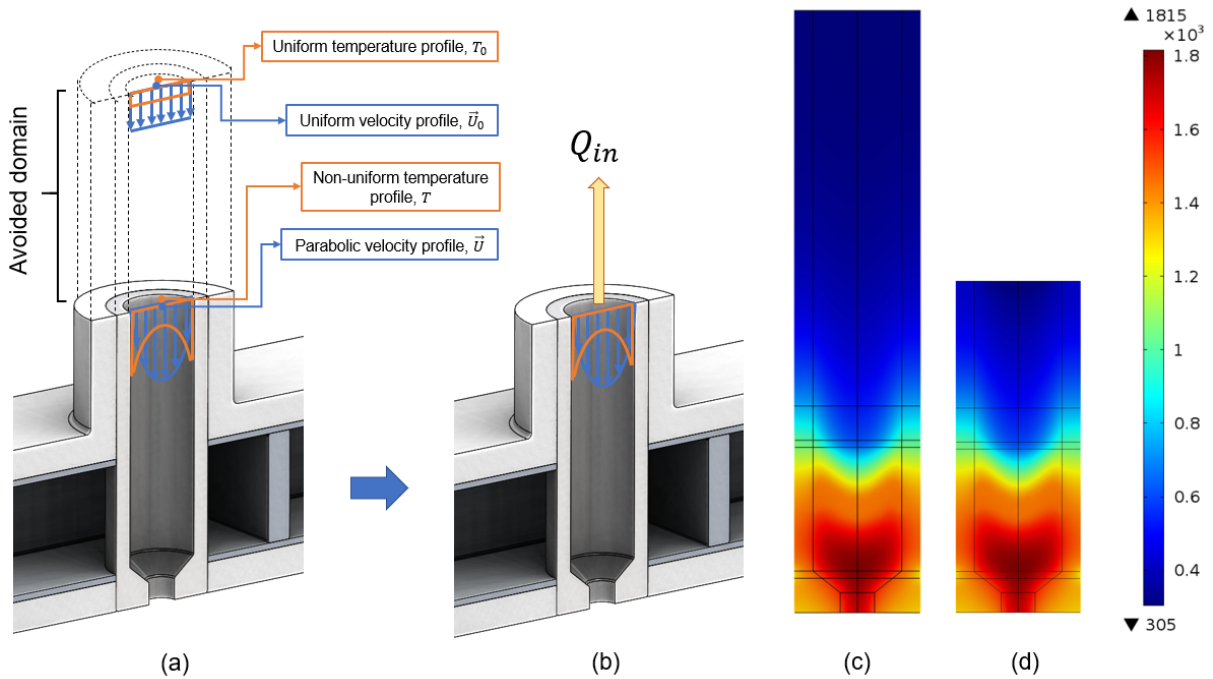


Figure 3.11: Applicator tube inlet boundary condition in the models with (a) fixed temperature and (b) heat flux. Converged thermal solution for the (c) fixed temperature, and (d) heat flux models.

In order to verify the equivalence of both models, two simulations were made without the electromagnetic equations. Instead, a power source assigned to the glass domain was used to simulate the microwave heat absorption by the material. The converged solutions for the thermal field in the applicator tube and glass domains are shown in Figure 3.11. As it can be seen, both models have the same temperature field which means that the *heat flux* boundary condition applied to the tube inlet allows to reduce the computational domain while obtaining the same results.

As for the initial conditions assigned to the thermal interface, a temperature of 293 K was set to all domains except for the glass region, where a linear temperature profile was assigned, with a value of 293 K at the inlet and a value of 1293 K at the outlet. Since at low temperatures the glass loss factor is very low, this material poorly absorbs microwave radiation at those temperatures. An initial preheat

with another heating mechanism, or the use of a susceptor, a highly absorber material at low temperatures, which can be mixed with the glass powder, is necessary to help activating the microwave energy absorption, while the glass is transparent to the radiation because of the low values of its dielectric properties. The initial temperature field in the glass accounts for an that initial heating mechanism [22].

3.3.3 Flow interface

For the temperature range $293 \leq T \leq 1800$ K the average glass density value is calculated by:

$$\rho_{ave} = \frac{1}{(1800 - 293)} \int_{293}^{1800} \rho(T) dT = 2205.1 \text{ kg/m}^3 \quad (3.19)$$

As stated before, and observing Figure 3.5, the maximum deviation of the glass density from the average value is less than 4.5%, thus it was assumed a constant value for the glass density of $\rho = 2205.1 \text{ kg/m}^3$. While considering a constant value for the density, it was not required to couple the Navier-Stokes equations with the heat equation saving, therefore, considerable computational resources. The glass velocity field was calculated in a separate model with the *laminar flow* interface and then imported to the electromagnetic-thermal model.

With respect to the boundary conditions applied to the flow interface, the inner walls of the applicator tube were modelled with a *no-slip* boundary condition. This boundary condition is realistic when the glass is already in liquid state. However, when the glass is still in solid state, as a powder, a *slip* boundary condition should be applied. In order to keep the numerical model as simple as possible, the *no-slip* boundary condition was adopted. The influence of this choice will be analyzed in a later section. For the inlet surface a *mass flow* boundary condition was applied and atmospheric pressure was imposed at the outlet surface.

With respect to the initial conditions, the velocity along x and y were set to zero and along z , *i.e.*, along the direction of the flow, the initial velocity was set to be equal to the average inlet velocity:

$$U_z = - \frac{\dot{m}}{\rho_{ave} \pi d_i^2 / 4} \quad (3.20)$$

where \dot{m} is the mass flow rate [kg/s] and d_i is the tube inner diameter [m].

3.4 Phase change numerical modelling

As it is well known, for a pure substance phase-change occurs at constant temperature because all the energy received is being used to change the material's molecular structure instead of rising its temperature. The energy required to melt 1 kg of a material is known as the latent heat of fusion, L_f

[J/kg]. For the case of soda-lime silica glass, this amount of energy is found in Table 3.5. In this Thesis, it was assumed that the glass thermal properties were the same for both the solid and liquid state.

There are several methods to model numerically a material phase-change. *COMSOL* uses an apparent specific heat capacity, $C_{p_{app}}(T)$, in the heat equation to account for the glass phase-change given by:

$$C_{p_{app}}(T) = C_p(T) + L_f \frac{d\theta}{dT} \quad (3.21)$$

where θ represents the fraction of liquid phase, modelled as a smooth ramp function in the temperature interval between $T_m - \Delta T/2$ and $T_m + \Delta T/2$, where ΔT is a user defined parameter that specifies the temperature difference between the beginning and the end of the phase change process which should be as small as possible. By definition θ is equal to zero for temperatures below $T_m - \Delta T/2$ and equal to the unity for temperatures greater than $T_m + \Delta T/2$. Equation (3.21) shows that outside of the temperature interval $T_m - \Delta T/2$ to $T_m + \Delta T/2$, the apparent specific heat capacity is equal to the glass one since in this interval $d\theta/dT = 0$. Inside that temperature range $d\theta/dT = 1/\Delta T$, which models an extra energy that would be necessary to rise the temperature by 1 K of 1 kg of glass, simulating therefore the energy consumption of the phase change process.

During this work, a value of 50 K was chosen for the parameter ΔT . This value is justified by the comparison between two converged solutions with $\Delta T = 50$ K and $\Delta T = 20$ K shown in Figure 3.12. These solutions were obtained for the model without the electromagnetic interface, using a power source assigned to the glass region to simulate the microwave energy absorption. Comparing the results, it is noticeable that the two solutions are practically the same, justifying the use of $\Delta T = 50$ K which requires less computational efforts.

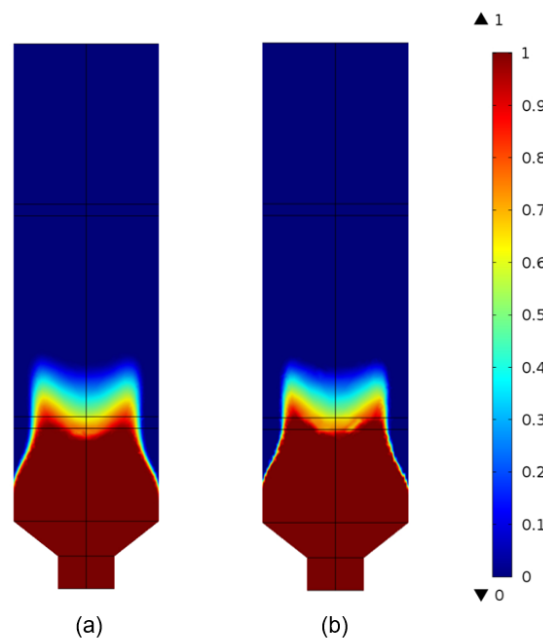


Figure 3.12: Phase transition converged solution with (a) $\Delta T = 50$ K and (b) $\Delta T = 20$ K.

3.5 Mass and energy balances

In order to verify if the numerical model is correctly built, it is important to perform mass and energy balances. As it will be seen in the next section energy balances are of extreme importance in this work because they are the key information that will allow the control of the glass melting process. Before introducing the calculations required for the mentioned balances, it is important to define the control volume. In this Thesis the control volume used to perform mass and energy balances is defined by the external boundaries of the microwave cavity including the tube inlet and outlet.

Mass balances must ensure that all the mass entering the control volume is equal to the mass leaving it, *i.e.*, the glass mass flow rate at the tube inlet, S_{in} , must be the same as the one at the outlet, S_{out} :

$$\dot{m}_{in} = \rho_{ave} \iint_{S_{in}} (\vec{U} \cdot \vec{n}) dA = \rho_{ave} \iint_{S_{out}} (\vec{U} \cdot \vec{n}) dA = \dot{m}_{out} \quad (3.22)$$

To perform the energy balance, some concepts must firstly be introduced to the reader. When the microwave radiation power enters the cavity, P_{in} [W], some of it will be reflected, P_{ref} [W],. The fraction of the input power that is reflected is given by:

$$\frac{P_{ref}}{P_{in}} = |S_{11}|^2 \quad (3.23)$$

where S_{11} is the reflection coefficient. Since the model can compute the radiation leakage, P_L [W], that may occur across the tube inlet and outlet, a fraction of the non-reflected power can be also lost. Therefore, the fraction of the power input that is absorbed by the glass and tube, P_{abs} [W], *i.e.*, the microwave efficiency, η_{MW} , is given by:

$$\frac{P_{abs}}{P_{in}} = \eta_{MW} = 1 - |S_{11}|^2 - \frac{P_L}{P_{in}} \quad (3.24)$$

In order to get the value of the microwave efficiency, η_{MW} , *COMSOL* allows the user to get the value of the reflection coefficient, S_{11} , as a probe. To calculate microwave leakage, P_L , it is necessary to create a probe that gives the surface integral of the Poynting vector, $\vec{S} = \vec{E} \times \vec{H}$, along the leakage surfaces S_{in} and S_{out} . As it was seen in Section 2.3, the Poynting vector represents an electromagnetic energy flux with units of W/m². Therefore, the microwave power leakage, P_L , is given by the following expression:

$$P_L = \iint_{S_{in}} [(\vec{E} \times \vec{H}) \cdot \vec{n}] dA + \iint_{S_{out}} [(\vec{E} \times \vec{H}) \cdot \vec{n}] dA \quad (3.25)$$

Another important concept is the thermal efficiency, η_T , which is the fraction of the absorbed power, P_{abs} , that actually contributes to the heating of the glass, P_h [W], since some of it will be lost by radiation and convection across the external surfaces of the microwave cavity. This efficiency is computed by:

$$\eta_T = \frac{P_h}{P_{abs}} \quad (3.26)$$

where P_h is the sum of the sensible heat, SH [W], responsible for the glass temperature rise from T_0 to T , which is the local temperature at the tube outlet, and the latent heat, LH [W], responsible for the glass phase change:

$$P_h = \iint_{S_{out}} \left[\rho(\vec{U} \cdot \vec{n}) \int_{T_0}^T C_p(T) dT \right] dA + \iint_{S_{out}} [\rho(\vec{U} \cdot \vec{n}) L_f \theta] dA \quad (3.27)$$

where the first and second terms on the right-hand side of Equation (3.27) refer to the sensible and latent heat, respectively, which represent the required power to process the glass in the adiabatic case.

The global efficiency of the process, η_G , represents the fraction of the total power input that contributes to the melting of the glass, and is given by:

$$\eta_G = \frac{P_h}{P_{in}} \theta = \eta_{MW} \eta_T \theta \quad (3.28)$$

where the variable θ is used to penalize the efficiency when the glass is not totally processed when leaving the system.

An energy balance to the microwave cavity guarantees that, at steady-state, the power input, P_{in} , times the microwave efficiency, η_{MW} , is equal to the sensible heat, SH , plus the latent heat, LH , and the thermal losses, P_{loss} :

$$P_{in} \eta_{MW} = \iint_{S_{out}} \left[\rho(\vec{U} \cdot \vec{n}) \int_{T_0}^T C_p(T) dT \right] dA + \iint_{S_{out}} [\rho(\vec{U} \cdot \vec{n}) L_f \theta] dA + P_{loss} \quad (3.29)$$

To perform this energy balance, it is required to extract some variables from the simulation, namely the value of the microwave efficiency, η_{MW} , the sensible heat, SH , the latent heat, LH , and the thermal losses, P_{loss} .

3.6 *Matlab* microwave heating controller code

The main goal of this Thesis is to simulate the glass melting process in order to study the influence of several operational conditions on its global efficiency, η_G . To achieve this objective, at steady-

state, the glass must be totally in a melted state at the tube outlet, so it is necessary to provide enough microwave power, P_{in} , to rise the glass temperature from T_0 to a temperature, T , which must be greater than the glass melting temperature, T_m . Since $T_m = 1450$ K, it was decided that an outlet average temperature of $T_{out} = 1600$ K should be obtained at steady-state. Besides the required sensible heat, SH_{needed} [W], the latent heat must be considered, *i.e.*, the additional power for the phase-change. The latent heat is defined by the material's mass flow rate times its latent heat of fusion, $LH_{needed} = \dot{m}L_f$ [W]. Since the microwave cavity is not completely insulated, thermal losses, P_{loss} , will arise as the system temperature increases. To achieve the desired outlet average temperature, the power input, P_{in} , must account for those thermal losses. To achieve the desired outlet conditions, another essential parameter that must be considered in the calculation of the power input is the microwave efficiency, η_{MW} . Regarding Equation (3.29), the required microwave power input is given by:

$$P_{in} = \frac{\iint_{S_{out}} \left[\rho(\vec{U} \cdot \vec{n}) \int_{T_0}^{T_{out}} C_p(T) dT \right] dA + \dot{m}L_f + P_{loss}}{\eta_{MW}} \quad (3.30)$$

Since the velocity field at the outlet is not known *a priori*, a simplification assuming a uniform velocity profile must be done to Equation (3.30) to get the required power input:

$$P_{in} = \frac{\dot{m} \int_{T_0}^{T_{out}} C_p(T) dT + \dot{m}L_f + P_{loss}}{\eta_{MW}} \quad (3.31)$$

Steady-state simulations could be performed to get converged solutions for different operational conditions. However, it is impossible to know *a priori* both microwave efficiency, η_{MW} , and thermal losses, P_{loss} . To get a converged solution with the desired outlet conditions using the required power input it is necessary to run transient simulations during a defined physical time, Δt_s . After each simulation, both microwave efficiency and thermal losses must be extracted from the results in order to update the power input. This process must be repeated until the transient term of the heat equation is below a user defined limit, meaning that steady-state was achieved. Being this a very time-consuming method that requires constant supervision, a *MATLAB* code was developed to automatically control the glass melting process.

COMSOL multiphysics software provides a bidirectional interface with *MATLAB* which enables the user to write its own codes to run simulations, analyze and manipulate its results in the *MATLAB* interface, rather than in the *COMSOL* graphical user interface. This bidirectional interface is of extreme importance since it allows the user to automatically run the transient simulations sequence described above. In this section, a general description of the developed *MATLAB* code is presented. This algorithm is composed by four main parts.

In the first part, the user introduces several inputs of the *COMSOL* model, namely the glass mass flow rate, \dot{m} [kg/s], the tube inner diameter, d_i [m], the temperature at which the glass enters the tube, T_0 [K], and the desired outlet average temperature, T_{out} [K]. Regarding Figure 3.8, a fourth-order polynomial function was found to fit the specific heat capacity temperature dependence curve, $C_p(T)$,

and was introduced in the code as a variable along with the glass latent heat of fusion L_f . With these inputs, the required sensible and latent heat can be calculated as shown in Equation (3.31).

To compute the microwave efficiency at the initial conditions described in Section 3.3, a plunger position parametric study must be run. This simulation uses only the electromagnetic interface and calculates the electromagnetic field in the microwave cavity for a range of the plunger positions while imposing the initial temperature field. As described in Section 3.1, using Equation (2.39), the waveguide wavelength is found to be $\lambda_g = 174$ mm. In absolute values, the electric field repeats itself every half wavelength, so it is expected that the value of $1 - |S_{11}|^2$, and consequently the microwave efficiency, also repeats itself every half wavelength. To run the initial plunger position parametric study, the electromagnetic field, thus the value of $1 - |S_{11}|^2$, is calculated for plunger positions between $0 \leq \Delta d_p \leq 87$ mm, where Δd_p is the distance between the plunger's actual and minimum positions. When the plunger is at its minimum position its distance from the center of the tube is 50 mm. Figure 3.13 shows the results of the plunger position parametric study for the initial conditions of a model with $d_i = 30$ mm. The curve plotted presents the value of $1 - |S_{11}|^2$ as a function of the plunger position and shows that a maximum value of 0.837 is achieved when the moving plunger is 54 mm away from its minimum location. It is also important to notice that the value of $1 - |S_{11}|^2$ repeats itself every half wavelength.

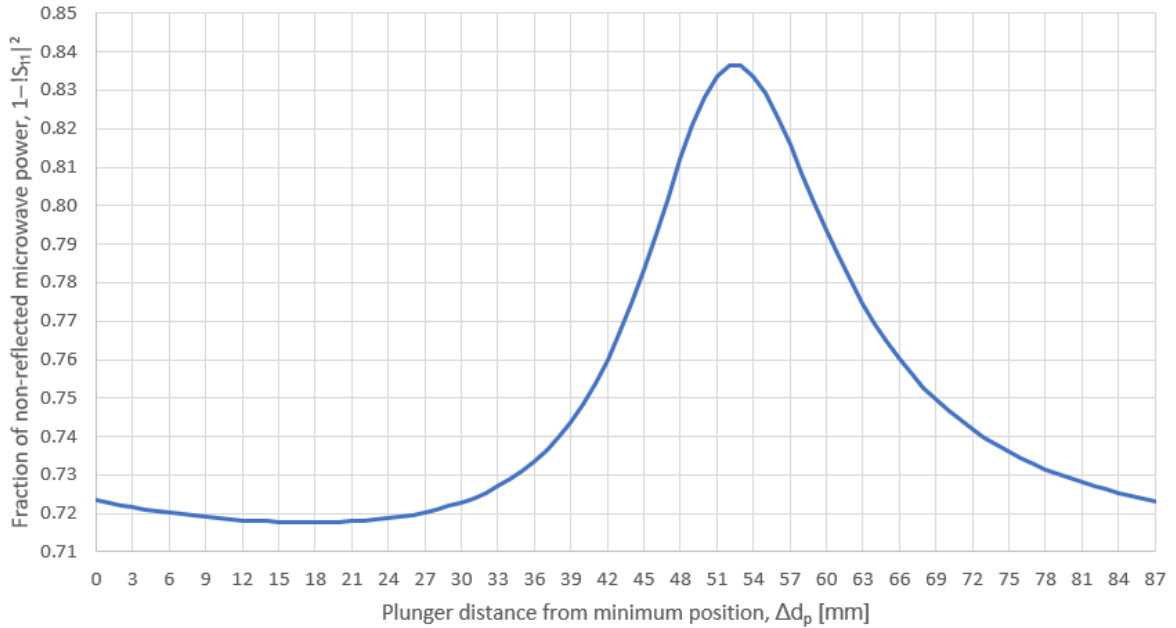


Figure 3.13: Plunger parametric study for the initial thermal conditions in a model with $d_i = 30$ mm. The curve shows the value of $1 - |S_{11}|^2$ for different plunger positions.

With the information given by the plunger position parametric study for the initial temperature distribution, and with the computed microwave leakage, P_L , the user can give to the *MATLAB* code the initial maximum microwave efficiency, η_{MW} , and the respective plunger position that maximizes it. The power input, P_{in} , for the first transient simulation, or iteration, is then calculated using Equation (3.31). Since the thermal losses are unknown before the end of the first iteration, they are not considered at this stage. The last input variable that the user must give to the algorithm is the physical time of each

iteration, Δt_s , during which the transient simulations should run. In this Thesis it was considered that Δt_s should be equal to a quarter of the glass residence time in the tube.

In the second part, the *MATLAB* code loads the *COMSOL* model with the defined initial parameters. After that, the code starts the simulation and at the end of it, the values of the control probes are extracted, analyzed and stored. These control probes are: the glass average outlet temperature, the transient term of the heat equation, the outlet fraction of melted glass, the radiation and convection thermal losses, the sensible and latent heat according to Equation (3.29), the fraction of non-reflected microwave power, $1 - |S_{11}|^2$, the microwave leakage, the power absorbed by the glass and by the tube as well as their maximum temperatures. Then, the *COMSOL* model is saved and identified by the respective iteration number.

In the third part, the *MATLAB* code starts a parametric study of the plunger position. Using the thermal field obtained in the previous transient simulation, the electromagnetic field and the value of $1 - |S_{11}|^2$ are calculated for the current plunger position and for other two, 1 mm away for the left and right side. Then, the algorithm analyzes those values and check where maximum efficiency occurs. If the value of $1 - |S_{11}|^2$ is maximum in the central position, the code stores this value as well as the corresponding plunger position. If the left or right position is the one that corresponds to a higher value of $1 - |S_{11}|^2$, it is considered as a central position for a new parametric study. This cycle continues until this quantity is maximum at the central position. By running this cycle at the end of each iteration, the *MATLAB* code will keep the microwave efficiency as high as possible during the heating process.

By defining the plunger position for the next iteration and the corresponding value of $1 - |S_{11}|^2$, the algorithm calculates the current value of the microwave efficiency, η_{MW} , using Equation (3.24). After that, the power input, P_{in} , for the following iteration is calculated by adding the thermal losses obtained to the sensible and latent heat required and dividing it by the new microwave efficiency value.

In the fourth and last part, the *MATLAB* code will check if convergence has been achieved by comparing the value of the transient term of the heat equation to a user defined limit. In this work, convergence was considered when this value was less than 0.1% of the power absorbed by the glass. If the convergence criterion is achieved, the converged model is saved, and the iterative process ends. If not, a new transient simulation, or iteration, is started with the updated power input. At the end of each iteration, the controller code presents some probe values to the user in order to facilitate the monitoring process.

When the iterative process ends, all probe values stored at the end of each iteration allow the analysis of the heating process evolution. As stated before, the *MATLAB* code automatically controls the heating process, by updating the power input at every iteration and by keeping the microwave efficiency as high as possible through the adjustment of the plunger position. Summing up and to better understand the *MATLAB* controller code, an algorithm is presented next with a step by step description. A flowchart is also presented in Figure 3.14, summarizing this algorithm.

The *MATLAB* controller code consists of the following steps:

1. Set the input parameters for the *MATLAB* code, namely: the material mass flow rate, the tube's inner diameter, the desired glass outlet average temperature, $T_{out} = 1600$ K in this

- Thesis, the glass inlet temperature, the physical duration of the transient simulations, the initial plunger position and the initial microwave efficiency.
2. With the data given in 1, compute the initial power input using Equation (3.31) assuming no thermal losses since they are not known *a priori*.
 3. Load the *COMSOL* model.
 4. Assign the data given in 1 and the power input computed in 2 to the *COMSOL* model.
 5. **Start 1st loop**: Getting a steady-state solution.
 - 5.1. Run a transient simulation with a total time of Δt_s .
 - 5.2. Extract all the relevant data, namely the thermal losses, the microwave leakage, the value of the transient term of the heat equation and the power absorbed by the glass.
 - 5.3. **Start 2nd loop**: Plunger position update.
 - 5.3.1. Run a parametric study for the actual and adjacent plunger positions.
 - 5.3.2. If the maximum value of $1 - |S_{11}|^2$ is found on the actual position, with the microwave leakage obtained in 5.2 compute the new microwave efficiency. Leave 2nd loop and go to point 5.4.
 - 5.3.3. If not, the position with the highest value for $1 - |S_{11}|^2$ is defined as the actual one and start 2nd loop again from point 5.3.1.
 - 5.4. Compute the new power input with the data extracted in 5.2 and computed in 5.3.2 using Equation (3.31).
 - 5.5. If the value of the transient term of the heat equation is less than 0.1% of the power absorbed by the glass, steady-state solution has been achieved. Save the converged model. Leave 1st loop and go to point 6.
 6. End of the *MATLAB* controller code.

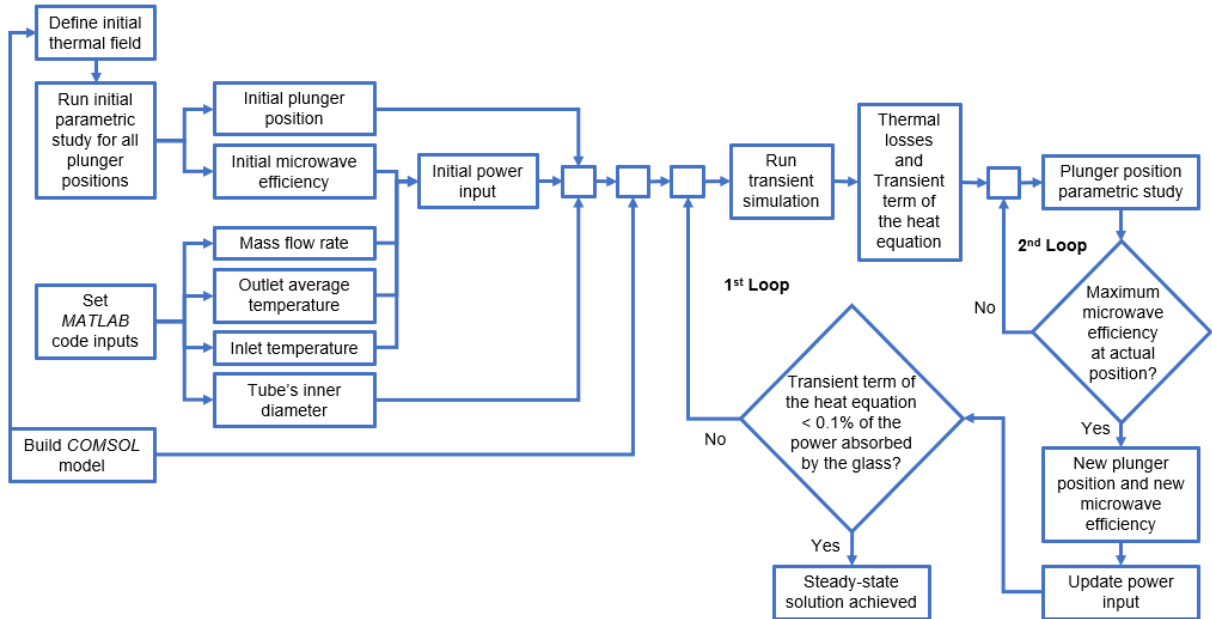


Figure 3.14: Flowchart describing the *MATLAB* controller code.

Chapter 4

Results and discussion

This chapter aims to present and discuss the numerical results obtained during this work. In Section 4.1, the performed mesh convergence analysis is presented, to justify the chosen grid of the numerical simulations. Section 4.2 presents the results of a scalability study done in order to check the parallel computing performance. The influence of imposing rotation on the applicator tube during the heating process is discussed in Section 4.3. The history of the transient glass heating process as well as its converged solution for defined operation conditions is shown and discussed in Section 4.4. Section 4.5 looks for the impact that the plunger position update, the microwave leakage and the usage of a *slip* boundary condition, exert on the glass melting process. Finally, in Section 4.6, a tube inner diameter and flow mean velocity parametric studies are presented in detail to show how these parameters influence the glass melting process and to find the best possible operational conditions.

4.1 Mesh convergence analysis

A mesh convergence analysis is an indispensable procedure for all numerical studies. In any numerical model, the discretized solution reaches the exact solution of the mathematical model when the discretization parameters tend to zero, *i.e.*, when the size of the elements that compose the simulation domain approach zero. There is, however, a compromise between the accuracy of the discretized solution and the available computational resources to run the numerical simulations. A good mesh allows to have results with a good accuracy with the minimum possible simulation time. This can be achieved and studied with a good convergence analysis.

Following the works of Oberkampf and co-authors [55-56], Eça and Hoekstra [57] and Roache [58], to run a mesh convergence analysis it is necessary to have numerical results for at least four different meshes. For this analysis, five simulations were done for a model with a glass mass flow rate of $\dot{m} = 3.6$ kg/h with an applicator tube with inner diameter of $d_i = 30$ mm for five different meshes, which were numbered from the most refined, mesh 1, to the coarser one, mesh 5. The defined outlet average temperature was $T_{out} = 1600$ K. These meshes were created in order to have a constant refinement ratio of $r = 1.26$, which, for a 3D analysis, corresponds to double the number of mesh

elements. Table 4.1 presents Information about the number of elements of each created mesh and the respective normalized grid spacing, NGS, defined as the ratio h_i/h_1 , where h_i is the mesh spacing of grid i , or the average characteristic length of the elements from grid i .

Table 4.1: Number of elements, NoE, and normalized grid spacing, NGS, of the created grids for the mesh convergence analysis.

	NoE	NGS
Mesh 1	597746	1.00
Mesh 2	298873	1.26
Mesh 3	149957	1.59
Mesh 4	74837	2.00
Mesh 5	37610	2.51

Before presenting the converged results, *i.e.*, the results obtained at steady-state, for the simulations in each of the five meshes, it is relevant to introduce some important concepts that are strongly related to the convergence analysis. The first concept to be introduced is the order of accuracy, p , that is the rate at which a discrete solution approaches the exact solution to the mathematical model in the limit as the discretization error approaches zero [56]. The observed order of accuracy can be calculated by:

$$p = \frac{\ln \left(\frac{f_3 - f_2}{f_2 - f_1} \right)}{\ln(r)} \quad (4.1)$$

where f_i is the converged result of a control variable for mesh i and r is the refinement ratio that is assumed constant and equal to:

$$r = \frac{h_3}{h_2} = \frac{h_2}{h_1} = 1.26 \quad (4.2)$$

Equation (4.1) is valid when the solutions f_i are in the asymptotic range, which is defined as the range of discretization sizes, h , where the lowest-order terms in the discretization error expansions dominate. Knowing the formal rate of convergence of the discretization method with mesh refinement and if discrete solutions on two systematically refined meshes are available, it is possible to use that information to obtain an estimate of the exact solution to the mathematical model. This estimate is known in the literature as the Richardson extrapolation, \bar{f} , [56], which is the value to which the numerical solution would converge if the contribution of the discretization error could be neglected. It can be calculated by Equation (4.3) presented below:

$$\bar{f} = f_1 + \frac{f_1 - f_2}{r^p - 1} \quad (4.3)$$

Since in the majority of practical problems it is very difficult to have all meshes in the asymptotic range and to have data free of scatter, in the work of Eça and Hoekstra [57], it is proposed a method for estimating the discretization error based on using a power series expansion as a function of the typical cell size that is fitted to the data in the least-squares sense. Having data for n_g meshes, assuming that the higher-order terms can be neglected, the discretization error can be estimated as:

$$e(\phi_i) = f_i - \bar{f} = \alpha h_i^p \quad (4.4)$$

where α is a constant. To find the value of \bar{f} in order to estimate the error it is required to find the minimum of the function:

$$S_{RE}(\bar{f}, \alpha, p) = \sqrt{\sum_{i=1}^{n_g} (f_i - (\bar{f} + \alpha h_i^p))^2} \quad (4.5)$$

The glass average temperature, T_{ave} [K], the glass maximum temperature, T_{max} [K], the microwave efficiency, η_{MW} , and the thermal efficiency, η_T were the chosen control variables to be analyzed in order to check convergence. The control variables obtained for the five different meshes, along with the values obtained for the estimate of the exact solution, \bar{f} , are all presented in Table 4.2. The control variables and respective estimates for the exact solutions are plotted in Figure 4.1.

Table 4.2: Results of the mesh convergence analysis by using the converged control variables for five different meshes.

	T_{ave} [K]	T_{max} [K]	η_{MW}	η_{MW}
Mesh 1	1186.93	1830.96	0.36406	0.60509
Mesh 2	1187.27	1829.21	0.36412	0.60528
Mesh 3	1187.74	1826.47	0.36437	0.60552
Mesh 4	1188.65	1822.80	0.36544	0.60732
Mesh 5	1190.82	1825.34	0.36652	0.60732
\bar{f}	1186.45	1834.75	0.36394	0.60491

Regarding Table 4.2 and Figure 4.1, it can be concluded that all the converged solutions of the control variables are converging to the estimate of the exact solution. The estimated “exact” solutions for the average temperature, maximum temperature, microwave and thermal efficiencies are plotted in Figure 4.1 as well as the least-squares fits obtained from the four most refined meshes, *i.e.*, mesh 1 to mesh 4. Since the deviation between the converged solutions for mesh 4 and the estimated “exact” solutions were 0.19% for the average temperature, 0.65% for the maximum temperature, 0.41% for the

microwave efficiency and 0.40% for the thermal efficiency, that mesh was chosen for the remain simulations in this Thesis.

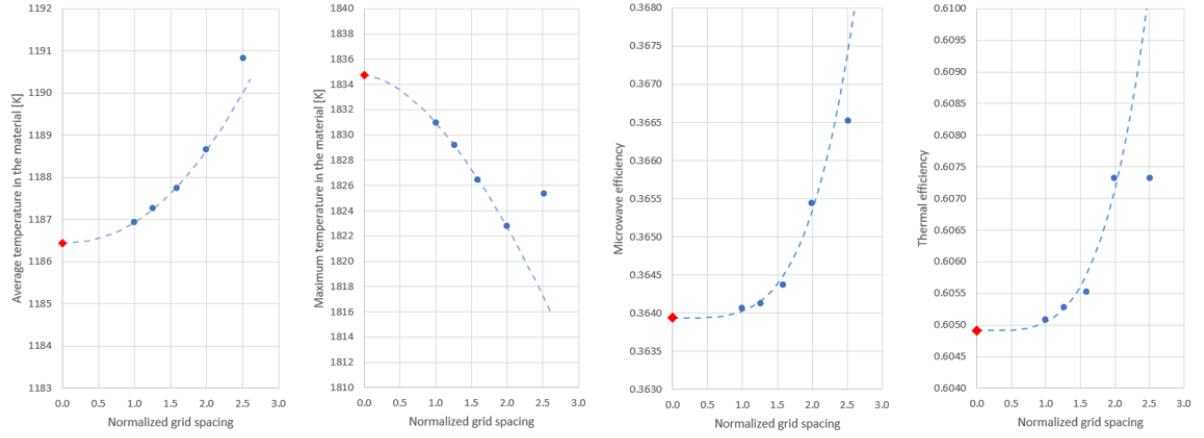


Figure 4.1: Convergence of the control variables for the five meshes along with the respective fit and result for the exact solution estimation, in red.

The simulation times obtained with mesh 3 and 4, for one transient iteration with a physical time of $\Delta t_s = 44$ s, along with the relative errors regarding the average outlet temperature variable are presented in Table 4.3. These simulations were run on a machine with an AMD Ryzen 7200X CPU with 8 cores and a clock speed of 3.7 GHz.

Table 4.3: Simulation times and average temperature relative errors obtained with mesh 3 and 4 for one transient iteration with a physical time of $\Delta t_s = 44$ s in a machine with an AMD Ryzen 7200X CPU 8 cores and a clock speed of 3.7 GHz. All 8 cores were used in parallel computing.

	Simulation time [min]	Time ratio	Error [%]
Mesh 3	226.68	1.00	0.11
Mesh 4	104.35	0.46	0.19

Regarding Table 4.3, it can be concluded that mesh 2 spends less than half of the time spent by mesh 1 with a loss of accuracy of only 0.08%. Mesh 4 was the selected mesh because it consumes significantly less computational resources with a very good accuracy.

4.2 Scalability study

Parallel computing usually allows for a reduction in numerical problems execution costs due to the possibility to distribute the workload between different processors. The performance of parallel computing applications can be quantified by the speedup, $S(n_p)$, which is given by:

$$S(n_p) = \frac{t(1)}{t(n_p)} \quad (4.6)$$

where n_p is the number of processors, $t(1)$ and $t(n_p)$ are the computational times required to solve a numerical problem with 1 and n_p processors, respectively. Finally, the efficiency, $E(n_p)$, is given by:

$$E(n_p) = \frac{S(n_p)}{n_p} \quad (4.7)$$

The speedup ideal scenario is such that $S(n_p) \approx n_p$, and, consequently, $E(n_p) \approx 1$, which is known as a linear speedup. However, usually a sub-linear scenario takes place, meaning that $S(n_p) < n_p$ and $E(n_p) < 1$. When the speedup is sub-linear the efficiency decreases when n_p increases. This efficiency decrease is due to the overhead time related to the synchronization, communication and other redundant operations between processors. Super-linear speedup happens when $S(n_p) > n_p$ and, consequently, $E(n_p) > 1$. This phenomenon may arise due to higher cache hit ratios and/or lower memory usage compared to the single core algorithm [59].

This section presents the results of the scalability study done to check the parallel computing performance. The simulations were carried out in an AMD Ryzen 7200X CPU with 8 cores and a clock speed of 3.7 GHz. A transient simulation with a physical duration time of $\Delta t_s = 44$ s was run using 1, 2, 4 and 8 cores. The simulation times, speedup and efficiency are presented in Table 4.4.

Table 4.4: Scalability study results obtained with an AMD Ryzen 7200X CPU with 8 cores and a clock speed of 3.7 GHz.

Processors, n_p	$t(n_p)$ [s]	$S(n_p)$	$E(n_p)$ [%]
1	465.18	1.00	100
2	189.10	2.46	123
4	151.23	3.08	77
8	104.35	4.46	56

Regarding the results presented in Table 4.4, it is noticeable that the speedup is always increasing and a super-linear speedup regime occurs when the number of processors increases from $n_p = 1$ to $n_p = 2$. As already said, this phenomenon may arise due to better memory performance [59]. When the value of n_p continues to increase, a sub-linear speedup regime is observed, and the efficiency of the parallel computing starts to decrease, mainly because as n_p increases so does the time spent by synchronization and communication between processors. It is observed that when 8 cores are used, a 44% efficiency loss is observed in the parallelization.

These results show that when a single simulation is needed, all 8 cores should be used in parallel computing. However, when multiple simulations are required, running 4 parametric simulations simultaneously, each with 2 cores should be a faster approach.

4.3 Influence of the tube's rotation on the glass heating process

To evaluate the influence of the tube's rotation on the glass heating process and check whether the rotation should be imposed and its right magnitude to get the best results, a sequence of simulations was done for different rotation velocities and other fixed operation conditions like a mass flow rate of $\dot{m} = 3.6$ kg/h, an applicator tube inner diameter of $d_i = 30$ mm and an outlet average temperature of $T_{out} = 1600$ K. It may be useful to recall the description of the microwave cavity geometry presented in Section 3.1. To define the rotation magnitude imposed in each simulation, a reference value, ω_{ref} [rad/s], was established as:

$$\omega_{ref} = U_{ave}/r_i \quad (4.8)$$

where r_i is the tube inner radius [m] and U_{ave} is the average velocity across the tube's cross section [m/s] given by:

$$U_{ave} = \dot{m}/\rho\pi r_i^2 \quad (4.9)$$

Equation (4.8) establishes that when the rotation is equal to ω_{ref} , the tangential velocity in the tube's wall is the same as the average axial velocity, U_{ave} . Each simulation tested a different value for the tube rotation, ω_r [rad/s], given by:

$$\omega_r = 2^n \omega_{ref} \quad (4.10)$$

with $n = 1, 2, 3, 4, \dots$, and being 2^n the number of times that the actual tangential velocity is greater than the average axial velocity, U_{ave} .

Observing Figure 4.2, it is evident that imposing rotation to the applicator tube has a significant influence in the achieved steady-state solution. Firstly, as the rotation velocity increases, the thermal field tends to be axisymmetric. Secondly, temperature homogeneity at the outlet zone increases at higher rotation velocities which improves glass quality and reduces thermal stresses [8]. Finally, it can be noticed that the glass maximum temperature decreases with increasing rotation, as depicted in Figure 4.3. Lower temperatures in the glass improve the thermal efficiency since the thermal losses decrease. Another advantage of lowering the glass maximum temperature is related to the decrease in the tube's maximum temperature, since it was verified that the boron nitride starts to deteriorate at tem-

peratures above 1900 K [36]. The tube's maximum temperature at steady-state is also showed, for several rotation velocities, in Figure 4.3.

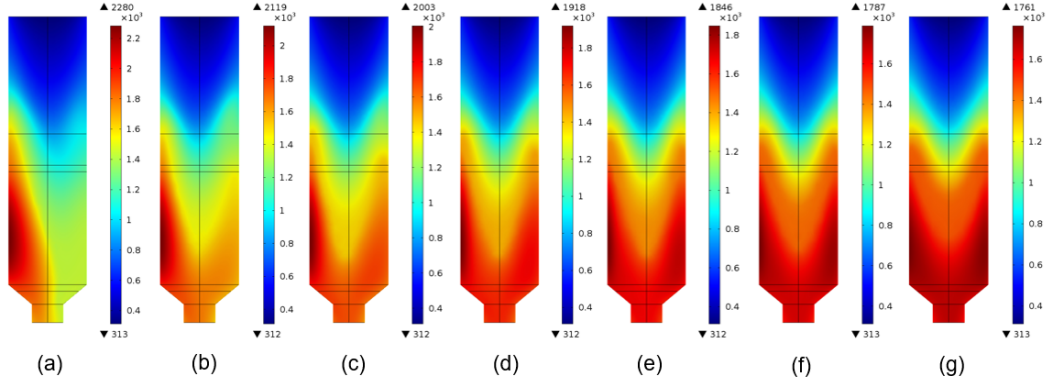


Figure 4.2: Steady-state thermal field [K], for different rotation velocities, ω_r [rad/s]: (a) no rotation, (b) $\omega_r = 2\omega_{ref}$, (c) $\omega_r = 4\omega_{ref}$, (d) $\omega_r = 8\omega_{ref}$, (e) $\omega_r = 16\omega_{ref}$, (f) $\omega_r = 32\omega_{ref}$ and (g) $\omega_r = 64\omega_{ref}$.

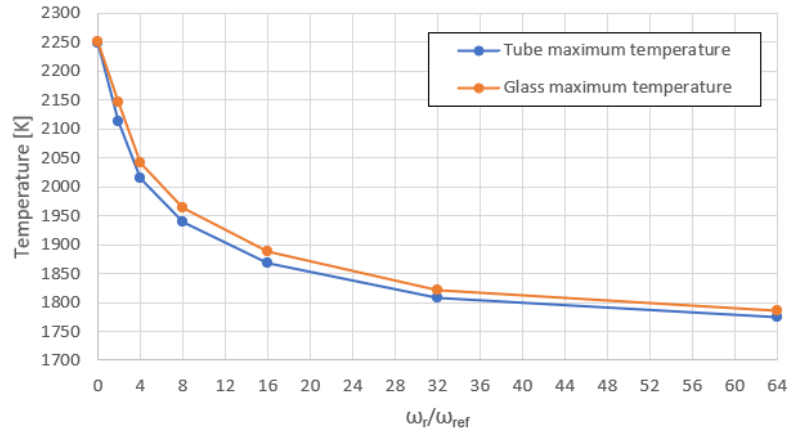


Figure 4.3: Glass and tube maximum temperatures at steady-state for different rotation velocities.

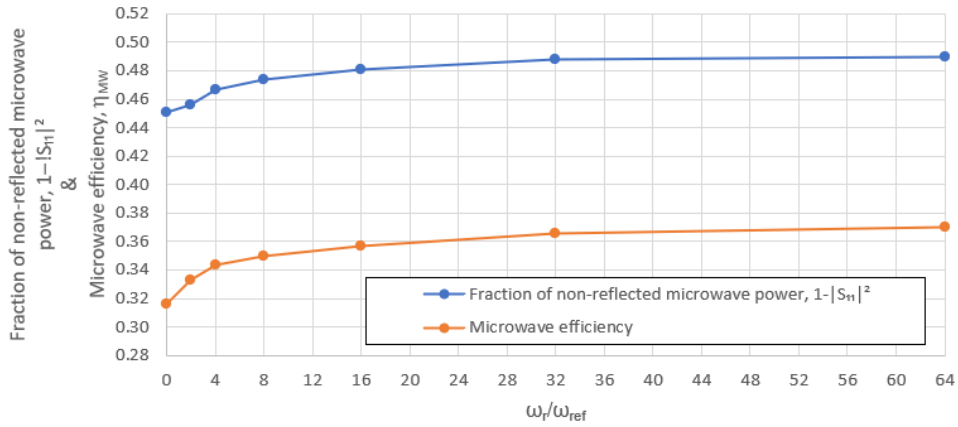


Figure 4.4: Fraction of non-reflected microwave power, $1 - |S_{11}|^2$, and microwave efficiency, η_{MW} , dependence on the rotation velocity.

Figure 4.4 presents the evolution of the fraction of non-reflected microwave power, $1 - |S_{11}|^2$, as well as of the microwave efficiency, η_{MW} , as the rotation increases. It is observed that there is a vertical shift between the two curves, which means, recalling Equation (3.24), that the ratio between the power leakage, P_L , and the power input, P_{in} , is almost independent of the rotation. It is also shown that, as the rotation velocity increases, there is an improvement in the value of $1 - |S_{11}|^2$, and consequently in the microwave efficiency, η_{MW} . The curves show an asymptotic behavior, indicating that there is no significant advantage in imposing a rotation velocity greater than $\omega_r = 32\omega_{ref}$ rad/s.

The increase in the value of η_{MW} with rotation might be explained by the thermal field uniformity commented above. As it was observed, the maximum temperature in the glass diminishes as the rotation velocity increases and, regarding Figure 3.6 as well as Equation (2.35), for lower temperatures, the dielectric properties of the glass decrease which contributes to an increase in the penetration depth, δ . Figure 4.5 shows the penetration depth, δ , at the surface where the microwaves penetrate the glass for the cases without rotation and with rotation velocity of $\omega_r = 32\omega_{ref}$ rad/s. The color legend presents values between 0.58 and 1.3 mm. For the case without rotation, the penetration depth is smaller than for the case with rotation, which means that the heat source, Q , given by Equation (2.29), is concentrated in a thinner outer layer, since the electric field is more rapidly attenuated when penetrating the glass, as shown in Figure 4.6.

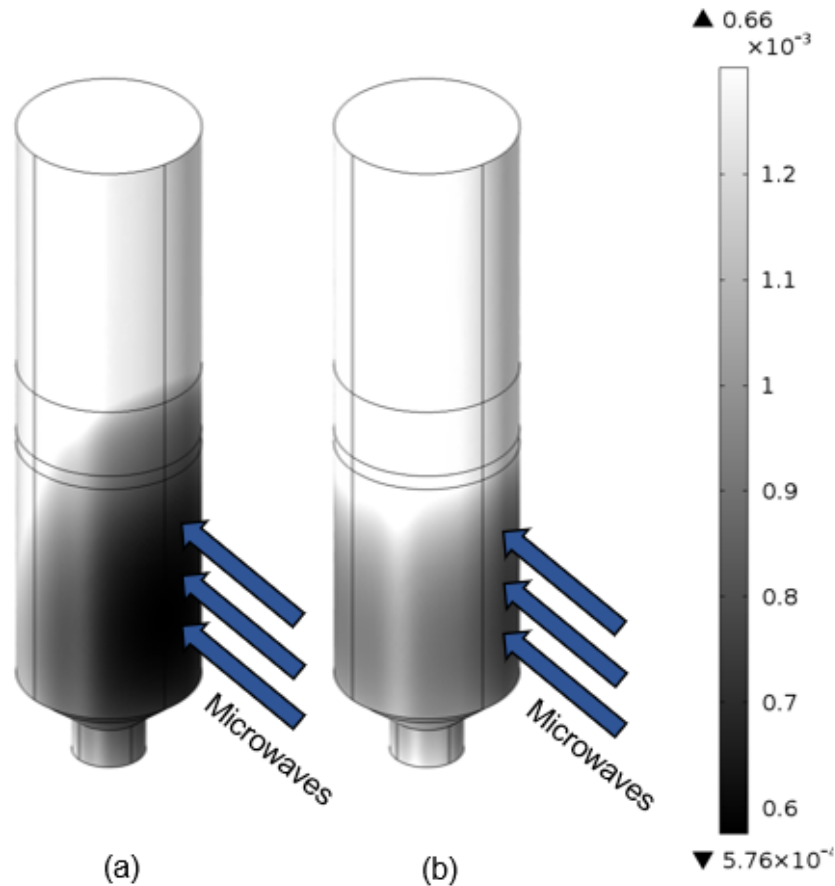


Figure 4.5: Penetration depth, δ [m], at the surface where the microwaves penetrate the glass for the cases (a) without rotation and (b) with rotation velocity of $\omega_r = 32\omega_{ref}$ rad/s.

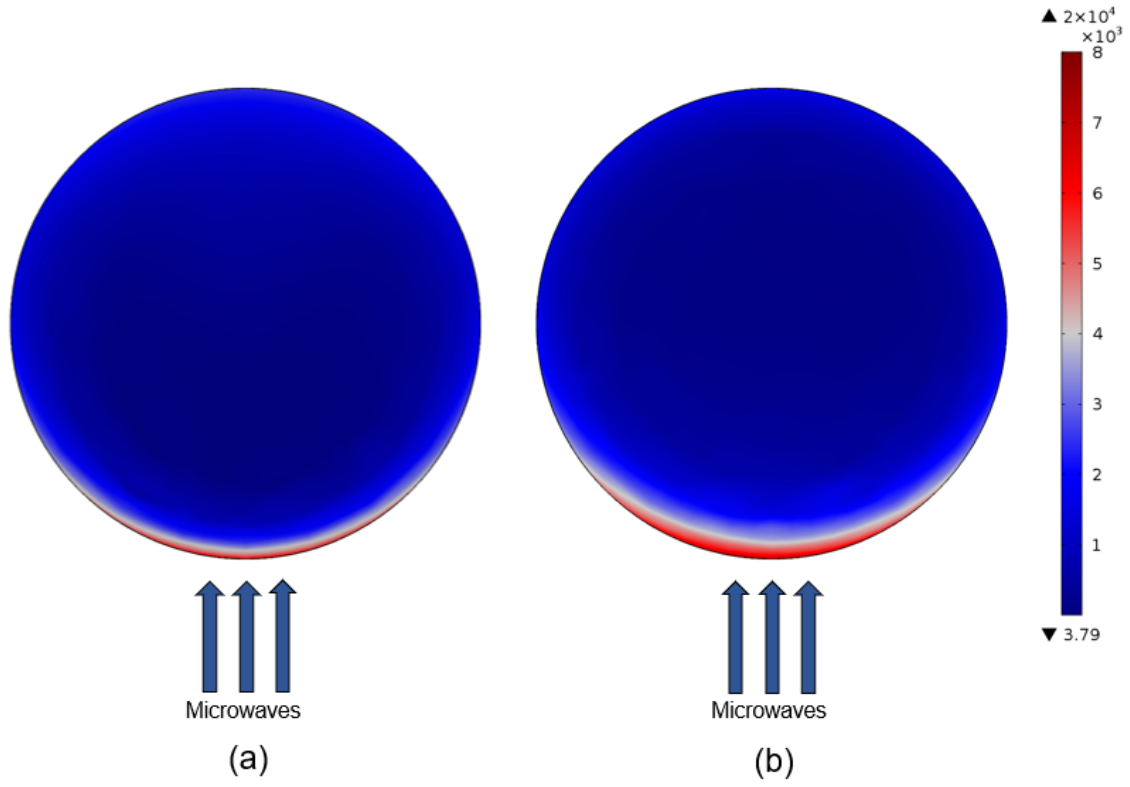


Figure 4.6: Electric field norm [V/m] inside the glass for the cases (a) without rotation and (b) with rotation velocity of $\omega_r = 32\omega_{ref}$ rad/s, at a cross-section taken at the middle position inside the microwave cavity.

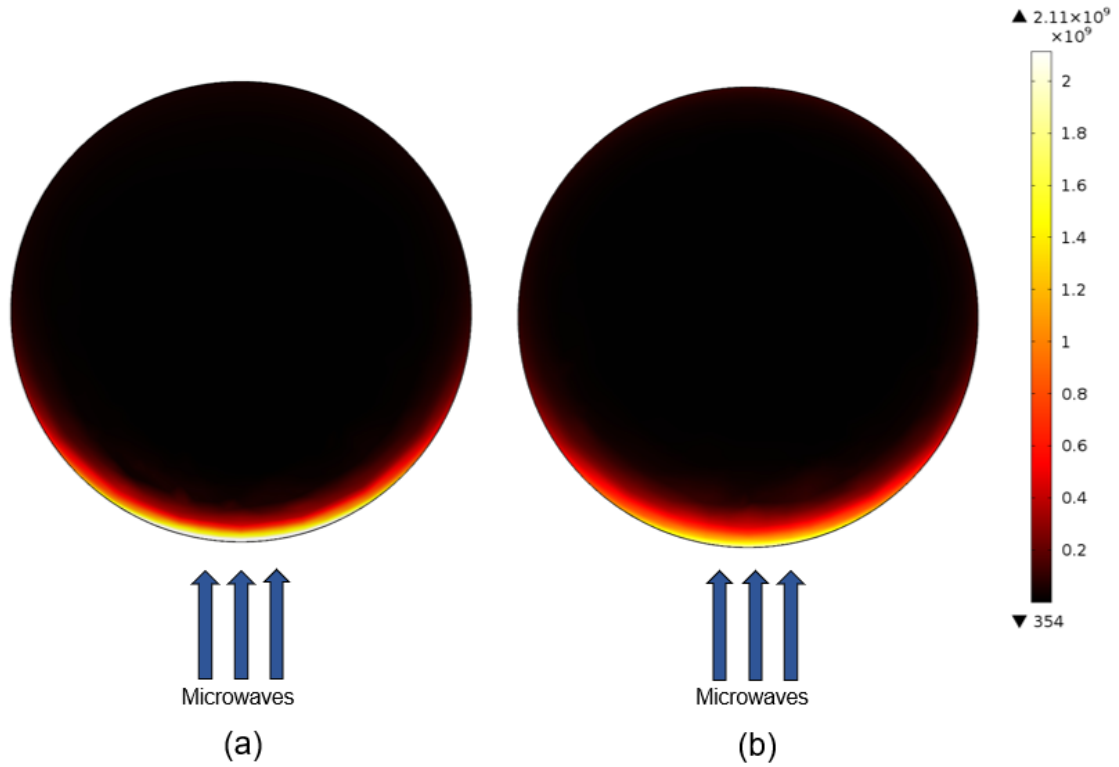


Figure 4.7: Heat source [W/m³] inside the glass for the cases (a) without rotation and (b) with rotation velocity of $\omega_r = 32\omega_{ref}$ rad/s, at a cross-section taken at the middle position inside the microwave cavity.

The heat source distribution at a cross-section located inside the microwave cavity equally distanced from its top and bottom surfaces is shown in Figure 4.7. Although the heat source peak is higher in the case without rotation, when it is integrated over the glass volume, the resulted power absorbed is higher in the case with rotation, since the volume that effectively absorbs the microwave radiation is slightly higher. A higher value for the penetration depth for the case with rotation allows a better microwave efficiency despite the lower loss factor, ϵ_r'' .

From the analysis done using Figures 4.3 and 4.4, it was decided to impose a rotation velocity of $\omega_r = 32\omega_{ref}$ rad/s for all the studies in this Thesis, since the improvements in the thermal field and in the microwave efficiency obtained for higher rotation velocities might not compensate the energy cost associated to the rotation increase.

4.4 Thermal history and converged solution

This section aims to present the evolution of the heating process controlled by the *MATLAB* code until steady-state is achieved for the operational conditions showed in Table 4.5. Its main purpose is to show that the algorithm can in fact obtain a steady solution with the desired conditions at the outlet and to show how some important variables evolve along the process. An energy balance is also carried out to check if the heating process is well modelled and to give some insight on how the microwave energy is being used.

Table 4.5: Operational conditions used for showing the control of the glass heating process done by the *MATLAB* algorithm.

Operational conditions	
Mass flow rate, \dot{m} [kg/h]	3.6
Tube inner diameter, d_i [m]	30
Rotation velocity, $\omega_r = 32\omega_{ref}$ [rpm]	13.1
Glass inlet temperature, T_{in} [K]	293
Desired glass average outlet temperature, T_{out} [K]	1600
Physical duration of the transient simulations, [s]	44

In the following figures, some relevant variables are plotted versus the physical time. In Figure 4.8, the fraction of non-reflected microwave power, $1 - |S_{11}|^2$, the microwave efficiency, η_{MW} , as well as the plunger position are shown. Regarding the curve of $1 - |S_{11}|^2$, it is observed that in the first couple of iterations the plunger adjustment keeps its value high, around 0.9, as intended. However, after the third iteration, around 132 s of physical time, the reflected power starts to increase continuously, despite the plunger adjustment, represented by the sharp decrease in the value of $1 - |S_{11}|^2$. Between 750 s and 1750 s, the increase of the reflected power starts to slow down and eventually the value of $1 - |S_{11}|^2$ slightly increases. After that period, the curve shows again a decrease, converging to a value of 0.494

when steady-state is achieved. The behavior of this curve shows that after the initial iterations, the plunger adjustment has little influence on the value of $1 - |S_{11}|^2$, and consequently on the microwave efficiency. This behavior can be explained by the cut-off frequency phenomenon reported in [23, 27-28] which will be discussed in more detail later on.

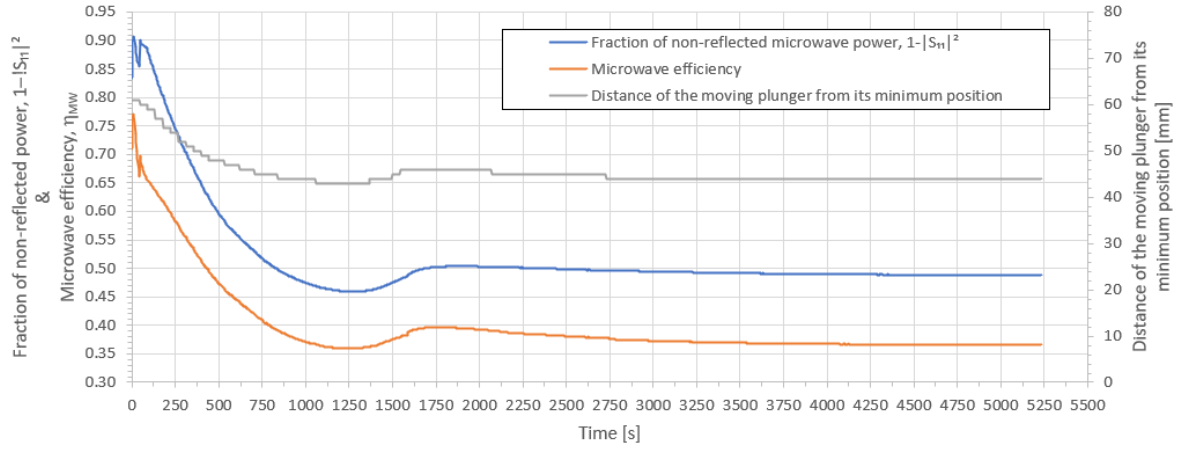


Figure 4.8: Fraction of non-reflected microwave power, microwave efficiency and plunger position evolution during the physical time.

As the temperature of the glass starts to increase, so do its dielectric properties as shown in Figure 3.6. Recalling Equation (2.35), the penetration depth, δ , decreases when the dielectric properties increase. For the present case, at steady-state, the value of δ is close to 1 mm which means that the microwave power is being absorbed in a thin outer layer of glass. By definition of penetration depth, the electric field practically vanishes after that penetration length, and since, in the present case, the ratio δ/r_i is very small, being r_i the inner radius of the applicator tube, the microwave radiation sees the glass material as a poor absorber. As discussed in Section 2.6.3, an electromagnetic wave cannot propagate when the distance between two reflector walls are less than half of the cut-off wavelength, $\lambda_{c_{10}}/2$. So, for the present case where tube's inner diameter is $d_i = 30$ mm, the distance between the tube's inner surface and the waveguide walls is not enough to allow the propagation of the radiation, meaning that the electric field is very low in the region between the load and the moving plunger as depicted in Figure 4.9.

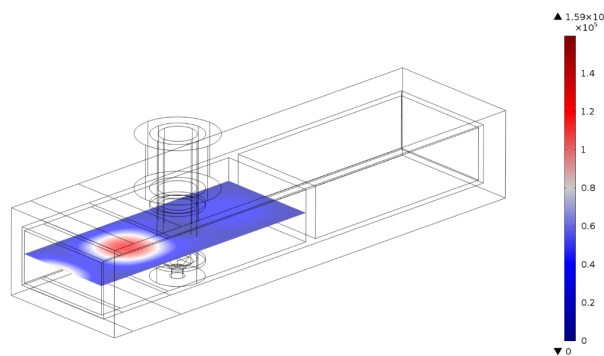


Figure 4.9: Electric field norm [V/m] in the microwave cavity at the steady-state.

Since practically no electric field reaches the moving plunger, its adjustment has very little influence on the microwave efficiency. Besides that, since the electric field is strongly attenuated when turning around the load, the radiation is being absorbed in a thin layer that is not axisymmetric but appears only in the tube side facing the microwaves as shown in Figure 4.10. In this figure the distributions of the electric field norm, loss factor and heat source in the glass region are presented. Recalling Equation (2.29), the heat source due to microwave absorption is proportional to the square of the electric field norm and to the loss factor. It is then expected that the heat source will be higher in those regions where electric field and loss factor higher values intersect. Figure 4.10 shows that due to rotation, the loss factor distribution is axisymmetric. However, as stated above, the electric field distribution presents high values in a thin layer only on the side of the tube facing the radiation and very lower values on the opposite region. As the absorbing region is confined only to that side of the tube, the volume of glass that is effectively absorbing the microwave radiation is small relatively to the total volume and since the glass temperature is continuously rising, the penetration depth is continuously decreasing, reducing the thickness of this absorbing layer. This is the reason why, for this tube diameter, the value of $1 - |S_{11}|^2$ and, consequently, of η_{MW} , converge to a low value. As stated before, this discussion will be addressed again in the following sections.

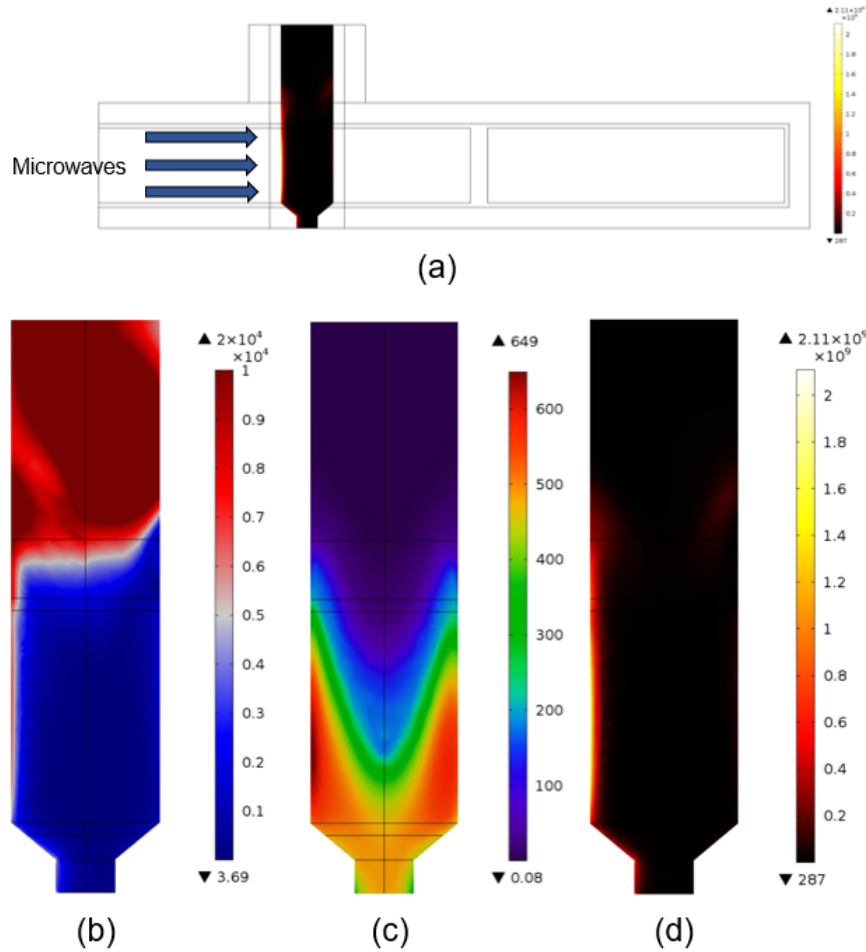


Figure 4.10: Heat source [W/m³] distribution, (a), in the glass thin layer facing the incoming microwave radiation. Distributions of the (b) electric field norm [V/m], (c) loss factor and (d) heat source [W/m³] in the glass region at the steady-state.

The microwave efficiency curve presents the same behavior discussed so far. However, this curve is shifted down, relatively to the curve representing the fraction of non-reflected microwave power. This shift is because, as stated earlier, the microwave efficiency accounts not only for the reflected power but also for the leaked radiation through the inlet and outlet surfaces of the tube and glass regions. It can be concluded, recalling Equation (3.24), that the ratio between the power leakage and the power input, is kept almost constant along the process evolution.

To justify the slight increase in the microwave efficiency between 1250 s and 1750 s it is useful to observe Figure 4.11 where it can be seen that during this time interval phase change is occurring at the outlet region and that the temperature in this region is almost constant and equal to the melting temperature. Since the volume that is effectively absorbing radiation is related to the penetration depth and since, during this time interval, the value of δ is kept constant in that region, as the power input continuously increases so does the microwave efficiency. If a constant volume of material is absorbing an increasing power input, the rate of increase in the power absorbed is higher than if that volume was continuously decreasing. After the phase change, the temperature of the glass starts to rise again and, consequently, the penetration depth is reduced, leading to a decrease in the microwave efficiency until steady-state is achieved.

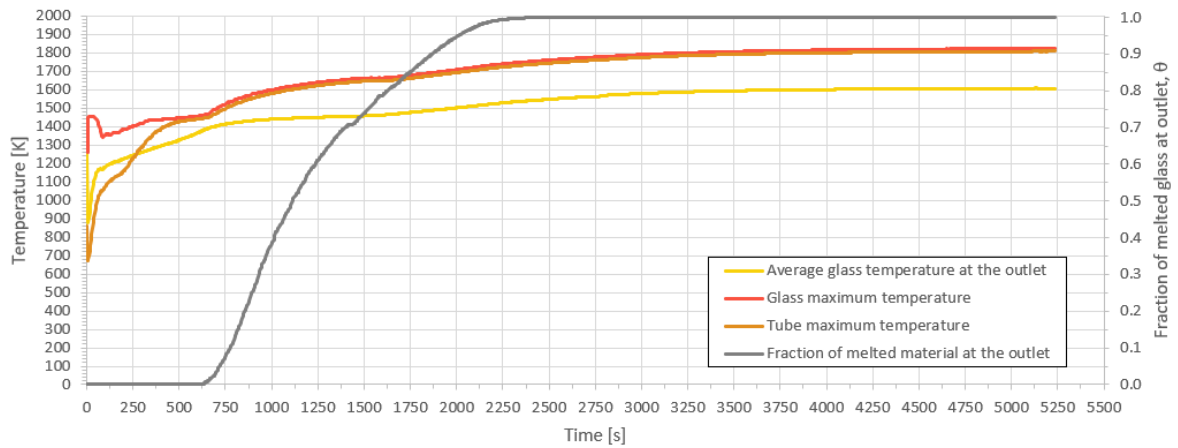


Figure 4.11: Average outlet glass temperature, maximum glass temperature, maximum tube temperature and outlet fraction of melted material evolutions during the physical time.

Figure 4.11 presents the evolution of the glass average outlet and maximum temperatures, the tube maximum temperature and the outlet fraction of melted glass. Regarding the glass average outlet temperature, it is noticed that during the first iteration, its value drops sharply from 1273 K to around 900 K. This happens because initially the outlet region is the hottest place in the glass. It is also in this region that the highest glass velocities are present due to its narrower diameter. Since the highest absorption region is quite above the outlet, the initially hot material flows out of the tube before the new hot material has time to get to the outlet. Another cause for that temperature drop is the fact that, in the first iteration, the *MATLAB* controller does not consider the thermal losses when computing the required power input. After the first iteration, the glass average outlet temperature continuously rises until it stabilizes at 1607 K when steady-state is achieved.

Concerning the glass maximum temperature, it is observed that there is an initial sharp increase mainly due to the high microwave efficiency in that period. After the third iteration the maximum temperature drops and then starts a continuous increase until steady-state is achieved. Between 300 s and 600 s it is observed that the maximum temperature stabilizes around the melting temperature, illustrating the phase change occurring in the region of highest microwave absorption. The tube maximum temperature also experiences a decrease in the first iteration, following the glass outlet temperature behavior. After that period, this temperature starts to approach the glass maximum temperature, both being practically the same during the rest of the simulation. This happens because, as verified above, the microwave absorption occurs in a very thin layer of glass near the tube's inner walls, so both maximum temperature locations are near each other reducing the margin for differences. The curve representing the outlet fraction of melted glass shows that, at steady-state, the exiting glass is completely processed as desired. It is also possible to conclude that an outlet average temperature of 1600 K was not necessary to have 100% of melted glass at the outlet. However, since different operational conditions will be studied in this work, and in order to account for possible high thermal gradients at the outlet due to the increase of the tube's diameter or of the mean flow velocity, this average outlet temperature was chosen.

In Figure 4.12 the evolution of the control variables from the *MATLAB* algorithm are presented. The microwave efficiency curve has been already discussed above. Regarding the power input evolution, it is observed that its continuous increase is mainly caused by the decrease in the microwave efficiency following Equation (3.31). The thermal losses across the exterior boundaries of the microwave cavity also contribute to the power input increase. Between 1250 s and 1750 s a decrease in the power input is observed due to the increase in the microwave efficiency in the same time interval. Relatively to the plunger position adjustment, it has been mentioned that, for the present case, it has little influence on the microwave efficiency after the first couple of iterations, when the glass temperatures reach values that keep the penetration depth close to 1 mm. However, it will be seen later that, although this influence is small, it is always better than not having any plunger adjustment at all and that for smaller tube diameters the plunger position adjustment will play a fundamental role in the process.

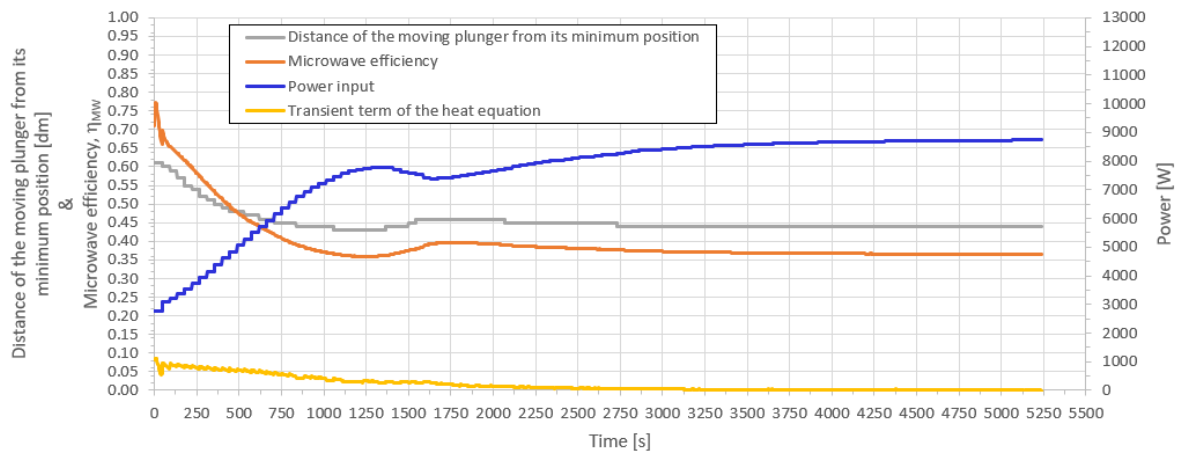


Figure 4.12: Power input, microwave efficiency, transient term of the heat equation and plunger position evolutions during the physical time.

Figure 4.13 shows how the power input is being distributed in the system. As discussed before, there is a considerable fraction of this power that is being reflected. Another relevant fraction of the power input is leaking from the cavity. This power leakage has less influence than the reflected power but still represents around 12% of the power input and this percentage is practically kept constant during the process evolution, as discussed before. The fraction of the power input that is not reflected nor escapes is absorbed by both glass and tube. Additionally, the power absorbed evolution curve is also depicted in Figure 4.13.

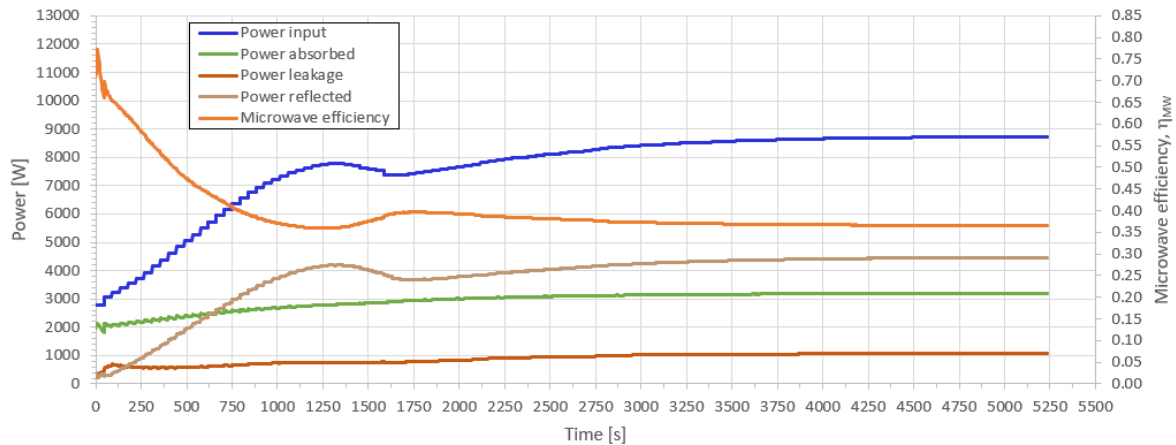


Figure 4.13: Power input, power absorbed, power leakage, power reflected and microwave efficiency evolution during the physical time.

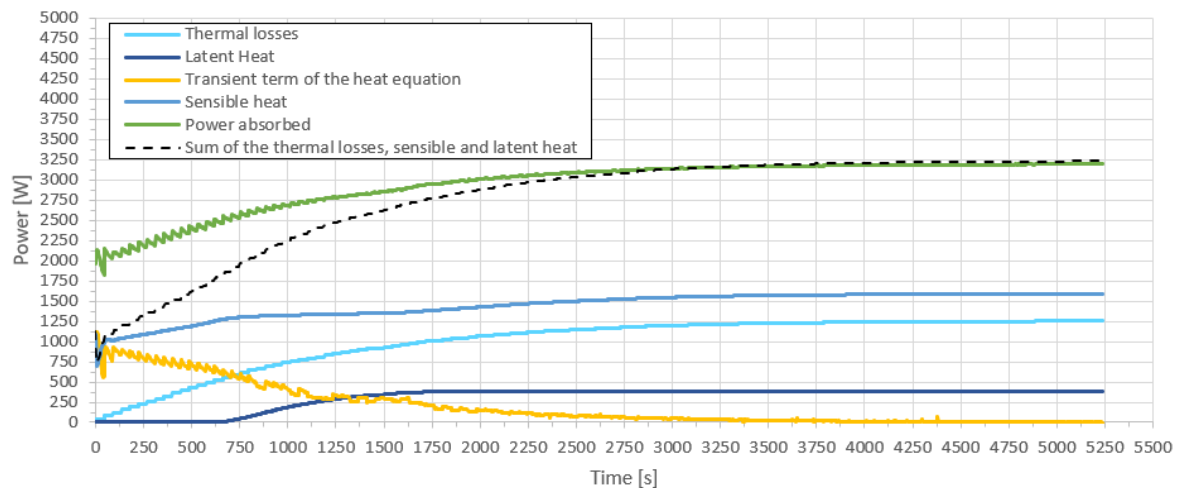


Figure 4.14: Power absorbed, transient term of the heat equation, sensible and latent heat at the outlet and thermal losses evolutions during the physical time.

The evolution of each energy term, used in an energy balance, is illustrated in Figure 4.14. The power absorbed by both glass and tube is obtained by adding the sensible heat, latent heat, thermal losses and the transient term of the heat equation. Regarding the transient term of the heat equation, it is shown that it approaches zero from positive values, meaning that the energy of the system is increasing, resulting in the rise of the glass temperature, until steady-state is achieved. The dotted line represents the sum of the sensible heat, latent heat and thermal losses. It can be noted that when the

transient term of the heat equation approaches zero, *i.e.*, when the steady-state is being reached, the dotted line tends to the power absorption curve as expected, meaning that all the power absorbed is being used to rise the material temperature, change the material phase and overcome the thermal losses. The difference between both curves gives information about how far the solution is from steady-state.

In Figure 4.15 the energy balance of the system is schematically represented. For the studied operational conditions 51% of the microwave power input is reflected, 12% is escaping as microwave leakage and only 37% is being absorbed by the glass and tube, indicating that for this case the microwave efficiency is $\eta_{MW} = 37\%$. Of the power that is effectively absorbed by both glass and tube, 49% is being used to heat the glass from 293 K to 1600 K, 12% is being used in the glass phase change and 39% is being lost as convection and radiation through the microwave cavity exterior walls. Since only the sensible and latent heat are useful power in the process, the thermal efficiency is, for this case, $\eta_T = 61\%$.

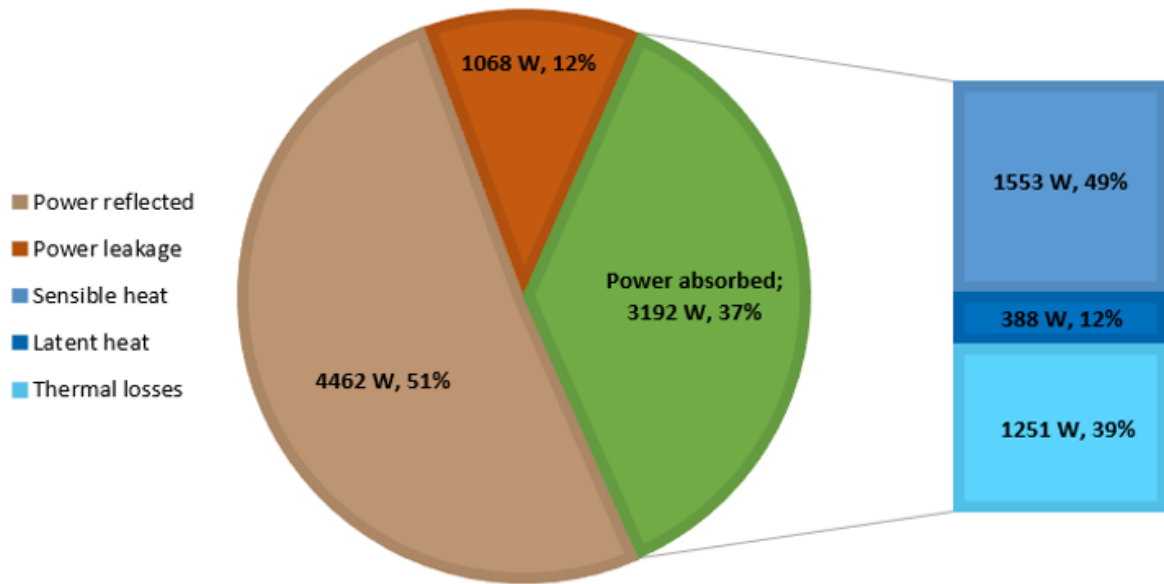


Figure 4.15: Complete energy balance of the microwave cavity for the case with $d_i = 30$ mm and $\dot{m} = 3.6$ kg/h.

The global efficiency, calculated as the product of the microwave efficiency, the thermal efficiency and the outlet fraction of melted material, is $\eta_G = 23\%$. Another key performance indicator, KPI, is the specific energy consumption, SEC [J/kg], which represents the amount of energy required to process 1 kg of glass and it is given by:

$$SEC = \frac{P_{in}}{\dot{m} \cdot \theta} \quad (4.11)$$

which, for the present case, is equal to $SEC = 8722.6$ kJ/kg. This value can be compared to the data given in [1], where it is stated that for the conventional glass melting process, the European average specific energy consumption in 2007 was $SEC_{conv} = 7800$ kJ/kg. The SEC value obtained for the microwave heating process represents an increase of around 12% in the energy consumption per kilogram of processed material. However, it is important to notice that, for the studied operational conditions, the global efficiency of the process was very low, $\eta_G = 23\%$, indicating that significant improvements can be made. Besides that, it is also important to highlight that using microwaves as the heating source has a tremendous impact in environmental issues since there are no direct emissions of CO_2 . Another advantage in using microwaves is the significant reduction in the process duration, since to achieve the steady-state around 1 hour was needed which represents a decrease of around 80% relatively to the conventional process [12]. The overall steady-state results are summarized in Table 4.6.

Table 4.6: Steady-state results for the glass melting process with $d_i = 30$ mm and $\dot{m} = 3.6$ kg/h.

Variable	Value
Power input, P_{in} [W]	8722
Power reflected, P_{ref} [W]	4462
Power leakage, P_L [W]	1068
Power absorbed, P_{abs} [W]	3192
Sensible heat at outlet (theoretical, SH_{needed} / obtained, SH) [W]	1551/1553
Latent heat at outlet (theoretical, LH_{needed} / obtained, LH) [W]	388/388
Thermal losses, P_{Loss} [W]	1251
Outlet Fraction of melted material, θ [%]	100
Glass maximum temperature, $T_{G,max}$ [K]	1823
Tube maximum temperature, $T_{T,max}$ [K]	1808
Glass average outlet temperature, T_{out} [K]	1607
Microwave efficiency, η_{MW} [%]	37
Thermal efficiency, η_T [%]	61
Global efficiency, η_G [%]	23
Specific energy consumption, SEC [kJ/kg]	8722

4.5 Influence of plunger position updates, microwave leakage and *slip* boundary condition

As have been introduced earlier, in the numerical simulations done so far it was assumed the presence of microwave leakage on the tube's inlet and outlet, a *no-slip* boundary condition was used in the tube inner walls and a plunger position adjustment was performed every iteration in order to maximize the microwave efficiency. In this section, three studies are presented with the purpose of showing how these model parameters influence the glass melting process by running a set of simula-

tions without the plunger position adjustments (Subsection 4.5.1), without the presence of microwave leakage (Subsection 4.5.2) and with a *slip* boundary condition on the tube inner walls (Subsection 4.5.3). All three studies were run for operational conditions with $d_i = 30$ mm and $\dot{m} = 3.6$ kg/h.

4.5.1 Plunger position updates

To investigate how the plunger position adjustments affect the glass heating process and the respective steady-state results, a set of four simulations were carried out. In the first two, a tube with an inner diameter of $d_i = 30$ mm was used. For the other two, a value of $d_i = 15$ mm was chosen. Using Equation (4.9), the mass flow rate was set in order to have the same mean flow velocity, $U_{ave} = 0.64$ mm/s, for all cases. In each pair of simulations, one was run with the plunger position adjustments and the other with the plunger position kept constant during the simulation. The operation conditions described above are compiled in Table 4.7.

Table 4.7: Operation conditions of the numerical simulations.

Operational conditions			
	Mass flow rate, \dot{m} [kg/h]	Tube inner diameter, d_i [m]	Plunger adjustments
Simulation 1	3.6	30	Yes
Simulation 2	3.6	30	No
Simulation 3	0.9	15	Yes
Simulation 4	0.9	15	No

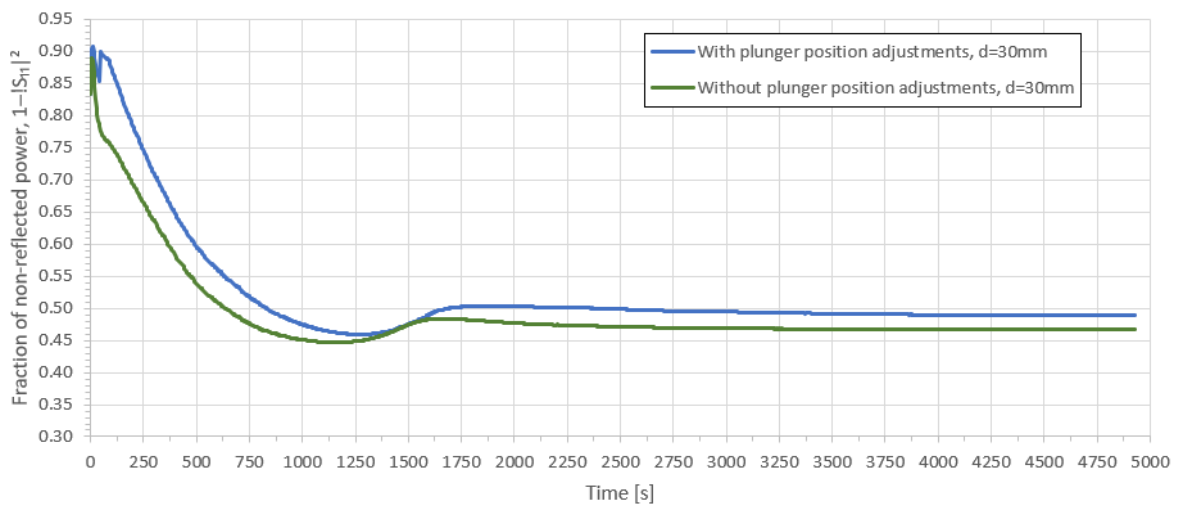


Figure 4.16: Fraction of non-reflected microwave power evolution during the physical time, for $d_i = 30$ mm, with and without plunger position adjustments.

The evolution of the fraction of non-reflected microwave power during the glass heating process for the case with $d_i = 30$ mm is shown in Figure 4.16. Although the curve obtained with the plunger position adjustments have already been commented in Section 4.4, it is interesting to compare it with the curve obtained without these adjustments, *i.e.*, with the plunger kept in a constant position during the process. In the first iterations, when the glass temperatures are low and the penetration depth is large, the plunger position adjustments prove to be very effective, keeping the value of $1 - |S_{11}|^2$ close to 90%. However, as discussed before, as the temperature increases so do the glass dielectric properties contributing to a decrease in the penetration depth and, consequently, to a decrease in the fraction of non-reflected power. At this stage, after 400 s of physical time, due to the large inner tube diameter, the electric field is strongly attenuated when turning around the load because of the cut-off phenomenon already described. Since the magnitude of \vec{E} is very low in the region between the load and the moving plunger, the latter's position adjustments have little influence on the process. This can be attested by the almost perfect vertical shift observed between both curves. Besides that, the converged results for both cases show a difference of only 2.5% in the value of $1 - |S_{11}|^2$ and, consequently, on the value of the microwave efficiency, η_{MW} .

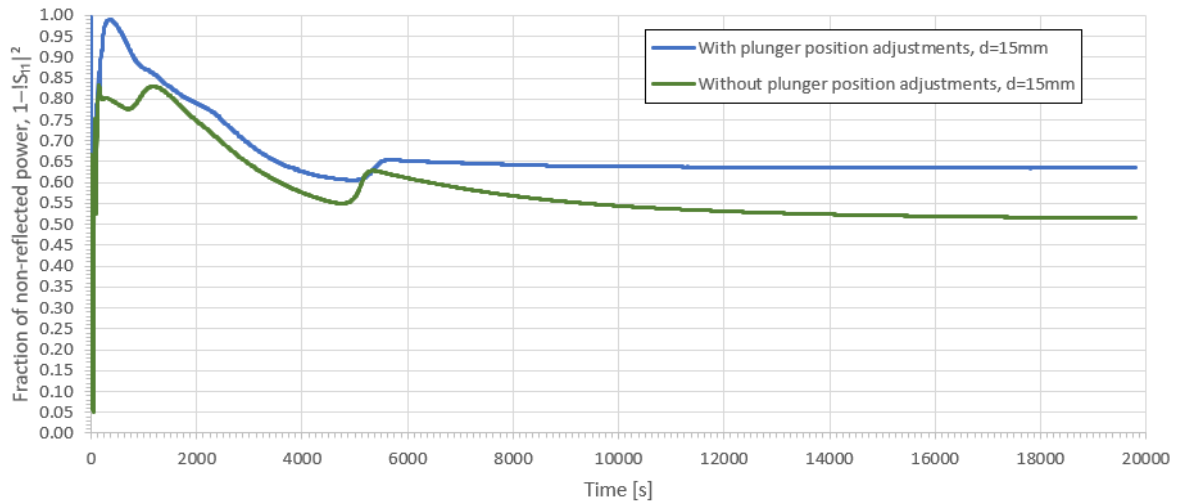


Figure 4.17: Fraction of non-reflected microwave power evolution during the physical time, for $d_i = 15$ mm, with and without plunger position adjustments.

The same analysis has been done for a tube with $d_i = 15$ mm and the evolution of the fraction of non-reflected microwave power with and without plunger position adjustments are shown in Figure 4.17. It can be observed that in the first iteration, there is a tremendous decrease in the value of $1 - |S_{11}|^2$ in both curves. This happens because the thermal losses are not considered in the initial power input, P_{in} , calculated by the *MATLAB* controller as justified earlier, and so, a significant decrease in the glass temperature takes place. With that high temperature drop, the dielectric properties experiment a drastic decrease, so does the ability of the glass to absorb the microwave power. In the second iteration, the power input is updated considering the thermal losses measured and the glass temperatures rise again and so there is an improvement in the microwave absorption ability. During the initial period of the heating process, the plunger position adjustments allow the value of $1 - |S_{11}|^2$ to be above 90%. How-

ever, as the glass temperatures continues to rise, the penetration depth decreases, and the fraction of non-reflected microwave power starts to drop, converging to a value around 63%.

Comparing the results presented in Figures 4.16 and 4.17, it can be observed that for the case with $d_i = 15$ mm, there is no longer a perfect vertical shift between the curves obtained with and without plunger position adjustments as it was seen for the case with $d_i = 30$ mm. Although in both cases the value of $1 - |S_{11}|^2$ experiments a drop as the glass heats up, for the case with $d_i = 15$ mm the plunger position adjustments have a considerable influence on the process allowing a reduction in the rate of decrease of the $1 - |S_{11}|^2$ curve. This happens due to the lower inner tube diameter which reduces the influence of the cut-off frequency phenomenon, allowing the electric field to turn around the glass more easily and contributing to an improvement of the moving plunger influence on the distribution of the electric field inside the microwave cavity, as illustrated in Figure 4.18. For that reason, the converged results with and without plunger position adjustments show a difference of almost 12% in the value of $1 - |S_{11}|^2$.

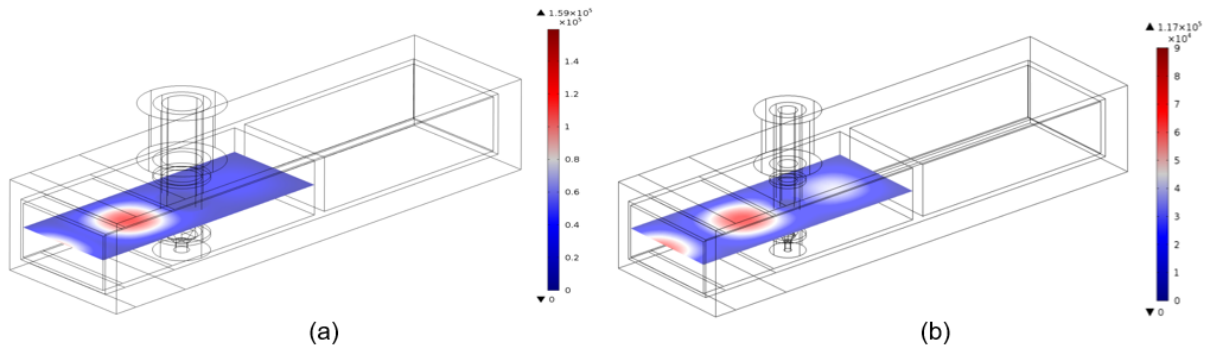


Figure 4.18: Electric field norm [V/m] in the microwave cavity at steady-state, for the case with (a) $d_i = 30$ mm and (b) $d_i = 15$ mm.

The influence of the plunger position adjustments in the glass heating process and in its converged results is clearly dependent on the tube's inner diameter, d_i , increasing as the latter decreases. However, the results presented in this study show that the use of plunger position adjustments is always a better solution than keeping the moving plunger in a fixed position, since it increases the microwave efficiency.

4.5.2 Microwave leakage

As it was observed so far, radiation leakage through the tube's inlet and outlet represent a considerable power loss in the glass melting process and, consequently, a relevant penalty for the microwave efficiency, η_{MW} . As described earlier, this power loss was modelled by assigning a *scattering* boundary condition to the surfaces where it occurs. In order to compare the steady-state results with and without microwave leakage, a simulation was run with a model in which, for those surfaces, a *perfect*

electrical conductor boundary condition was assigned. The relevant results obtained for both cases are presented in Table 4.8.

Table 4.8: Comparison of the steady-state results with and without microwave radiation leakage.

Variable	Value	
	With leakage	Without leakage
Power input, P_{in} [W]	8722	7352
Power absorbed, P_{abs} [W]	3192	3170
Sensible heat at outlet (theoretical, SH_{needed} / obtained, SH) [W]	1551/1553	1551/1552
Latent heat at outlet (theoretical, LH_{needed} / obtained, LH) [W]	388/388	388/388
Thermal losses, P_{Loss} [W]	1251	1230
Microwave efficiency, η_{MW} [%]	37	43
Thermal efficiency, η_T [%]	61	61
Global efficiency, η_G [%]	23	26
Specific energy consumption, SEC [kJ/kg]	8722	7352

By analyzing the results shown in Table 4.8 it can be noticed that despite the thermal efficiency has remained practically the same, the microwave efficiency has increased from 37% to 43%. This happens mainly due to the fact the tube's inlet and outlet boundaries are no longer permeable to the electromagnetic radiation. Instead, reflection phenomena occurs in those regions allowing the electric field to be more intense in the domain between the load and the moving plunger as depicted in Figure 4.19. This means that not only there are no more radiation losses but also there is a better heat source distribution since there is a slight increase in the electric field and, consequently, in the heat source in a thin layer at the back side of the glass domain.

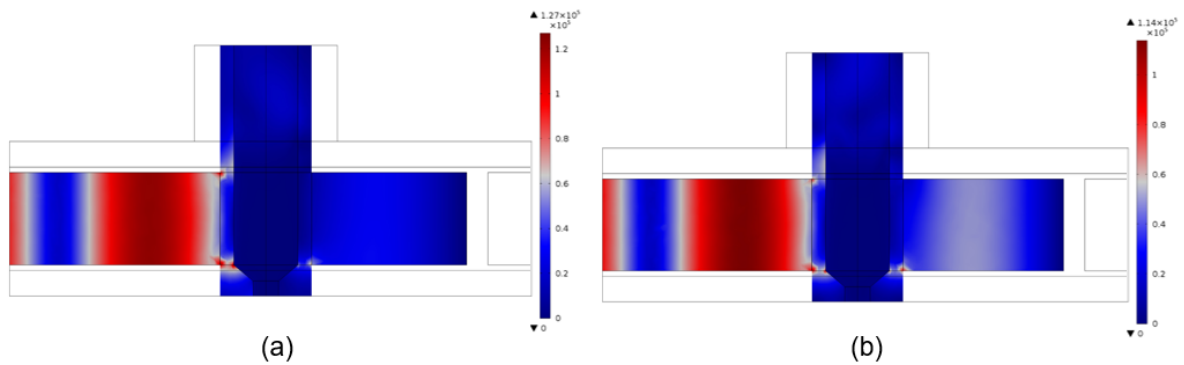


Figure 4.19: Electric field norm [V/m] in the microwave cavity at steady-state for the case (a) with and (b) without microwave radiation leakage.

The observed increase in the microwave efficiency contributes to a power input reduction of almost 16% which is reflected in the decrease of the specific energy consumption. This analysis allows to conclude that microwave leakage has a considerable impact on the continuous glass melting process and should be avoided, or limited, as much as possible.

4.5.3 *Slip* boundary condition

As mentioned earlier, the glass enters the tube in powder state and at ambient temperature. Its only when the phase change starts to occur that it begins to behave as a fluid. Modelling this complex flow is computationally expensive and it is beyond the goals of this Thesis. To simplify, the glass flow inside the tube was modelled as laminar, assuming fluid behavior everywhere and ignoring the influence of the solid particles flow. One of the differences between a solid particle and a fluid flow is the interaction with the tube walls. For fluid flows, the velocity must be zero at the walls which is modelled by imposing a *no-slip* boundary condition in the inner surface of the tube. However, when the material that flows is composed by small solid particles, non-zero velocities appear at the walls so a *slip* boundary condition must be used instead. With the objective to analyze the difference between both models, the glass melting process was simulated with a *slip* boundary condition assigned to the tube inner walls. The relevant steady-state results obtained for both cases are presented in Table 4.9.

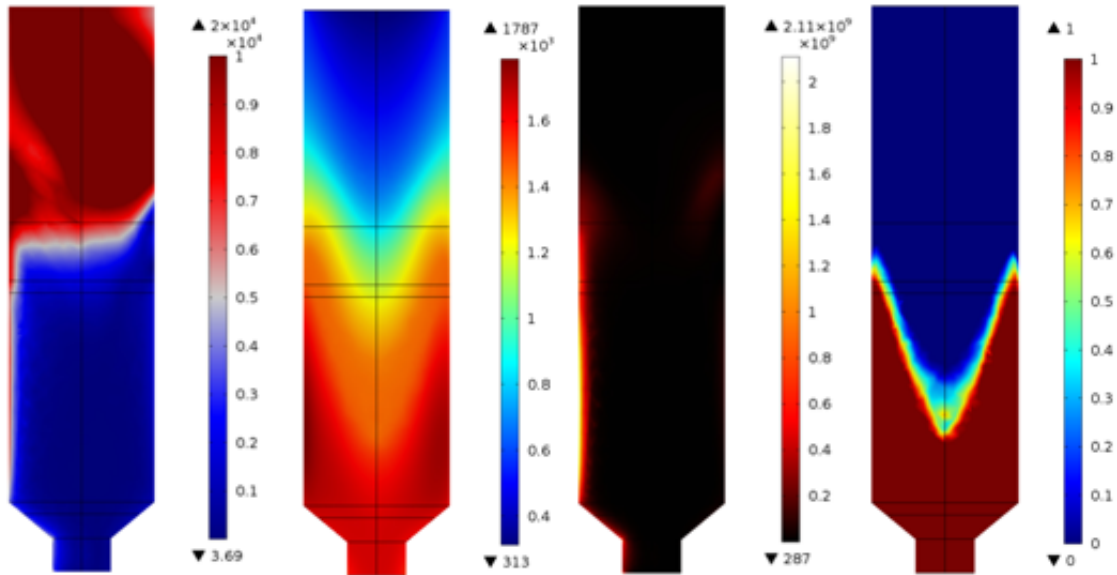
Table 4.9: Comparison of the steady-state results obtained using *no-slip* and *slip* boundary conditions at the tube inner walls.

Variable	Value	
	<i>No-slip</i> B.C.	<i>Slip</i> B.C.
Power input, P_{in} [W]	8722	8214
Power absorbed, P_{abs} [W]	3192	3125
Sensible heat at outlet (theoretical, SH_{needed} / obtained, SH) [W]	1551/1553	1551/1552
Latent heat at outlet (theoretical, LH_{needed} / obtained, LH) [W]	388/388	388/388
Thermal losses, P_{Loss} [W]	1251	1184
Microwave efficiency, η_{MW} [%]	37	38
Thermal efficiency, η_T [%]	61	62
Global efficiency, η_G [%]	23	24
Specific energy consumption, SEC [kJ/kg]	8722	8214

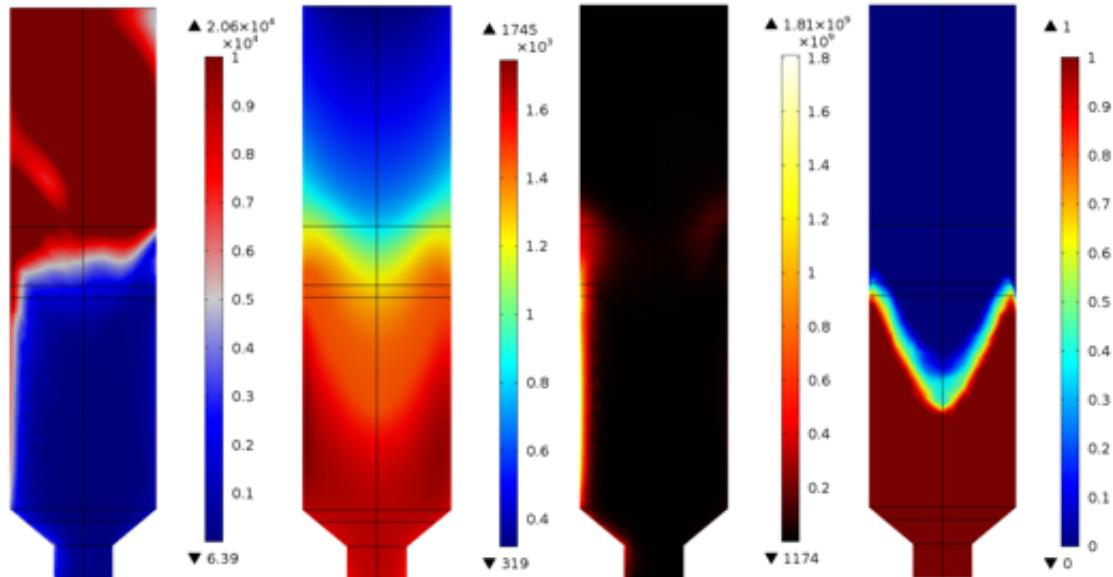
Regarding Table 4.9, it can be seen that modelling the glass flow with a *slip* boundary condition allows a slight increase in the microwave efficiency and, consequently, a reduction in the specific energy consumption. This occurs mainly due to the differences observed in the thermal field as shown in Figure 4.20. Since the velocities at the walls are not zero, the radial thermal gradients are significantly smaller and a slight decrease in the temperatures can be observed, especially in the thin layer region where the

heat absorption occurs. Consequently, the penetration depth experiences a small increase in the *slip* boundary condition model contributing to a slight increase in the microwave efficiency.

Despite the slight increase in performance, most of the heat absorption occurs after the phase change takes place, *i.e.*, when the glass is behaving as a fluid. For that reason, and since the differences between the global results for both cases are small, it was decided that the *no-slip* boundary condition was more realistic and, therefore, used throughout this work.



(a)



(b)

Figure 4.20: Distributions of the electric field norm [V/m], temperature [K], heat source [W/m³] and fraction of melted phase in the glass region at steady-state, for the case with (a) *no-slip* and (b) *slip* boundary conditions at the tube inner walls.

4.6 Tube inner diameter and mean flow velocity parametric studies

In this section, a detailed analysis of the influence that the tube inner diameter and the glass mean flow velocity have on the efficiency of the melting process is presented. In Subsection 4.6.1, a parametric study is presented showing the effect of changing the diameter for a fixed mean flow velocity. Another parametric study showing the influence of changing the mean flow velocity for a fixed diameter is presented in Subsection 4.6.2. Finally, a combined parametric study is presented in Subsection 4.6.3, showing how the global efficiency varies in a given study domain and allowing to check the existence of optimum operational conditions.

4.6.1 Influence of the diameter for a fixed mean flow velocity

This subsection aims to quantify and study the influence that the applicator tube inner diameter exerts on the glass melting process, namely on its global efficiency. In this parametric study, the mean flow velocity was kept constant and equal to $U_{ave} = 0.64$ mm/s. In order to fulfill the purpose of this study, a set of simulations were carried out, whose operational conditions are summarized in Table 4.10.

Table 4.10: Operational conditions for the simulations done in the diameter parametric study.

	Operational conditions		
	Mean flow velocity	Tube inner diameter	Mass flow rate
	U_{ave} [mm/s]	d_i [mm]	\dot{m} [kg/h]
Simulation 1	0.64	12	0.58
Simulation 2	0.64	14	0.78
Simulation 3	0.64	15	0.90
Simulation 4	0.64	17	1.16
Simulation 5	0.64	20	1.60
Simulation 6	0.64	23	2.12
Simulation 7	0.64	28	3.14
Simulation 8	0.64	30	3.60
Simulation 9	0.64	31	3.85
Simulation 10	0.64	40	6.40
Simulation 11	0.64	54	11.67

The converged values for the fraction of non-reflected microwave power, $1 - |S_{11}|^2$, microwave efficiency, η_{MW} , thermal efficiency, η_T , outlet fraction of melted material, θ , and global efficiency, η_G , for each simulation are presented in Figure 4.21. Comparing the $1 - |S_{11}|^2$ and η_{MW} curves, it is observed that despite a greater presence of microwave leakage for $12 \text{ mm} \leq d_i \leq 14 \text{ mm}$, for diameters above 15 mm the ratio between the microwave leakage and the power input is kept practically constant, around

10%. It can also be concluded that there is a clear tendency for the microwave efficiency to increase as the diameter decreases, mainly because the fraction of non-reflected microwave power increases for smaller diameters.

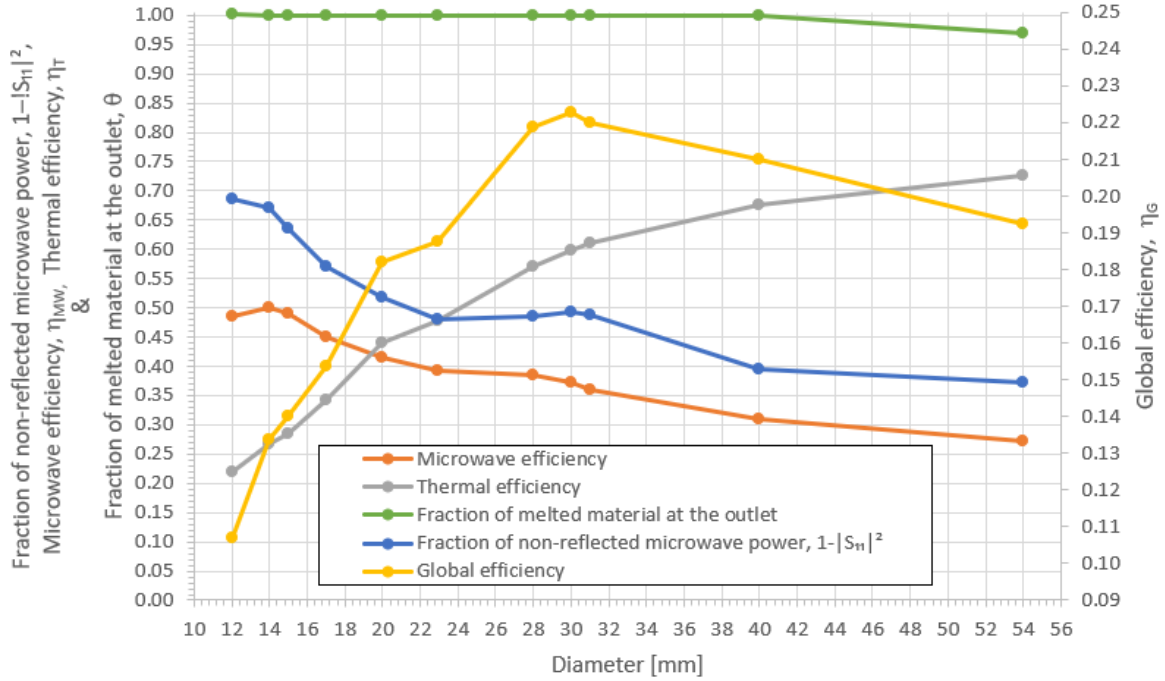


Figure 4.21: Fraction of non-reflected microwave power, $1 - |S_{11}|^2$, microwave efficiency, η_{MW} , thermal efficiency, η_T , outlet fraction of melted material, θ , and global efficiency, η_G , versus tube inner diameter, d_i , for a constant mean flow velocity of $U_{ave} = 0.64$ mm/s.

By analyzing the $1 - |S_{11}|^2$ curve, the studied diameters can be grouped into two classes. The first class is constituted by the smaller diameters where $12 \text{ mm} \leq d_i < 20 \text{ mm}$ and the second one is represented by diameters above $d_i \geq 20 \text{ mm}$. This classification is strongly related to the cut-off frequency effect reported in [23, 27-28] and already discussed in this work.

As discussed in Section 4.4, due to the low penetration depths observed, which are illustrated in Figure 4.22, the cut-off frequency effect strongly contributes to the existence of a high fraction of reflected microwave power. As the diameter decreases, the electric field starts to be attenuated only when the distance between the tube and cavity walls is minimum, contributing to an increase of the external area of the glass absorbing layer, until $d_i = 30 \text{ mm}$, as illustrated in Figures 4.23d and 4.23e. For diameters in the interval $20 \text{ mm} < d_i < 30 \text{ mm}$, as the diameter continues to decrease, the slight decrease in the $1 - |S_{11}|^2$ curve is justified by the decrease in the external area of the glass absorbing layer, as depicted in Figures 4.23c and 4.23d. However, for the same interval, the microwave efficiency, η_{MW} , rises due to a drop in the microwave leakage.

For diameters belonging to the first class, where $12 \text{ mm} \leq d_i < 20 \text{ mm}$, the cut-off frequency phenomenon is less intense, and the electric field can properly propagate around the load as illustrated in Figure 4.18. This allows the glass absorbing layer to become axisymmetric, contributing to higher microwave absorption, as presented in Figures 4.24a, 4.24b and 4.24c. As the diameter decreases, the

sharp increase in the $1 - |S_{11}|^2$ curve between $12 \text{ mm} \leq d_i < 20 \text{ mm}$ is also caused by geometric reasons. At the outlet region of the tube, the diameter, d_{out} , is smaller than d_i and $\delta/r_{out} \approx 1$, which causes an increase in the heat source distribution in that region, as illustrated in Figures 4.24a and 4.24b. This increase in the heat source at the tube outlet region causes a temperature rise and, consequently, a decrease in the penetration depth, depicted in Figures 4.22a and 4.22b. Regarding the η_{MW} curve, the decrease observed for $d_i = 12 \text{ mm}$ is due to the increase of the microwave leakage caused by the high electric field intensity in the outlet region of the tube.

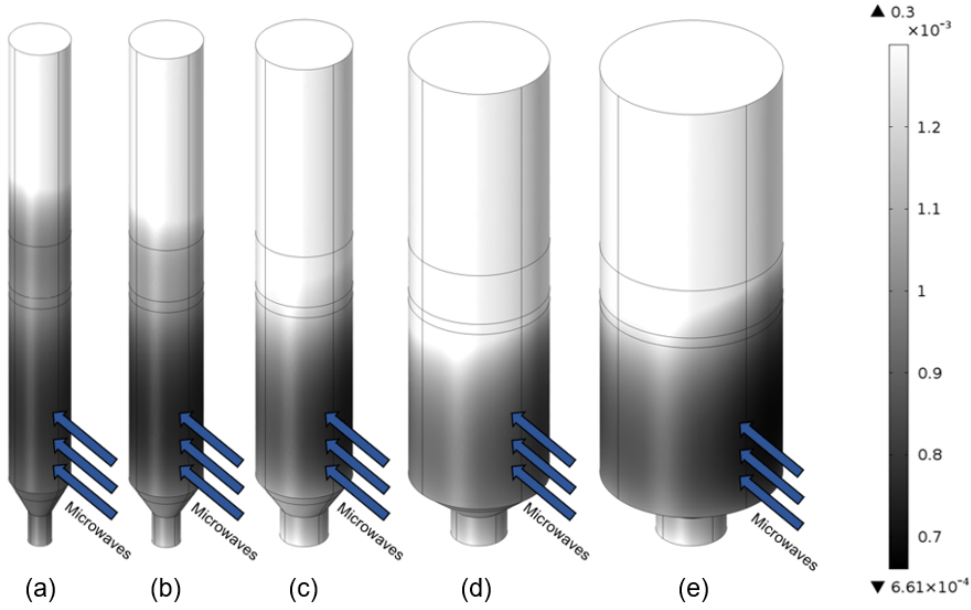


Figure 4.22: Penetration depth values for the converged solutions with (a) $d_i = 12 \text{ mm}$, (b) $d_i = 15 \text{ mm}$, (c) $d_i = 20 \text{ mm}$, (d) $d_i = 30 \text{ mm}$ and (e) $d_i = 40 \text{ mm}$. For all cases, the penetration depth is always below 1 mm in the glass outer surface inside the microwave cavity.

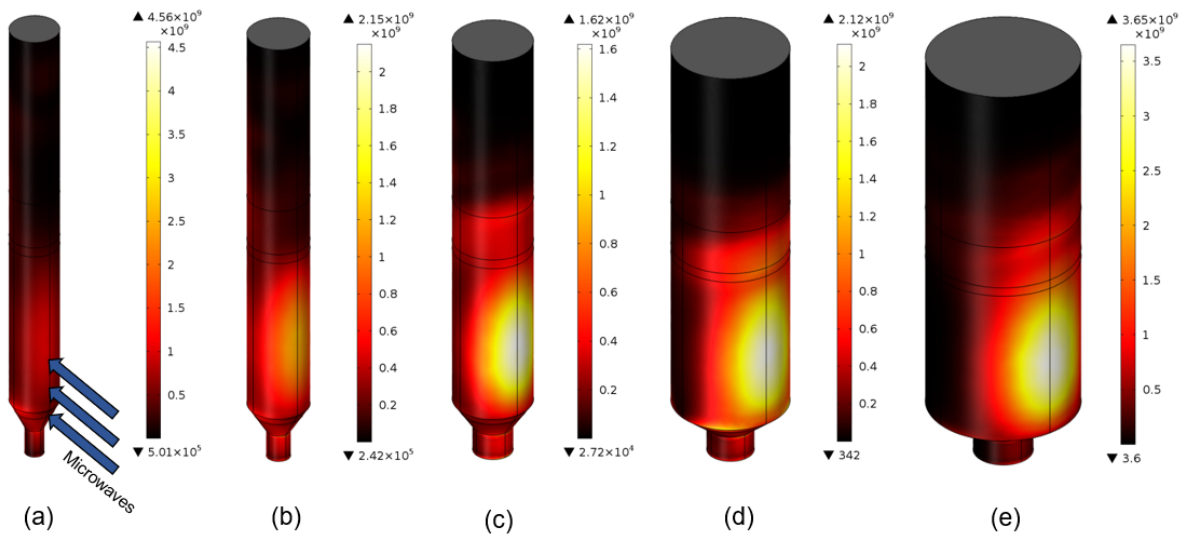


Figure 4.23: Heat source distribution $[\text{W}/\text{m}^3]$ in the external surface of the absorbing layer for (a) $d_i = 12 \text{ mm}$, (b) $d_i = 15 \text{ mm}$, (c) $d_i = 20 \text{ mm}$, (d) $d_i = 30 \text{ mm}$ and (e) $d_i = 40 \text{ mm}$.

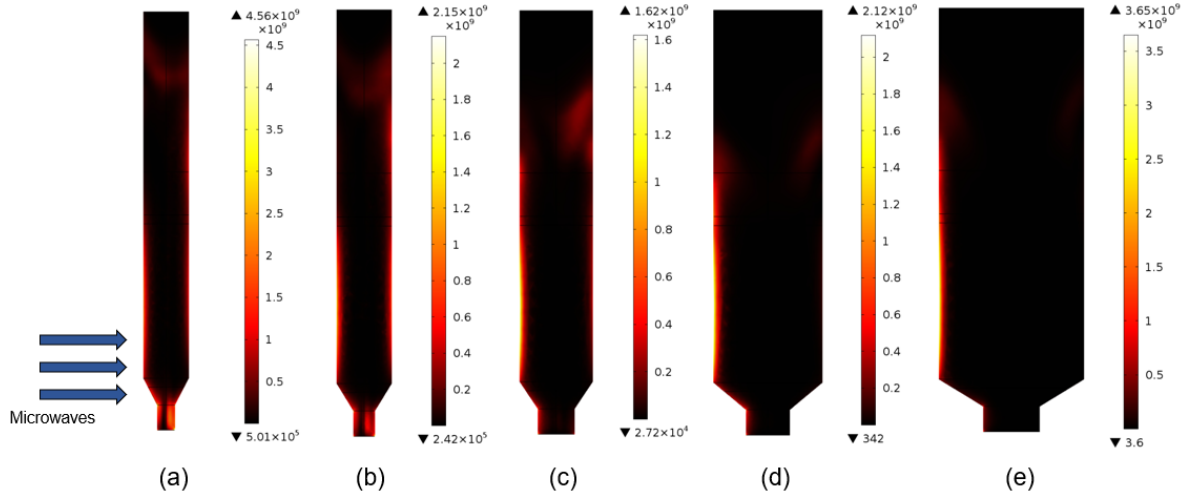


Figure 4.24: Heat source distribution [W/m^3] in the absorbing layer for (a) $d_i = 12$ mm, (b) $d_i = 15$ mm, (c) $d_i = 20$ mm, (d) $d_i = 30$ mm and (e) $d_i = 40$ mm. For diameters below $d_i = 20$ mm.

Despite the tendency for the microwave efficiency to increase as the tube inner diameter decreases, for manufacturing reasons, smaller diameters were not considered in this Thesis. Machining constraints such as drill lubrication, excessive vibrations, etc., require that when drilling a hole, the ratio between its depth and diameter should not be greater than 20 [60]. However, since boron nitride is a ceramic material with a brittle behavior, a minimum inner diameter of $d_i = 12$ mm was chosen for the applicator tube to guarantee good dimensional tolerances and that it would not break during the manufacturing process.

The thermal efficiency, η_T , curve, also presented in Figure 4.21 and calculated using Equation (3.26), shows a clear tendency to increase as the tube inner diameter increases. This trend is justified by the fact that, although there is an increase in the thermal losses as the diameter increases due to the maximum temperature rise, the ratio between these losses and the power absorbed is smaller for higher diameters and, therefore, a higher percentage of the power absorbed is used for the glass heating and phase change.

The curve showing the outlet fraction of melted material, θ , is also depicted in Figure 4.21. The glass leaves the tube completely processed for all cases except for the diameter $d_i = 54$ mm. In this last case, the heat generated in the external absorbing layer cannot reach the center of the glass region by diffusion and large thermal gradients along the radial direction appear. Since the inside region of the glass is not heated above the melting point, there is a percentage of material that leaves the tube in solid state.

Recalling Equation (3.28), the global efficiency of the process is calculated by multiplying the microwave and thermal efficiencies by the value of θ . This curve is also presented in Figure 4.21. It is observed that, initially the increase in the thermal efficiency compensates the decrease in the microwave efficiency contributing to an increase in the global efficiency. At $d_i = 30$ mm the global efficiency reaches a maximum and then starts to decrease because the drop in the microwave efficiency is stronger than the small rise of the thermal one. Besides that, for the case with $d_i = 54$ mm there is an extra penalty because θ is no longer unitary.

In order to verify the positive influence of the rotation imposed in the tube, a set of simulations were performed for different diameters with the same mean flow velocity of $U_{ave} = 0.64$ mm/s without rotation. The global efficiency dependency on the tube diameter, for the cases with and without rotation are presented in Figure 4.25.

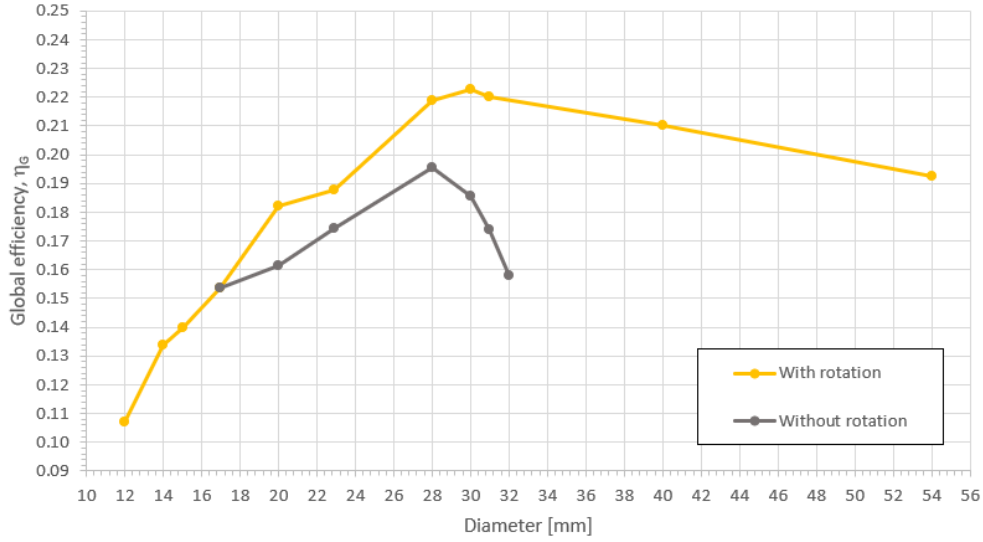


Figure 4.25: Global efficiency, η_g , versus tube inner diameter, d_i , for a constant mean flow velocity of $U_{ave} = 0.64$ mm/s, with and without tube rotation.

By observing Figure 4.25 it is evident that imposing rotation in the tube brings significant advantages to the glass heating process as already discussed in Section 4.3. Not only there is an improvement in the maximum value of the global efficiency, but also the critical diameter is larger when the rotation is used, allowing for more material to be processed with less power input. The sharper decrease in the curve without rotation after the critical diameter is explained by the decrease in the value of the outlet fraction of melted material, θ , which penalizes severely the global efficiency. As showed in Figure 4.2, rotation contributes significantly to the uniformization of the thermal field and favors the heat diffusion to the central region of the glass, allowing all material to be heated up above the melting temperature. If there is no rotation imposed to the tube, as the diameter increases, diffusion alone cannot heat up the central region of the glass and material in solid state starts to leave the tube, contributing to the sharp decrease in the global efficiency.

The influence of the tube inner diameter can also be evaluated in terms of the specific energy consumption, SEC , defined by Equation (4.11). Figure 4.26 shows the SEC curve versus the tube inner diameter and, as expected, its behavior presents a trend which is the inverse of the global efficiency one, meaning that for this mean flow velocity, the critical diameter of $d_i = 30$ mm presents the higher value for the global efficiency and the lower value for the specific energy consumption.

It can be concluded that for a mean flow velocity of $U_{ave} = 0.64$ mm/s there is a critical inner tube diameter of $d_i = 30$ mm which maximizes the global efficiency of the glass melting process. For values below and above the critical diameter, low thermal efficiencies and low microwave efficiencies, respectively, are responsible for the decrease in the global efficiency of the process.

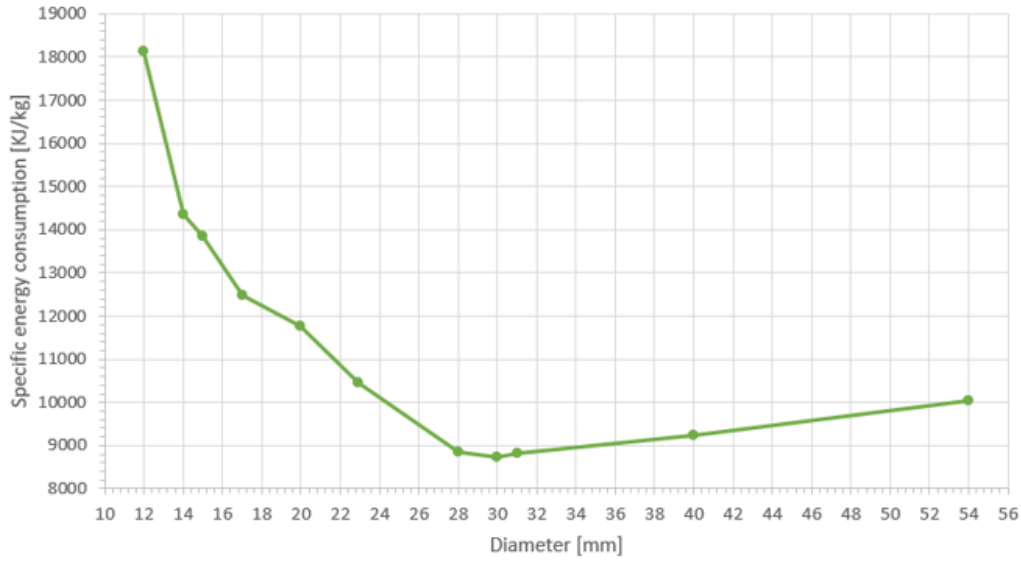


Figure 4.26: Specific energy consumption, SEC [kJ/kg], versus tube inner diameter, d_i , for a constant mean flow velocity of $U_{ave} = 0.64$ mm/s.

4.6.2 Influence of the mean flow velocity for a fixed diameter

In this subsection, another parametric study is presented with the aim of giving some insight on the influence that the mean flow velocity exerts on the process with a fixed diameter, $d_i = 30$ mm. To achieve this objective, a set of simulations were run, whose operational conditions are summarized in Table 4.11.

Table 4.11: Operational conditions for the simulations done in the mean flow velocity parametric study.

Operational conditions			
	Mean flow velocity	Tube inner diameter	Mass flow rate
	U_{ave} [mm/s]	d_i [mm]	\dot{m} [kg/h]
Simulation 1	0.64	30	3.6
Simulation 2	1.28	30	7.2
Simulation 3	1.93	30	10.8
Simulation 4	2.57	30	14.4
Simulation 5	3.21	30	18.0
Simulation 6	3.85	30	21.6
Simulation 7	5.13	30	28.8
Simulation 8	6.10	30	34.2
Simulation 9	8.50	30	47.7
Simulation 10	11.50	30	64.5

Similarly to the previous subsection, the converged results for the fraction of non-reflected microwave power, $1 - |S_{11}|^2$, microwave efficiency, η_{MW} , thermal efficiency, η_T , outlet fraction of melted material, θ , and global efficiency, η_G , for each performed simulation are presented in Figure 4.27 and will be discussed in detail.

Regarding the $1 - |S_{11}|^2$ and η_{MW} curves, it can be observed that both show the same behavior, being the later shifted down from the other due to the presence of the microwave leakage. The almost perfect vertical shift between the curves indicate that the ratio between the microwave leakage and the power input is kept practically constant, around 10%, for the studied diameter. The trend observed show that the microwave efficiency decreases continuously as the mean flow velocity increases. To justify this trend, it is useful to recall that the diameter used in this parametric study belong to the second class described in the previous subsection, meaning that the radiation absorption occurs in a thin outer layer facing the incoming waves. This thin absorption layer is not axisymmetric relatively to the tube's central axis due to the cut-off frequency effect that takes place for large diameters.

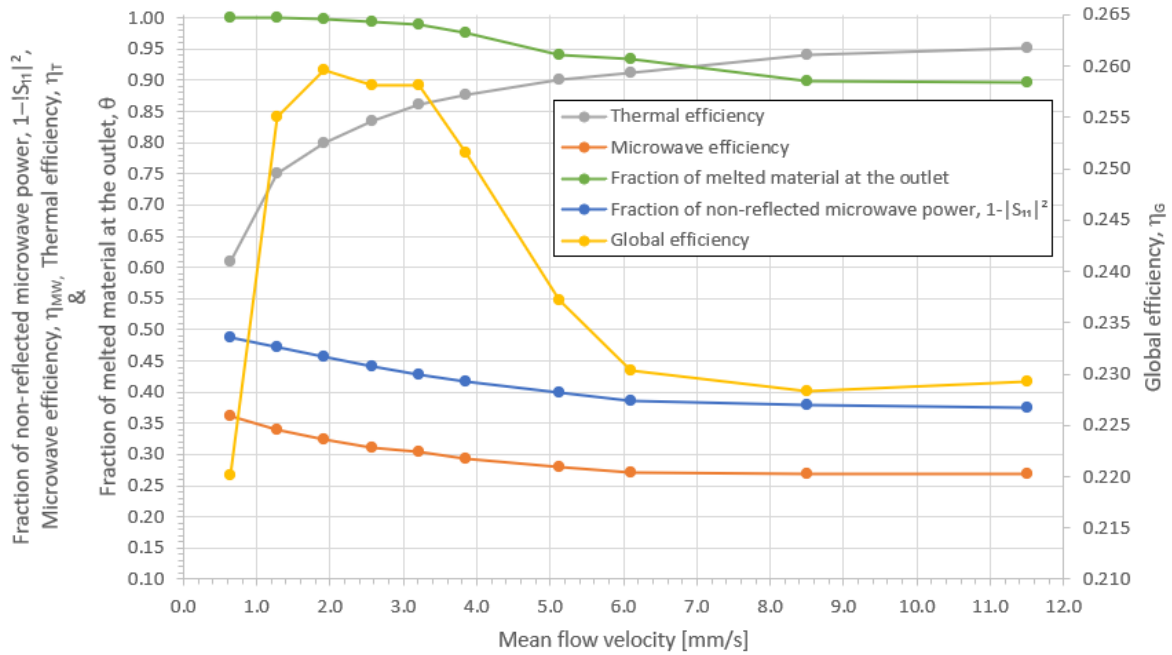


Figure 4.27: Fraction of non-reflected microwave power, $1 - |S_{11}|^2$, microwave efficiency, η_{MW} , thermal efficiency, η_T , outlet fraction of melted material, θ , and global efficiency, η_G , versus mean flow velocity, U_{ave} , for a tube inner diameter of $d_i = 30$ mm.

As the mean flow velocity increases, so does the mass flow rate of glass through the tube. Consequently, the power input delivered by the *MATLAB* controller rises with the increase of the mean flow velocity. Despite the increasing mass flow rate, the volume that effectively absorbs the radiation is decreasing in a feedback regime as the mean flow velocity rises. This happens because since the cut-off frequency effect does not allow the absorption layer to extend around the tube, this absorption region generates more heat due to the higher power input. Consequently, the temperatures in the absorption layer increase as illustrated in Figure 4.28. With the temperature rise, the penetration depth decreases as showed in Figure 4.29, and the absorption layer gets thinner contributing to an even faster tempera-

ture rise in the hot zone. The penetration depth decrease is then the cause of the continuous drop of the microwave efficiency due to a lower temperature uniformity as the mean flow velocity increases.

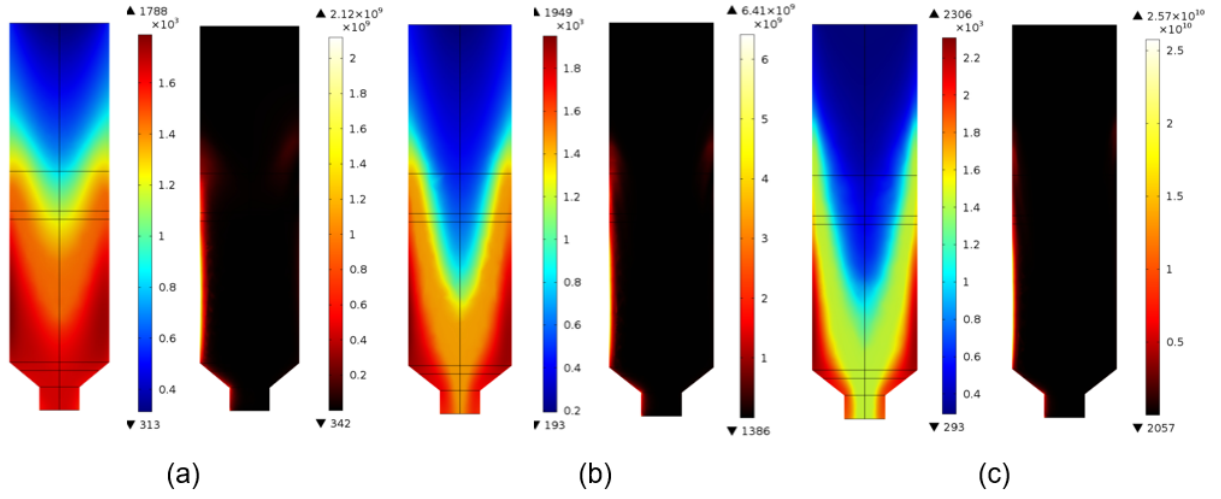


Figure 4.28: Thermal field [K] and heat source distribution [W/m^3] in the glass domain for (a) $U_{ave} = 0.64 \text{ mm/s}$, (b) $U_{ave} = 1.93 \text{ mm/s}$ and (c) $U_{ave} = 6.10 \text{ mm/s}$, for a tube inner diameter of $d_i = 30 \text{ mm}$.

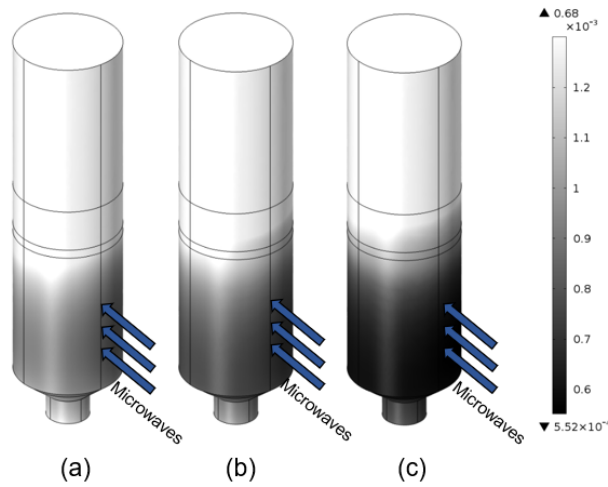


Figure 4.29: Penetration depth values for (a) $U_{ave} = 0.64 \text{ mm/s}$, (b) $U_{ave} = 1.93 \text{ mm/s}$ and (c) $U_{ave} = 6.10 \text{ mm/s}$, for a tube inner diameter of $d_i = 30 \text{ mm}$.

On the other hand, the thermal efficiency curve presents a continuous rise as the mean flow velocity increases as shown in Figure 4.27. This behavior can be justified similarly as in the last subsection. Although there is an increase in the thermal losses, the ratio between these losses and the power absorbed drops as the mean flow velocity increases.

With respect to the outlet fraction of melted material, θ , Figure 4.27 shows that for mean flow velocities above $U_{ave} = 1.93 \text{ mm/s}$, the exiting glass is no longer fully processed. For large velocities, the heat diffusion mechanisms are not able to transfer the heat absorbed in the outer layer to the central region of the material and, consequently, the temperatures do not exceed the melting point and solid

glass starts to flow out of the tube. It is important to notice that this decrease in the value of θ is empowered by the large diameter used in the study.

The global efficiency curve, obtained from the product of the other three, exhibits an initial rise due to the sharp increase in the thermal efficiency. After that initial increasing tendency, a critical mean flow velocity of $U_{ave} = 1.93 \text{ mm/s}$ maximizes the global efficiency. Then the η_G curve starts to drop mainly due to the decrease in the value of θ , since the increase in the thermal efficiency compensates the decrease in the microwave one, as they have a similar derivative value. It is important to notice that the global efficiency varies only 4%, between its minimum and maximum values, for the mean flow velocities studied, indicating that the velocity has less influence in the glass melting process than the tube inner diameter, studied previously.

As in the previous subsection, a comparison between the global efficiency obtained with and without rotation is presented in Figure 4.30. Observing both curves, it is evident that rotation plays a very important role in the glass melting process when higher mass flow rates are desired, especially when large diameters are used. The very low values obtained in the simulations without rotation and the sharp drop in the curve is clearly due to the steep decrease in the value of θ . As showed in Section 4.3 and explained in the previous subsection, rotation improves the uniformization of the thermal field and favors the heat diffusion from the outer absorption layer to the central region of the glass, keeping the outlet fraction of melted material as high as possible. Without rotation, not only the global efficiency for a defined mean flow velocity is lower, but also the mass flow rates allowed in the process are very limited.

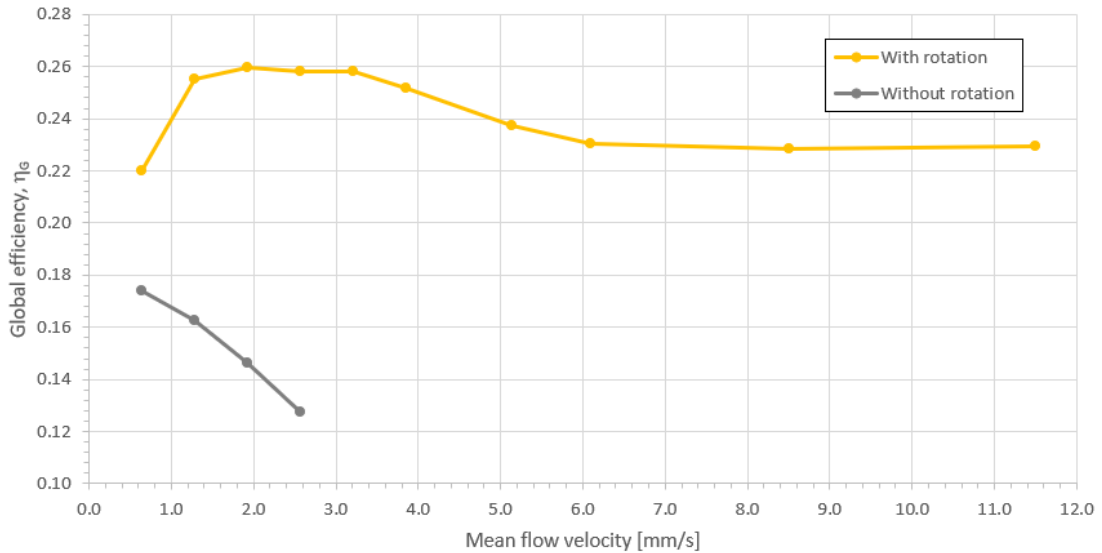


Figure 4.30: Global efficiency, η_G , versus mean flow velocity, U_{ave} , for a tube inner diameter of $d_i = 30 \text{ mm}$, for the cases with and without tube rotation.

With this parametric study, it can be concluded that for large diameters, the microwave efficiency decreases continuously with the rise of the mean flow velocity. On the other hand, the thermal efficiency shows the opposite trend. The outlet fraction of melted material, θ , is greatly influenced by the flow velocity. For this value to be kept as high as possible the tube rotation is crucial. Therefore, the

global efficiency of the glass melting process exhibits a maximum value for a critical mean flow velocity. Below and above this critical velocity, lower thermal efficiencies and reductions in the value of θ affect, respectively, the global performance of the process.

4.6.3 Combined parametric study

In the previous subsections, two parametric studies were performed in order to analyze the influence of the tube inner diameter and mean flow velocity on the efficiency of the glass melting process. In the first one, the diameter was varied with a fixed mean flow velocity and, in the second one, the velocity was changed while keeping a fixed diameter.

In this subsection a combined parametric study is presented as complement to the previous ones. Since such combined parametric study for the continuous flow microwave glass melting process was not found in the literature by the time this Thesis was written, the main objective of this study is to give insight on how the process responds for different values of the examined parameters and thus to give some support in the design stage of a microwave continuous system, and also to find the operational conditions that maximize the global efficiency of this process within the given study domain.

It is important to refer that it is not the purpose of this study to develop, or use, an optimization algorithm, since the computational effort required to run a single simulation is too high and also because the main purpose of the study is to obtain the global efficiency surface and not only its maximum value. For that reason, to find the best operational conditions, several simulations were done with different values of d_i and U_{ave} . The study domain is illustrated in Figure 4.31, which shows that the analyzed tube inner diameters and mean flow velocities were changed in the intervals $12.5 \text{ mm} \leq d_i \leq 30 \text{ mm}$ and $0.64 \text{ mm/s} \leq U_{ave} \leq 11.50 \text{ mm/s}$, respectively.

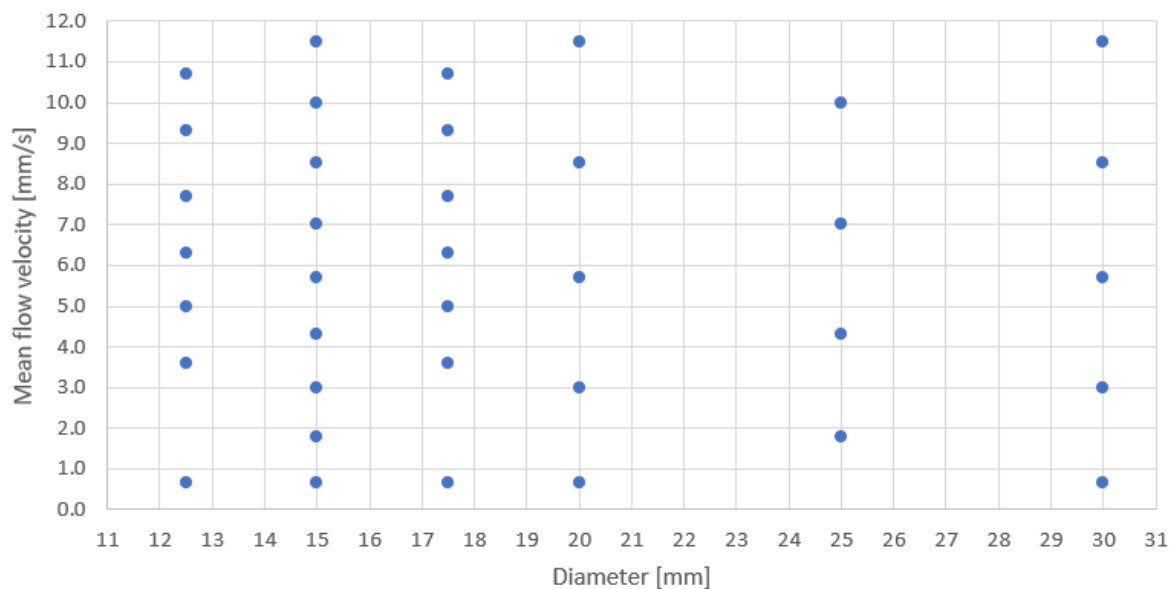


Figure 4.31: Domain for the combined parametric study. Each point represents a performed simulation.

For each simulation, the converged values for the microwave efficiency, η_{MW} , thermal efficiency, η_T , outlet fraction of melted material, θ , and global efficiency, η_G , were stored and plotted against both d_i and U_{ave} creating three-dimensional surfaces. These surfaces are presented in Figure 4.32 in a top view for better visualization. The global efficiency surface provides the information about the combination between d_i and U_{ave} that should be used to minimize the energy consumption in the glass melting process. However, since the global efficiency is obtained from the product between the values of η_{MW} , η_T and θ , to understand its behavior, it is indispensable to firstly examine the trends of the other three quantities. In the first place, a detailed description of the microwave efficiency surface will be given, followed by a briefer description of the η_T and θ ones. This analysis will, obviously, be supported by the conclusions obtained in the previous subsections.

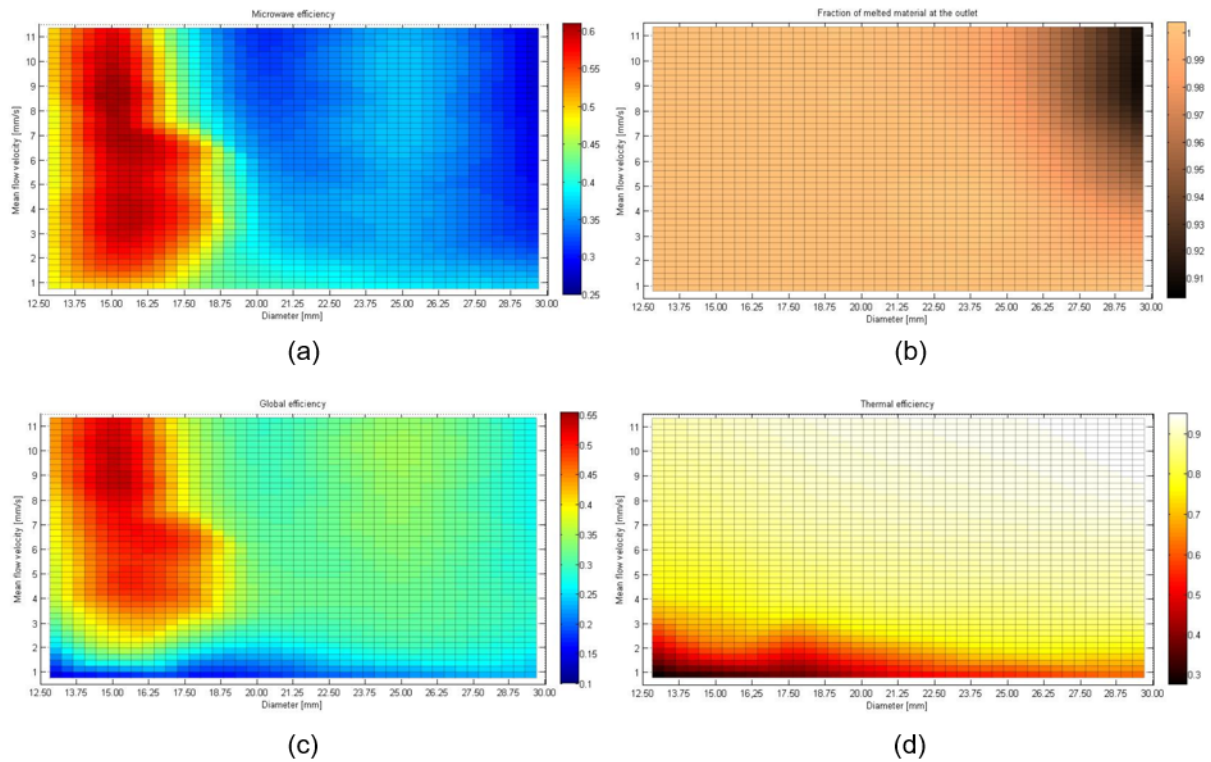


Figure 4.32: Combined influence of the tube inner diameter, d_i [mm], and mean flow velocity, U_{ave} [mm/s], on the (a) microwave efficiency, η_{MW} , (b) outlet fraction of melted material, θ , (c) global efficiency, η_G , and (d) thermal efficiency, η_T .

By observing Figure 4.32a, which represents the microwave efficiency dependence on both d_i and U_{ave} , it can be confirmed the existence of two classes of diameters as already referred in Subsection 4.6.1. For the second-class diameters, $d_i \geq 20$ mm, there is a clear tendency for the microwave efficiency to continuously decrease as the mean flow velocity increases. As explained before in Subsection 4.6.2, this happens due to the strong influence of the cut-off frequency effect and to the low penetration depths observed in the glass material, caused by the very high values of its dielectric properties.

For smaller diameters, belonging to the first class where $12.5 \text{ mm} < d_i < 20$ mm, the microwave efficiency firstly increases with the mean flow velocity and at a certain critical point reaches a maximum value. Then, for velocities higher than the critical one, the microwave efficiency starts to drop. For the

studied mean flow velocity interval, at $d_i = 12.5$ mm the microwave efficiency tends to increase without showing a critical value for the analyzed velocities. For these diameters, at low mean flow velocities, diffusion attenuates the radial temperature gradients and the thermal field varies practically only in the direction of the flow and the hot spot appears centered between the cavity top and bottom surfaces. The maximum temperatures are very high, and the penetration depth is low. When the mean flow velocity is increased, radial temperature gradients appear and the maximum temperatures decrease contributing to an increase in the penetration depth – as depicted in Figures 4.33a and 4.33b – and thus to a rising of the microwave efficiency. Until the critical velocity is reached, the microwave efficiency continues to increase due to the rise of the area of the outer surface of the absorbing layer as illustrated in Figures 4.33b and 4.33c. After the critical mean flow velocity, the microwave efficiency starts to drop because the area of the outer surface of the absorbing layer stays practically constant and penetration depth continues to decrease as a consequence of the temperature rise, similarly to what happens for the large diameters, as shown in Figures 4.33c and 4.33d.

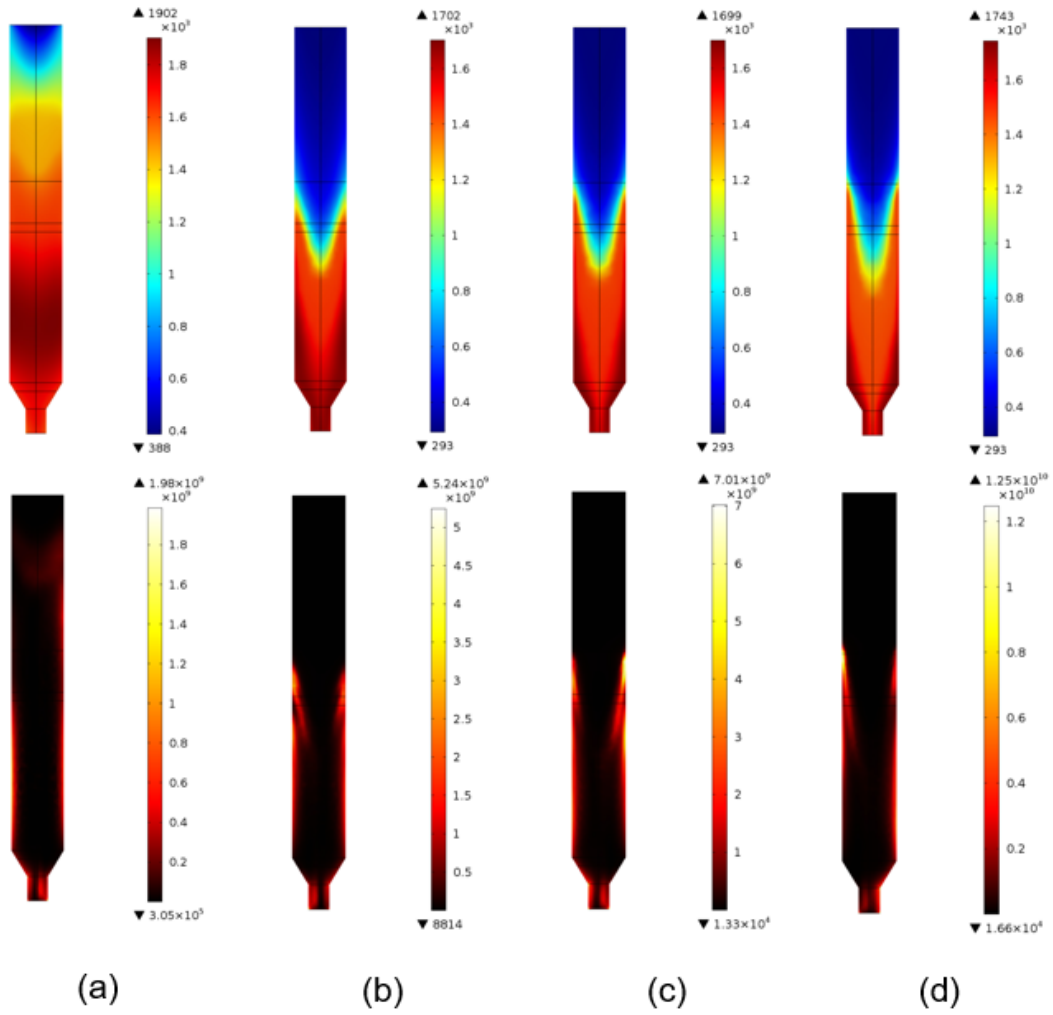


Figure 4.33: Thermal field [K] and heat source distribution [W/m³] in the glass domain for (a) $U_{ave} = 0.64$ mm/s, (b) $U_{ave} = 4.30$ mm/s, (c) $U_{ave} = 8.50$ mm/s, which is the critical mean flow velocity and (d) $U_{ave} = 11.50$ mm/s, for a tube inner diameter of $d_i = 15$ mm.

The evolution of this surface also shows that the microwave efficiency tends to continuously increase as the tube inner diameter decreases for all mean flow velocities studied as explained in detail in Subsection 4.6.1. It is, however, important to recall that this tendency is strongly related to the lower penetration depths of the glass at high temperatures.

It is also important to refer that these results are in accordance with the work of Yousefi *et al.* [28] which presents a similar parametric study for the microwave heating process of flowing water already discussed in Subsection 1.3.3 and illustrated in Figure 1.1.

Figure 4.32b, shows that for almost all simulations the glass leaves the tube totally processed. It is only for large diameters and with high mean flow velocities that the value of θ starts to drop and affects the global efficiency. Observing Figure 4.32d, it can be stated that the thermal efficiency continuously grows with the increase of both d_i and U_{ave} as it was explained in the previous subsections.

After analyzing the microwave and thermal efficiencies surfaces as well as the variation of the outlet fraction of melted material in the defined study domain, Figure 4.32c, describing the global efficiency, can be commented. It can be observed that, for all studied diameters, the global efficiency rises with the increase of the mean flow velocity until a critical value is reached, where a maximum efficiency is achieved. In a general way, this critical velocity increases as the diameter decreases. After the critical velocity, the global efficiency tends to drop and then stabilize. This behavior is due to the influence of the thermal efficiency on the microwave process. For low velocities, the global efficiency curve shows low values due to the very low thermal efficiencies.

Since for high mean flow velocities, the thermal efficiency tends to stabilize for values close to unity, its influence on the global efficiency vanishes. On the other hand, the curve of θ only affects the global efficiency for diameters close to $d_i = 30$ mm at very high velocities. For that reason, and since the highest values of the microwave efficiency are in the region where the thermal efficiency has little influence and the value of θ has no influence at all, the parameters that maximize the global efficiency are $d_i = 15$ mm and $U_{ave} = 8.50$ mm/s, corresponding to a mass flow rate of $\dot{m} = 11.92$ kg/h. The converged results for these operational conditions are summarized in Table 4.12.

Table 4.12: Steady-state results for the glass melting process with $d_i = 15$ mm and $\dot{m} = 11.92$ kg/h.

Variable	Value
Power input, P_{in} [W]	11952
Power absorbed, P_{abs} [W]	7331
Sensible heat at outlet (theoretical, SH_{needed} / obtained, SH) [W]	5140/5129
Latent heat at outlet (theoretical, LH_{needed} / obtained, LH) [W]	1285/1286
Thermal losses, P_{Loss} [W]	916
Microwave efficiency, η_{MW} [%]	61
Thermal efficiency, η_T [%]	88
Global efficiency, η_G [%]	54
Specific energy consumption, SEC [kJ/kg]	3605

Observing the SEC value obtained and comparing it to the reference value for the conventional process, $SEC_{conv} = 7800 \text{ kJ/kg}$ given in [1], it can be concluded that energy savings of almost 54% can be achieved using the microwave melting process.

Similarly to what has been done at the end of Section 4.4, the energy balance of the microwave cavity for these operational conditions is presented in Figure 4.34. It can be observed that the microwave power reflected represents 24% of the microwave power input, while 15% is escaping as microwave leakage. For these operational conditions 61% of the microwave power input is being absorbed by the glass and tube, which represents a microwave efficiency of $\eta_{MW} = 61\%$. Of the power that is effectively absorbed by both glass and tube, 70% is being used to heat the glass from 293 K to 1600 K, 18% is being used in the glass phase change and only 12% is being lost as convection and radiation through the microwave cavity exterior walls. Since only the sensible and latent heat are useful power in the process, the thermal efficiency is, for this case, $\eta_T = 88\%$ and a global efficiency of $\eta_G = 54\%$ was achieved.

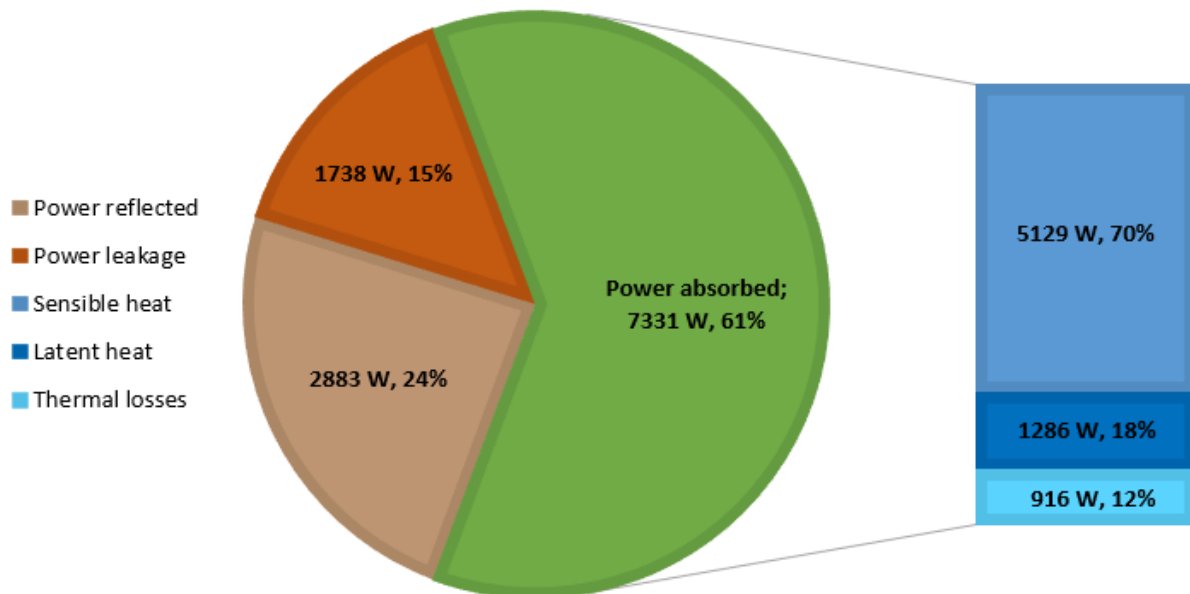


Figure 4.34: Complete energy balance of the microwave cavity for the case with $d_i = 15 \text{ mm}$ and $\dot{m} = 11.92 \text{ kg/h}$

Chapter 5

Conclusions

A continuous flow microwave heating unit with the purpose of melting glass was developed and modelled in this Thesis. The commercial software *COMSOL Multiphysics* was used to numerically simulate the glass melting process by coupling the electromagnetic and thermal physics. Three-dimensional transient simulations were run in order to achieve steady-state results with the desired outlet conditions and with the lowest possible power input. To reach this objective, the transient simulations were controlled by a developed *MATLAB* algorithm coupled to the *COMSOL* interface. This algorithm allowed to control the cavity geometry with a moving plunger, enabling the optimization of the process efficiency, and to control the power input delivered by considering the thermal losses, the microwave efficiency variations, as well as the power required to heat and melt the flowing material.

Several studies in this Thesis were carried out in order to analyze the performance of the developed *MATLAB* algorithm and the influence of several operation parameters in the microwave glass melting process. The thermal history for given operational conditions was studied in detail showing that the *MATLAB* code was able to control the simulation until a steady-state solution was achieved. The results showed that the outlet conditions defined by the user were achieved and temperature-related problems, such as the *thermal runaway* phenomenon, were not observed.

It was verified that by imposing rotation on the applicator tube it allowed to have more uniform temperature fields and thus lower maximum temperatures in the glass and in the tube. This represents an advantage not only for the tube's working conditions but also for the process itself since a rise in the microwave efficiency was observed as the rotation was increased. It was also concluded that above some critical rotation value, the increase in the microwave efficiency was no longer significant.

The influence of the plunger position adjustments, required to keep the microwave efficiency as high as possible, was also analyzed and it was observed that it is always better to adjust the plunger position than to keep it fixed. However, better results were verified for smaller diameters due to the lower impact of the cut-off frequency effect.

Microwave leakage was considered in the simulations done in this Thesis. However, to quantify its influence in the process, a simulation without leakage was carried out and compared. It was concluded that microwave leakage has a considerable impact on the glass melting process and should be avoided or limited as much as possible.

The influence of the applicator tube inner diameter and mean flow velocity on the global efficiency of the glass melting process was analyzed through a parametric study. The results showed that, for the defined study domain, operational conditions that maximize the global efficiency of the process can be found and that their values are strongly related to the penetration depth of the processed material which depends on its dielectric properties. For these conditions it was observed that using microwave energy as the heating source for melting glass allowed for energy savings of almost 54% relatively to the conventional process.

5.1 Achievements

The numerical study presented in this Thesis has confirmed that the commercial software *COM-SOL Multiphysics* represents a very useful tool to the design of microwave heating systems. The developed *MATLAB* algorithm used to control the numerical simulations has proven to be extremely effective since the converged solutions obtained presented the highest possible global efficiency with minimum power input, corresponding to the outlet conditions required *a priori* by the user, namely a defined averaged material outlet temperature and a totally processed material leaving the applicator tube. The controller has also proven to be capable of achieving automatically steady-state solutions without any temperature-related problems and without any intervention by the user. It was also shown that this controller can be applied in a physical apparatus since all its input variables can be measured by devices found in the market.

The performed detailed parametric study represents a true innovation on the microwave glass melting process research since nothing similar was found in the literature by the time this Thesis was written and constitutes a precious help in the design of microwave continuous systems and in the choice of the best combination of operational conditions in such systems.

5.2 Future Work

In order to improve the numerical model to better simulate the real microwave glass melting process, some efforts should be done to better model the flow of the material being processed. Some distinction should be made between the solid particle phase and the molten phase flows.

To improve the global efficiency of the process, microwave transparent materials with lower thermal conductivity should be found and tested to be assigned to the applicator tube. This would decrease even more the thermal losses of the system. The microwave continuous flow glass melting process should be studied using multi-mode cavities to limit the influence of the cut-off frequency effect that was observed in this work. For those cavities, some systems capable of controlling the electromagnetic field resonance should also be studied and developed, like the 3 stub-tuner, since it is a more popular impedance matching mechanism used in microwave systems, although way more difficult to model in numerical simulations [61-63].

Bibliography

- [1] A. Schmitz, J. Kamiński, B.M. Scalet and A. Soria. Energy consumption and CO₂ emissions of the European glass industry. *Energy Policy*, 39:142-155, 2011.
- [2] R. Beerkens. Analysis of elementary process steps in industrial glass melting tanks – Some ideas on innovations in industrial glass melting. *Ceramics Silikaty*, 52(4):206-217, 2008.
- [3] Y. Yao, T. Watanabe, T. Yano, T. Iseda, O. Sakamoto, M. Iwamoto and S. Inoue. An innovative Energy-saving in-flight melting Technology and its application to glass production. *Science and Technology of Advanced Materials*, 9(2):025013, 2008.
- [4] D. Agrawal. Microwave sintering of ceramics, composites and metallic materials, and melting of glasses. *Transactions of the Indian Ceramic Society*. 65(3):129-144, 2006.
- [5] A.K. Mandal, S. Sen, S. Mandal, C. Guha and R. Sen. Energy efficient melting of glass for nuclear waste immobilization using microwave radiation. *International Journal of Green Energy*, 12:1280-1287, 2015.
- [6] Y. Alpert and E. Jerby. Coupled thermal-electromagnetic model for microwave heating of temperature-dependent dielectric media. *IEEE Transactions on Plasma Science*, 27(2):555-562, 1999.
- [7] A.C. Metaxas and R.J. Meredith. *Industrial microwave heating*. Peregrinus, 1983.
- [8] Y.V. Bykov, K.I. Rybakov and V.E. Semenov. High-temperature microwave processing of materials. *Journal of Physics D: Applied Physics*, 34: R55-R75, 2001.
- [9] P.K. Loharkar, A. Ingle and S. Jhavar. Parametric review of microwave-based materials processing and its applications. *Journal of Materials Research and Technology*, 8(3):3306-3326, 2019.
- [10] A.K. Mandal and R. Sen. An overview on microwave processing of material: A special emphasis on glass melting. *Materials and Manufacturing processes*, 32:1-20, 2016.
- [11] D. Nowak. The impact of microwave penetration depth on the process of heating the moulding sand with sodium silicate. *Archives of Foundry Engineering*, 17(4):115-118, 2017.
- [12] C. Dorn, R. Behrend, D. Giannopoulos, L. Napolano, B. García Baños, V. James, V. Uhlig, J. M. Catalá, M. Founti and D. Trimis. KPI and LCA evaluation of integrated microwave technology for high temperature processes. *Procedia CIRP*, 29:492-497, 2015.
- [13] C.A. Vriezinga, S. Sánchez-Pedreño and J. Grasman. Thermal runaway in microwave heating: a mathematical analysis. *Applied Mathematical Modelling*, 26:1029-1038, 2002.
- [14] X. Wu, J.R. Thomas, Jr. and W.A. Davis. Control of thermal runaway in microwave resonant cavities. *Journal of Applied Physics*, 92(6):3374-3380, 2002.

- [15] T. Santos, M.A. Valente, J. Monteiro, J. Sousa and L.C. Costa. Electromagnetic and thermal history during microwave heating. *Applied Thermal Engineering*, 31:3255-3261, 2011.
- [16] D. Salvi, D. Boldor, G.M. Aita and C.M. Sabliov. COMSOL Multiphysics model for continuous flow microwave heating of liquids. *Journal of Food Engineering*, 104:422-429, 2011.
- [17] S. Tuta and T.K. Palazoğlu. Finite element modeling of continuous-flow microwave heating of fluid foods and experimental validation. *Journal of Food Engineering*, 192:79-92, 2017.
- [18] Y. Wu, T. Hong, Z. Tang and C. Zhang. Dynamic model for a uniform microwave-assisted continuous flow process of ethyl acetate production. *Entropy*, 20(4):241-254, 2018.
- [19] R.M.C. Mimoso, D.M.S. Albuquerque, J.M.C. Pereira and J.C.F. Pereira. Simulation and control of continuous glass melting by microwave heating in a single-mode cavity with energy efficiency optimization. *International Journal of Thermal Sciences*, 111:175-187, 2017.
- [20] R.H. Vaz, J.M.C. Pereira, A.R. Ervilha and J.C.F. Pereira. Simulation and uncertainty quantification in high temperature microwave heating. *Applied Thermal Engineering*, 70:1025-1039, 2014.
- [21] J.P.M. Mendes. *Simulation of cement clinker process by of microwave heating*. Master thesis, Instituto Superior Técnico, Universidade de Lisboa, 2017.
- [22] L. Acevedo, S. Usón and J. Uche. Numerical study of cullet glass subjected to microwave heating and SiC susceptor effects. Part 1: Combined electric and thermal model. *Energy Conversion and Management*, 97:439-457, 2015.
- [23] J. Clemens and C. Saltiel. Numerical modeling of materials processing in microwave furnaces. *International Journal of Heat and Mass Transfer*, 39(8):1665-1675, 1996.
- [24] W. Cha-um, P. Rattanadecho and W. Pakdee. Experimental and numerical analysis of microwave heating of water and oil using a rectangular wave guide: Influence of sample sizes, positions, and microwave power. *Food and Bioprocess Technology*, 4:544-558, 2011.
- [25] X. Gao, X. Liu, P. Yan, X. Li and H. Li. Numerical analysis and optimization of the microwave inductive heating performance of water film. *International Journal of Heat and Mass Transfer*, 139:17-30, 2019.
- [26] R. Morschhäuser, M. Krull, C. Kayser, C. Boberski, R. Bierbaum, P.A. Püschner, T.N. Glasnov and C.O. Kappe. Microwave-assisted continuous flow synthesis on industrial scale. *Green Processing and Synthesis*, 1:281-290, 2012.
- [27] J. Zhu, A.V. Kuznetsov and K.P. Sandeep. Mathematical modeling of continuous flow microwave heating of liquids (effects of dielectric properties and design parameters). *International Journal of Thermal Sciences*, 46:328-341, 2007.
- [28] T. Yousefi, S.A. Mousavi, M.Z. Saghir and B. Farahbakhsh. An investigation on the microwave heating of flowing water: a numerical study. *International Journal of Thermal Sciences*, 71:118-127, 2013.
- [29] N.G. Patil, E.V. Rebrov, K. Eränen, F. Benaskar, J. Meuldijk, J.-P. Mikkola, V. Hessel, L.A. Hulshof, D.Y. Murzin and J.C. Schouten. Effect of the load size on the efficiency of microwave heating under stop flow and continuous flow conditions. *Journal of Microwave Power and Electromagnetic Energy*, 46(2):83-92, 2012.

- [30] S. Ramo, J.R. Whinnery and T. Van Duzer. *Fields and Waves in Communication Electronics*. Wiley, 1994.
- [31] V. Brederode. *Aerodinâmica incompressível: Fundamentos*. IST Press, 2014.
- [32] D.J. Griffiths and R. College. *Introduction to electrodynamics*. Prentice Hall, 1999.
- [33] H. Eskelinen and P. Eskelinen. *Microwave component mechanics*. Artech House, 2003.
- [34] R. Berger, T. Rogge, E. Jansen and R. Rolfes. Probabilistic vibration and lifetime analysis of regenerated turbomachinery blades. *Advances in Aircraft and Spacecraft Science*, 3(4):503-521, 2016.
- [35] J. Bartl and M. Baranek. Emissivity of aluminum and its importance for radiometric measurement. *Measurement Science Review*, 4(3):31-36, 2004.
- [36] R. Behrend, C. Dorn, V. Uhlig and H. Krause. Investigations on container materials in high temperature microwave applications. *Energy Procedia*, 120:417-423, 2017.
- [37] A. Simpson and A.D. Stuckes. The thermal conductivity of 'isotropic' and hot-pressed boron nitride. *Journal of Physics D: Applied Physics*, 9(4):621-630, 1976.
- [38] V.L. Solozhenko. Thermodynamics of dense boron nitride modifications and new phase P,T diagram for BN. *Thermochimica Acta*, 218:221-227, 1993.
- [39] K. Sridharan, T. Allen, M. Anderson, G. Cao and G. Kulcinski. *Emissivity of candidate materials for VHTR applications: Role of oxidation and surface modification treatments*. Project report, University of Wisconsin, 2011.
- [40] F. Modarresifar, P.A. Bingham and G.A. Jubb. Thermal conductivity of refractory glass fibers. *Journal of Thermal Analysis and Calorimetry*, 125(1):35-44, 2016.
- [41] M. Rossi and V.M. Rocco. External walls design: The role of periodic thermal transmittance and internal areal heat capacity. *Energy and Buildings*, 68:732-740, 2014.
- [42] P. Principi and R. Fioretti. Thermal analysis of the application of pcm and low emissivity coating in hollow bricks. *Energy and buildings*, 51:131-142, 2012.
- [43] http://microwavepropertiesnorth.ca/glasses_insulation_materials/ consulted on November 30th, 2019.
- [44] S.C. Carniglia and G.L. Barna. *Handbook of industrial refractories technology. Principles, types, properties and applications*. Noyes Publications, 1992.
- [45] E. Tatli, J.P. Mazzocchi and P. Ferroni. CFD modeling of sodium-oxide deposition in sodium-cooled fast reactor compact heat exchangers. In *16th International Topical Meeting on Nuclear Reactor Thermalhydraulics Conference*, 2015.
- [46] P. Auerkari. Mechanical and physical properties of engineering alumina ceramics. *VTT Tiedotteita*, 1792, 26, 1996.
- [47] D.W. Green and R.H. Perry. *Perry's Chemical engineers' handbook*. McGraw-Hill, 8th edition, 2008.
- [48] T.L. Bergman, A.S. Lavine, F.P. Incropera and D.P. Dewitt. *Fundamentals of heat and mass transfer*. John Wiley & Sons, 7th edition, 2011.
- [49] N.P. Bansal and R.H. Doremus. *Handbook of glass properties*. Academic Press, 1986.

- [50] F. Albouchi, M. Fetoui, F. Rigollet, M. Sassi and S.B. Nasrallah. Optimal design and measurement of the effective thermal conductivity of a powder using a crenel heating excitation. *International Journal of Thermal Sciences*, 44:1090-1097, 2005.
- [51] L. Pilon, G. Zhao and R. Viskanta. Three-dimensional flow and thermal structures in glass melting furnaces. Part 1. Effects of the heat flux distribution. *Glass Science and Technology*, 75(2):55-68, 2006.
- [52] M.M. Hossain, Y. Yao, T. Watanabe, F. Funabiki and T. Yano. In-flight thermal treatment of soda-lime-silica glass powders for glass production by argon-oxygen induction thermal plasmas. *Chemical Engineering Journal*, 150:561-568, 2009.
- [53] A. Napolitano and E.G. Hawkins. Viscosity of a standard soda-lime-silica glass. *Journal of Research of the National Bureau of Standards – A. Physics and Chemistry*, 68A(5):439-448, 1964.
- [54] G.D. Raithby and K.G.T. Hollands. Natural convection. In W.M. Rohsenow, J.P. Hartnett and Y.I. Cho (Eds). *Handbook of heat transfer*. McGraw Hill, 3rd edition, 1998.
- [55] W.L. Oberkampf and T.G. Trucano. Verification and validation in computational fluid dynamics. *Progress in Aerospace Sciences*, 38:209-272, 2002.
- [56] W.L. Oberkampf and C.J. Roy. *Verification and validation in scientific computing*. Cambridge University Press, 2010.
- [57] L. Eça and M. Hoekstra. A procedure for the estimation of the numerical uncertainty of CFD calculations based on grid refinement studies. *Journal of Computational Physics*, 262:104-130, 2014.
- [58] P.J. Roache. Perspective: A method for uniform reporting of grid refinement studies. *Journal of Fluids Engineering*, 116:405-413, 1994.
- [59] G. Kosec and M. Depolli. Superlinear speedup in OpenMP parallelization of local PDE solver. In *2012 Proceedings of the 35th International Convention MIPRO*, 389-395, 2012.
- [60] V. P. Astakhov. *Drills: Science and technology of advanced operations*. CRC Press, 2014.
- [61] A. Ahmed and E. Siores. Microwave joining of 48% alumina–32% zirconia–20% silica ceramics. *Journal of Materials Processing Technology*, 118:88-95, 2001.
- [62] A. A. Chtcherbakov and R. L. Swart. Automatic microwave tuner for plasma deposition applications using a gradient search method. *Journal of Microwave Power and Electromagnetic Energy*, 32(1):28-33, 1997.
- [63] S. H. Lee, W. Choi, S. H. Park and S. Jun. Design and fabrication of a dual cylindrical microwave and ohmic combination heater for processing of particulate foods. *Journal of Biosystems Engineering*, 40(3):250-260, 2015.